DAMPING OF AXIAL INSTABILITIES BY SOLID PROPELLANT ROCKET EXHAUST NOZZLES

A THESIS

Presented to

The Faculty of the Division of Graduate

Studies and Research

by

Bangalore Ananthamurthy Janardan

In Partial Fulfillment

of the Requirements for the Degree

Doctor of Philosophy

in the School of Aerospace Engineering

Georgia Institute of Technology

August, 1973

DAMPING OF AXIAL INSTABILITIES BY SOLID PROPELLANT

ROCKET EXHAUST NOZZLES

Approved:

Ben T. Zinn, Chairman

Warren C. Strahle

William A. Bell

Date approved by Chairman: 7/6/73

ACKNOWLEDGMENTS

I hereby express my sincere appreciation to Dr. Ben T. Zinn for his suggestion of the dissertation topic, for his sustained guidance and encouragement during this investigation and for his painstaking scrutiny of the manuscript. I also thank Drs. Warren C. Strahle and William A. Bell for their careful examination of the manuscript and for their constructive comments.

The expert assistance of Mr. Brady R. Daniel while conducting the experiments was invaluable and I earnestly thank him for his generous help and cooperation. Also I am much obliged to Dr. William A. Bell who contributed significantly to this study since it was he who, under the direction of Dr. Zinn, first applied the modified technique used in this investigation to nozzle admittance measurements. The assistance given by Mr. Allan J. Smith, Jr. in computational work and by Mr. M. K. Singhal in fitting empirical relations to experimental data is gratefully appreciated.

The financial assistance provided by a research assistantship in the Aerospace School of the Georgia Institute of Technology is acknowledged.

TABLE OF CONTENTS

Table of Contents (Continued)

LIST OF TABLES

LIST OF ILLUSTRATIONS

List of Illustrations (Continued)

List of Illustrations (Continued)

List of Illustrations (Continued)

GLOSSARY OF SYMBOLS

A	amplitude of pressure oscillation, psfa (RMS); also used as admittance ratio, defined by Equation (2-26)
$\hat{A}$	constant
c	velocity of sound, ft/sec
$d = L_c - z$	axial distance measured from nozzle entrance, ft
E	measure of experimental error in pressure amplitude, defined by Equation (2-15)
f	frequency, Hertz
F	measure of experimental error in pressure phase, defined by Equation (2-17)
J	ratio of nozzle throat area to chamber cross-sectional area
L	length, ft
M	mean flow Mach number
p	pressure, psfa (RMS)
P	pressure amplitude, psfa (RMS)
q	secondary-to-primary flow rate ratio
r	radius, ft
Re	real part of a complex quantity
S	normalized frequency, defined by Equation (4-1); also used as cross-sectional area, ft^2
T	period of oscillation, sec
u	axial velocity, ft/sec
V	volume, ft^3
$\hat{V}$	quantity defined by Equation (2-21)
y	nondimensional admittance, defined by Equation (2-8)
Y	admittance, defined by Equation (2-1), ft^3/lb_f-sec

$Y_g = \frac{g}{\bar{\rho}\bar{c}}$	characteristic admittance of the gas in the chamber, ft^3/lb_f-sec
z	axial length measured from injector end
α	nozzle admittance parameter, defined by Equation (2-6)
α_N	nozzle decay coefficient, defined by Equation (2-19), sec^{-1}
β	nozzle admittance parameter, defined by Equation (2-7)
γ	specific heat ratio
Γ	real part of nondimensional admittance y_N
δ	pressure phase, defined by Equation (2-14), radians
η	imaginary part of nondimensional admittance y_N
θ	phase change between incident and reflected pressure waves, radians
λ	wavelength, ft
Λ	nondimensional decay coefficient
ρ	density of gas in the chamber, lb_m/ft^3
σ	scale factor, defined by Equation (2-34)
ω	angular frequency, radians/sec

SUBSCRIPTS

A	denotes conditions in actual engine
c	denotes a chamber property
E	denotes an experimental quantity
f	denotes a quantity pertaining to a "family" of nozzles
i	summation index
N	quantity related to nozzle behavior
ref	denotes a reference quantity
t	denotes a theoretical quantity
1	perturbed quantity

SUPERSCRIPTS

$(\bar{})$	steady state quantity
$(\vec{})$	vector quantity

SUMMARY

This dissertation presents the results of an experimental investigation undertaken to determine the effects of various nozzle design parameters on the capabilities of typical solid propellant rocket exhaust nozzles to attenuate axial combustion instabilities. The nozzles selected are representative of (a) a single-ported submerged rocket nozzle (RN-I) and (b) a multiple-ported rocket nozzle (RN-II). In pursuit of this objective several experimental studies were conducted with geometrically similar small-scale models of actual solid rocket nozzles. In addition to determining the attenuation provided by the small-scale models of the RN-I and RN-II nozzles, this investigation was also concerned with determining the dependence of solid rocket nozzle damping upon (a) the depth of the cavity surrounding a submerged nozzle, (b) the secondary flow rate issuing from the cavity of a submerged nozzle, (c) the geometry of the convergent section of a solid rocket nozzle, and (d) the number of nozzles present in a multiple-ported nozzle cluster. Finally, the criteria that should be used in scaling cold-flow, small-scale nozzle admittance data to real engine conditions were determined.

The nozzle attenuation was determined by measuring the nozzle admittance and these data were then used to determine the nozzle decay coefficients resulting from the use of the full-scale nozzles. The desired admittances were determined by measuring both the pressure amplitudes and phases at discrete locations along a modified impedance tube that simulated the oscillatory flow conditions in unstable rockets. In

this investigation the nozzles were tested under cold-flow conditions over a range of frequencies between 40 to 600 Hertz. This frequency range under cold-flow test conditions simulates, in general, the observed oscillatory flow conditions in unstable solid rockets.

The measured admittance data indicate that the damping provided by the RN-I and RN-II nozzles are independent of the frequency and that both of these nozzles provide little damping for axial instabilities. In the case of the submeged nozzle, combustion instability in the chamber excites wave motion in the cavity surrounding the nozzle. The depth of this cavity has a strong effect upon phase changes at the nozzle entrance plane but it exerts almost no effect upon wave attenuation. Also, the magnitude of the cavity-to-chamber flow rate ratio was found to have a negligible effect upon the measured submerged nozzle admittance.

The damping provided by short nozzles was found to be practically independent of the frequency and the geometrical details of the nozzle configuration and to be primarily dependent upon the nozzle area ratio. A comparison of the measured short nozzle admittance data with predictions of the "short nozzle" theory indicated that the theory underestimates the damping capabilities of short nozzles.

It has also been found that for a regular (i.e. not short) solid rocket nozzle with fixed values of entrance Mach number and the length of the convergent section, the damping provided by the nozzle can be increased by suitably redesigning the geometry of its convergent section. Tests conducted with conical, equal-radii-of-curvature and linear-velocity-profile nozzles showed that the conical nozzle provided the most damping. Test with multiple-ported solid rocket nozzles showed that the quadruple-

ported nozzle provided less damping for axial instabilities than the single- and dual-ported nozzles whose damping capabilities were approximately the same.

Finally, the scaling investigations showed that relevant nozzle damping data for both "short" and "long" full-scale nozzles can be obtained by investigating the behavior of geometrically similar small-scale nozzles.

CHAPTER I

INTRODUCTION

This investigation is concerned with the experimental evaluation of the capabilities of typical solid propellant rocket nozzles to attenuate axial combustion instabilities. The nozzles selected are representative of (a) a single-ported submerged rocket nozzle (henceforth referred to as RN-I) and (b) a multiple-ported rocket nozzle (henceforth referred to as RN-II). In pursuit of this objective several related experimental studies have been conducted. In the first of these studies, the attenuation provided by the RN-I and RN-II nozzles has been evaluated by determining the damping provided by small-scale models of the full-scale nozzles. Other studies undertaken in this investigation are concerned with evaluating the dependence of the nozzle attenuation upon (a) the depth of the cavity surrounding the submerged RN-I nozzle; (b) the secondary flow rate issuing from the cavity of the submerged RN-I nozzle; (c) the geometry of the convergent section of the RN-I nozzle; and (d) the number of nozzles in the RN-II nozzle cluster. Finally, this investigation has determined the scaling criteria which should be employed in the application of cold flow, small-scale nozzle damping test data in the design of full-scale rocket nozzles. This dissertation describes and discusses the results that have been obtained in the above-mentioned studies.

Background

Solid propellant rocket motors are often subject to combustion instabilities involving oscillations of the gases within the combustion chamber. Such instabilities can result in failure of the rocket motor and the mission due to large amplitude pressure oscillations, increased heat transfer rates, and severe vibrations of the engine structure.

Combustion instabilities occurring in solid propellant rocket motors are generally classified under three distinct categories based on the frequency of the oscillations. These categories are:[1]

(a) High-frequency instability.

(b) Intermediate-frequency instability.

(c) Low-frequency instability.

High-frequency instability is encountered in the frequency range[1] of 1000-100,000 Hertz. This type of instability generally corresponds to one of the transverse acoustic modes of the combustion chamber. The intermediate-frequency instability is generally encountered in large rocket motors[2] and it is characterized by frequencies ranging[1,2] from one hundred to several hundred Hertz. In contrast to the high-frequency instability, the intermediate-frequency instability oscillations generally correspond to one of the axial acoustic modes of the combustion chamber. Finally, the low-frequency instability occurs in the frequency range[1] of 1-100 Hertz and it is generally encountered during the operation of large rocket motors.

To date, several techniques have been used to suppress the above instabilities. Among these, the employment of powdered metals or metallic-oxides in the solid propellant[1] has proven effective in the suppression

of high-frequency combustion instabilities. However, experience with large size rocket motors (e.g., The Minuteman II Stage 3[2,3]) has indicated that such additives do not necessarily suppress the intermediate-frequency combustion instability. Currently, no reliable technique exists for suppressing this type of instability. Hence suppressing the intermediate-frequency combustion instability is currently a major consideration in the design and development of large solid rocket motors.[3,4]

The susceptibility of solid propellant rocket motors to combustion instability depends upon the wave energy balance between the various gain and loss mechanisms that are present in the system. The primary source of wave energy gain is the combustion process. Energy loss mechanisms are provided by the mean flow, dissipative processes such as viscosity and heat transfer, relaxation processes in the gas phase, nozzle acoustic losses, and the particulate and structural damping. A meaningful stability analysis of a solid propellant rocket motor would thus involve a quantitative evaluation of all the wave energy gains and losses pertaining to a particular system. To evaluate nozzle damping or wave energy losses in the nozzle, the admittance at the nozzle entrance must be determined. The admittance is defined as the ratio of the axial velocity perturbation to the pressure perturbation when both are expressed as complex numbers. The nozzle admittance is also needed in linear stability analyses where it is used as the boundary condition that must be satisfied at the nozzle end of the combustion chamber.

The theoretical determination of the nozzle admittance is a difficult gas dynamical problem which requires the solution of a mathematically complex system of conservation equations which describe the behavior of the flow oscillations in the convergent section of the nozzle.

Available theoretical treatments for computing the nozzle admittance are complex in nature, and, to date, solutions have been obtained only for a limited number of cases. The most sophisticated treatment of the nozzle admittance problem was developed by Crocco and Sirignano[5], who considered the case where the wave motion in the nozzle is three-dimensional and the mean flow is one-dimensional. The latter assumption implies a slowly converging nozzle. This theory indicates that the nozzle admittance is a function of the gradients of the mean flow properties in the convergent section of the nozzle, the frequency and mode of oscillation, and the value of the steady state Mach number at the nozzle entrance. With the exception of the frequency and mode of oscillation, the remaining parameters are controlled by the geometry of the convergent section of the nozzle. This theoretical treatment is also applicable to cases where both the wave motion and the steady state flow are one-dimensional. In separate theoretical treatments[6,7] the special case where the length of the nozzle convergent section is small, when compared to the chamber length, has been considered. These studies show that the admittance of a "short nozzle" depends only on the value of the steady state Mach number at the nozzle entrance. Since existing nozzle theories widely vary in scope and complexity, it is important to determine the conditions under which the results of these theories may be used in stability analyses and in the determination of nozzle damping capabilities. In this investigation, the applicability of the theoretical analyses is investigated by comparing their predictions with measured nozzle admittance data.

There are several experimental techniques that could be used to

determine the damping capabilities of a nozzle. These are often referred to as the direct, wave-attenuation, frequency response, and standing wave methods. A brief description of each of these methods follows:

(1) In the direct technique[8] a hot wire anemometer probe and a pressure transducer are installed in the entrance plane of the nozzle. The nozzle admittance is determined from direct measurements of the amplitudes and phases of the axial flow velocity and pressure oscillations at the nozzle entrance. However, experimental difficulties and inaccuracies that are associated with the measurements of the velocity perturbation reduce the quality of the measured nozzle admittances.

(2) In the wave-attenuation or decay technique[9] a pressure pulse is superimposed on a steady flow in a simulated chamber by bursting a diaphragm at the upstream end of the chamber. The decay rate of the resulting pressure pulse is measured and this data is used to determine the nozzle admittance. This technique is limited to investigations of nozzles having relatively small values of the ratio of the nozzle throat area to the chamber cross-sectional area because large values of this ratio result in extremely fast damping and high background flow noise. This method assumes that the observed decay is solely due to nozzle damping; a rather questionable assumption. Since the decaying pulse oscillates at the resonant frequency of the chamber, the measured admittance is only applicable to this particular frequency. To evaluate the admittance at other frequencies the chamber length must be modified; a requirement that considerably detracts from the attractiveness of this method in situations where nozzle response over a wide frequency range

is needed.

(3) In the frequency response or steady state resonance technique[9,10] an acoustic wave of a known frequency is excited in a simulated rocket combustion chamber. The frequency of the oscillations is slowly varied over a range of frequencies starting with a frequency below one of the resonant frequencies of the chamber and ending at a frequency above the chosen resonant frequency. The amplitudes of the resulting pressure oscillations are measured and plotted as a function of the driving frequency. From the shape of the resulting acoustic response curve the nozzle admittance at the chosen resonant frequency can be determined. This method suffers from most of the shortcomings that limit the applicability of the wave-attenuation method. In addition the analysis of Culick and Dehority[11] indicates that the frequency response technique can only be used to measure the damping of nozzles whose admittances are independent of the frequency.

(4) The standing wave or modified impedance tube technique is an extension of the classical, no flow, impedance tube method[12,13,14] employed to measure the acoustical damping capabilities of various materials. In the classical impedance tube technique, a sound source capable of generating a wave of desired waveform and frequency is placed at one end of a tube. The other end of the tube is terminated with a sample of the material whose damping capabilities or admittances are to be measured. A standing wave pattern of a given frequency is excited in the tube, and a microphone probe is traversed along the tube to measure the axial variation of the standing wave amplitude. The damping capability of the material can then be determined by measuring (a) the dis-

tance of the first pressure amplitude minimum or maximum from the tested sample and (b) the ratio of the maximum pressure amplitude to the minimum pressure amplitude. The frequency dependence of the admittance of the tested sample may be determined by repeating the experiment at different frequencies. In this experiment, changing the frequency merely involves changing the frequency of the generated wave; a process that is considerably simpler than the modifications required in the wave-attenuation or resonance experiments.

The applicability of the various experimental techniques for measuring nozzle admittances has been investigated by Culick and Dehority[11]. One of the important results of this study has been the conclusion that the impedance tube method appears to be the most suitable technique for the measurement of nozzle admittances. A similar conclusion has also been reached independently by Bell[15]. References 11 and 15 derive the equations and discuss the experimental setup required to measure nozzle admittances in an impedance tube containing a steady one-dimensional mean flow. Due to the presence of a mean flow, the method used in these experiments has often been referred to as the Modified Impedance Tube technique. In related studies by Bell[15] and Zinn et al.,[16] the experimental determination of the admittances of liquid propellant rocket nozzles subjected to three-dimensional pressure oscillations is discussed. In these studies the three-dimensional nozzle admittances are determined by measuring the amplitudes of a standing three-dimensional pressure pattern at a number of preselected locations along the modified impedance tube. In this connection it should be pointed out that the experimental nozzle admittance data obtained in these studies are in agreement

with the theoretical predictions obtained using Crocco's nozzle admittance theory[5]. In view of the conclusions derived in References 11 and 15, and the results described in Reference 16, it was decided to use the modified impedance tube method in the studies that were conducted under this investigation.

Objectives

In this dissertation, five related experimental studies have been undertaken and the objectives of each of the studies are stated below:

Study 1: Determine the attenuation provided by the RN-I and RN-II nozzles by measuring the damping provided by small-scale models of the full-scale nozzles.

Study 2: Determine the scaling rules that should be employed when cold flow, small-scale nozzle damping results are used in the design of full-scale nozzles.

Study 3: Determine the dependence of the admittance of the submerged RN-I nozzle upon (a) the depth of the cavity surrounding the nozzle and (b) the secondary flow rate issuing from the cavity surrounding the nozzle.

Study 4: Determine the dependence of the admittances of solid rocket nozzles upon the geometry of their convergent sections.

Study 5: Determine the dependence of the admittance of multiple-ported rocket nozzles upon the number of nozzles present in the nozzle cluster.

A summary of the theory and the pertinent equations required for the determination of nozzle admittances and nozzle decay coefficients is presented in Chapter II. Descriptions of the experimental facility, the

scaling procedure adopted for designing the experimental small-scale nozzles, the nozzle configurations, and the experimental procedure are presented in Chapter III. The measured nozzle admittance data are presented and discussed in Chapter IV. A summary of the results, conclusions, and recommendations for future work are presented in Chapter V.

CHAPTER II

ANALYTICAL CONSIDERATIONS

Introduction

The equations required for the measurement of nozzle admittances in a modified impedance tube experiment are derived in detail in References 11 and 15. Only a qualitative description of the theory and a summary of relevant expressions will be presented in this chapter. The expressions needed for the experimental determination of the nozzle admittance are obtained from solutions of differential equations describing the driven oscillatory flow conditions inside a simulated, cold-flow rocket combustor. These solutions are then required to satisfy the admittance boundary condition at the nozzle entrance. When this portion of the analysis is completed, the resulting expressions for the pressure amplitude $|P_1|$ and the pressure phase δ are found to be functions of the steady state properties of the medium, the axial coordinate, the known frequency, and the two parameters α and β that describe the as yet unknown nozzle admittance. The availability of such expressions for the pressure amplitude and pressure phase suggest that if one can measure the pressure amplitude and/or pressure phase at various locations along the chamber, then the experimental data could be substituted into the theoretical expressions for the pressure amplitude and/or pressure phase and the resulting algebraic equations could then be solved to determine the unknowns of the problem; that is, the parameters α and β which characterize the nozzle admittance. The measured nozzle admittance may

then be used to compute the nozzle decay coefficient, which is a parameter often used by industry to describe the nozzle damping capabilities. The expression required for the computation of the nozzle decay coefficient α_N from the measured admittance data is developed later on in this chapter.

Nozzle Admittance

The specific nozzle admittance, Y_N, defined as

$$Y_N = \frac{u_1}{p_1} \tag{2-1}$$

represents the boundary condition that the solutions for the axial velocity perturbation u_1 and pressure perturbation p_1 must satisfy at the nozzle entrance. In general, the nozzle admittance is a complex number whose real and imaginary parts describe the relationships that exist at the nozzle entrance between the amplitudes and phases of the velocity and pressure perturbations. These relationships depend upon the wave motion inside the convergent section of the nozzle.

When a wave generated inside a combustor enters the nozzle, the presence of convergent walls and gradients of mean flow properties result in continuous reflection and refraction of the wave as it moves through the convergent section of the nozzle. When such a wave reaches the nozzle throat, where the flow is sonic, an upstream propagation can no longer occur and the wave moves through the throat into the divergent portion of the nozzle. The complex processes taking place inside the convergent section of the nozzle result in both amplitude and phase

differences between the incident and reflected pressure waves at the nozzle entrance. It can be shown (e.g., see Reference 15) that the magnitude of these differences can also be described by the nozzle admittance.

The expressions required for the calculation of the nozzle admittance are obtained by solving the system of conservation equations that describe the behavior of small amplitude, one-dimensional disturbances which are superimposed upon a steady one-dimensional flow field inside a simulated cold flow rocket combustor. The simulated combustor has an acoustic driver at one end of the chamber and a choked nozzle at the other end. The above-mentioned solutions are then required to satisfy the admittance boundary condition at the nozzle entrance. The resulting expressions (see Reference 15 for detailed derivations of these solutions) describing the time and space dependence of the pressure and velocity perturbations inside the simulated combustor are given below:

$$p_1(z,t) = \gamma \bar{p} \hat{A}\, e^{i(\omega t + az)} \cosh(\phi - iRz) \tag{2-2}$$

$$u_1(z,t) = c \hat{A}\, e^{i(\omega t + az)} \sinh(\phi - iRz) \tag{2-3}$$

where

$$a = \frac{(\omega/\bar{c})\bar{M}}{(1 - \bar{M}^2)}$$

$$R = \frac{(\omega/\bar{c})}{(1 - \bar{M}^2)}$$

$$\phi = \pi\alpha - i\pi \left[\beta + \frac{2(L_c - z)}{\lambda} + \tfrac{1}{2} \right] \tag{2-4}$$

and

$$\lambda = \frac{2\pi(1 - \bar{M}^2)}{(\omega/\bar{c})} \tag{2-5}$$

The admittance parameters α and β describe the previously mentioned relationships between the amplitudes and phases of the incident and reflected pressure waves at the nozzle entrance. It can be shown[17] that

$$\left[\frac{\text{Amplitude of Reflected Pressure Wave}}{\text{Amplitude of Incident Pressure Wave}}\right]_{\substack{\text{nozzle} \\ \text{entrance}}} = e^{-2\pi\alpha} \tag{2-6}$$

and that the phase change, θ, between the incident and reflected pressure waves at the nozzle entrance is described by the following expression:

$$\theta = \pi(1 + 2\beta) \; ; \; -0.5 \leq \beta \leq 0.5 \tag{2-7}$$

The nondimensional form of the specific nozzle admittance can be written in the following form:

$$y_N = \frac{Y_N}{Y_g} = \left(\frac{\bar{\rho}\bar{c}}{g}\right)\left(\frac{u_1}{p_1}\right)_{z\,=\,0} = \Gamma + i\eta \tag{2-8}$$

where the reference admittance $Y_g = (g/\bar{\rho}\bar{c})$ is the characteristic admittance of the gas medium in the chamber. The conversion factor g which is included in the definition of Y_g will be omitted from the following discussion. Consequently, the density $\bar{\rho}$ must be expressed in the units $lb_f sec^2/ft^4$ whenever it appears in the definition of the characteristic admittance of the gas; that is, $1/\bar{\rho}\bar{c}$.

Substituting the solutions obtained for the pressure and velocity perturbations (i.e., Equations (2-2) and (2-3)) into the above defination gives the following expression[18] for the nondimensional nozzle admittance y_N:

$$y_N = \coth \pi(\alpha - i\beta) \tag{2-9}$$

Separating the nondimensional nozzle admittance into its real and imaginary parts, the following relations are obtained:

$$\Gamma = \frac{\tanh(\pi\alpha)\ \sec^2(\pi\beta)}{\tanh^2(\pi\alpha) + \tan^2(\pi\beta)} \tag{2-10}$$

$$\eta = \frac{\operatorname{sech}^2(\pi\alpha)\ \tan(\pi\beta)}{\tanh^2(\pi\alpha) + \tan^2(\pi\beta)} \tag{2-11}$$

Examination of Equations (2-8) through (2-11) shows that the nondimensional nozzle admittance depends upon the steady state properties of the flow and the parameters α and β.

It remains to be determined how α and β can be evaluated from pressure amplitude or pressure phase measurements inside a simulated, cold-flow rocket combustor. To accomplish this, Equation (2-2) is rewritten in the following form:

$$p_1(z,t) = |P_1(z)|\ e^{i(\delta + \omega t)} \tag{2-12}$$

where the pressure amplitude $|P_1(z)|$ is given by

$$|P_1(z)| = P_t = A\left[\cosh^2(\pi\alpha) - \cos^2\pi\left\{\beta + \frac{2z}{\lambda}\right\}\right]^{\frac{1}{2}} \tag{2-13}$$

and the pressure phase δ is given by

$$\delta(z) = az + \text{Arctan}\left[\frac{\tanh(\pi\alpha)}{\tan \pi(\beta + \frac{2z}{\lambda})}\right] \qquad (2\text{-}14)$$

Equations (2-13) and (2-14) show that the pressure amplitude $|P_1|$ and pressure phase δ are functions of the axial coordinate, the steady state properties of the medium, the known frequency and the unknowns α, β, and A. This functional dependence suggests that the unknowns α and β can be evaluated from either pressure amplitude measurements or pressure phase measurements taken at three different locations along the length of the simulated chamber. In this investigation the admittance parameters α and β were determined by measuring both the pressure amplitudes and phases. The resulting values of α and β were then substituted into Equations (2-9) through (2-11) to determine the nozzle admittance.

Since the expressions relating $|P_1|$ and δ to admittance parameters α and β are nonlinear, pressure amplitude or pressure phase measurements taken at only three discrete axial locations may not guarantee the uniqueness and accuracy of the calculated values of α and β. Stated differently, pressure amplitude or phase measurements taken at three locations along the standing wave pattern will not yield enough information about the shape of the standing wave pattern inside the simulated chamber. These points are further discussed in Appendix A. Hence, in this investigation ten transducers, located at different locations along the chamber, are used to measure the pressure amplitudes and phases. The measured data are then used to compute the desired values of the admittance parameters α and β using the method of Nonlinear Regression[15] (NLR). The method of NLR consists of determining those values of α and

β which give the best fit between the measured pressure amplitude and phase data and the corresponding theoretical predictions as obtained from Equations (2-13) and (2-14).

To obtain values of the admittance parameters α and β from pressure amplitude measurements, the method of NLR is used to determine the set of values A, α, and β that minimize the root-mean-square deviation between the experimental data and the corresponding theoretical pressure amplitudes obtained from Equation (2-13). To compute this set of values of A, α, and β a quantity E defined as

$$E = \sum_{i=1}^{10} \left[P_E(z_i) - P_t(z_i, \alpha, \beta, A, \omega, M...) \right]^2 \qquad (2\text{-}15)$$

is minimized. In Equation (2-15), the quantity $P_E(z_i)$ represents the experimental value of the pressure amplitude measured at location z_i and $P_t(z_i, \alpha, \beta, \omega, M...)$ is the corresponding theoretical amplitude evaluated by use of Equation (2-13). The NLR technique calculates the values of A, α, and β that minimize the quantity E by solving a system of nonlinear algebraic equations which are generated by taking a partial derivative of E with respect to each of the three unknown parameters and then equating the resulting expression to zero; that is,

$$\frac{\partial E}{\partial A} = 0 \; ; \; \frac{\partial E}{\partial \alpha} = 0 \; ; \; \frac{\partial E}{\partial \beta} = 0 \qquad (2\text{-}16)$$

The resulting values of A, α, and β determine the minimum value of the surface $E(A, \alpha, \beta)$.

Optimum values of the admittance parameters can also be determined from pressure phase measurements. This is achieved by using the method

of NLR to determine the set of values of α and β that minimizes the root-mean-square deviation between the experimental phase data and the theoretical phases obtained from Equation (2-14). To compute the required set of values of α and β a quantity F defined as

$$F = \sum_{i=1}^{10} [\delta_E(z_i) - \delta_t(z_i,\alpha,\beta,\omega,M...)]^2 \qquad (2\text{-}17)$$

is minimized. In this expression, the quantity $\delta_E(z_i)$ is the measured pressure phase at location z_i and $\delta_t(z_i,\alpha,\beta,\omega,M...)$ is the corresponding theoretical pressure phase as determined using Equation (2-14). The values of α and β that minimize the quantity F are determined by solving the system of nonlinear algebraic equations obtained by taking partial derivatives of F with respect to the unknown parameters α and β and then equating the resulting equations to zero; that is,

$$\frac{\partial F}{\partial \alpha} = 0 \; ; \; \frac{\partial F}{\partial \beta} = 0 \qquad (2\text{-}18)$$

As mentioned earlier, the optimum values of the admittance parameters α and β are determined in this investigation from both the pressure amplitude and pressure phase measurements. The real and imaginary parts of the non-dimensional nozzle admittance ratio, y_N, are then determined by substituting the computed values of α and β into Equations (2-10) and (2-11). Additional details on the use of the NLR technique and the associated computer programs are given in Reference 15.

Nozzle Decay Coefficient

In practice[3,19,20], the overall stability of solid propellant

rocket motors is often determined by evaluating a coefficient α_{gd} that describes the rate of growth or decay of a small amplitude oscillation inside the combustor. The sign of α_{gd} determines whether the oscillation will grow or decay with time. The coefficient α_{gd} can be expressed as a summation, $\sum_i \alpha_i$, where the components α_i represent the contributions of the various relevant processes (e.g., combustion, flow in the nozzle) to the stability of the rocket combustor. This section is concerned with the evaluation of the quantity α_N that may be regarded as a measure of the damping provided by the nozzle. When the nozzle is the only factor that can affect the growth or decay of an oscillation inside the combustor, the temporal behavior of the combustor oscillation may be expressed in the following form:

$$p_1(z,t) = P(z)e^{\alpha_N t} e^{i\omega t} \tag{2-19}$$

The following discussion will outline how the measured nozzle admittance data can be used to measure the nozzle decay coefficient.

According to Reference 21, the nozzle decay coefficient may be determined from the following relationship:

$$2\alpha_N \hat{V} = - < \int_{\substack{\text{nozzle}\\\text{entrance}}} d\vec{S}_n \cdot \left\{ p_1 \vec{u}_1 + \frac{\bar{\vec{M}}}{\bar{\rho}\bar{c}} p_1^2 \right.$$

$$\left. + \bar{\rho}\bar{c}(\bar{\vec{M}}\cdot\vec{u}_1)\,\vec{u}_1 + (\bar{\vec{M}}\cdot\vec{u}_1)\,p_1\bar{\vec{M}} \right\} > \tag{2-20}$$

where

$$\hat{V} = < \int_{\substack{\text{combustor}\\\text{volume}}} dV \left\{ \tfrac{1}{2}\bar{\rho}\vec{u}_1\cdot\vec{u}_1 + \tfrac{1}{2}\frac{p_1^2}{\bar{\rho}\bar{c}^2} + \frac{\bar{\vec{u}}\cdot\vec{u}_1}{\bar{c}^2} p_1 \right\} > \tag{2-21}$$

and the time average $< >$ is defined as follows:

$$< > = \lim_{T\to\infty} \frac{1}{T} \int_0^T ( ) \, dt \tag{2-22}$$

Implied in Equations (2-20) and (2-21) is the assumption that the growth or decay rate of the oscillations is small. It should also be pointed out that in order to evaluate the nozzle decay coefficient using Equations (2-20) and (2-21), the acoustic mode structure (i.e., $p_1(z,t)$ and $\underset{\rightarrow}{u}_1(z,t)$) and the steady state flow conditions throughout the chamber must be known. Substituting the expression for the nozzle admittance Y_N (defined in Equation (2-1)), into Equation (2-20) and rearranging yield the following expression:

$$2\alpha_N \hat{V} = - \int_{\substack{\text{nozzle} \\ \text{entrance}}} dS \left|P_N\right|^2 \left[(1 + \bar{M}^2) \, \mathrm{Re}\left\{ Y_N \right\} + \frac{\bar{M}}{\bar{\rho}\bar{c}} + \bar{\rho}\bar{c}\bar{M} \left|Y_N\right|^2 \right] \tag{2-23}$$

where $\left|P_N\right|$ is the amplitude of the pressure oscillation at the nozzle entrance. The relationship $\underset{\rightarrow}{\bar{M}} \cdot \underset{\rightarrow}{n} = \bar{M}$ and $\underset{\rightarrow}{u}_1 \cdot \underset{\rightarrow}{n} = u_1$, where now $\bar{M}$ and u_1 should be interpreted as the components of the steady state Mach number and velocity perturbation in the direction of the normal $\underset{\rightarrow}{n}$, were used in the derivation of Equation (2-23). Assuming uniform flow conditions at the nozzle entrance plane, Equation (2-23) can be rewritten as follows:

$$\left(\frac{2\bar{\rho}\bar{c}\hat{V}}{S_N \left|P_N\right|^2} \right) \alpha_N = - \left[(1 + \bar{M}^2) \, \mathrm{Re}\left\{ y_N \right\} + \bar{M} + \bar{M} \left| y_N \right|^2 \right] \tag{2-24}$$

The right-hand side of Equation (2-24) consists of four terms, three of

which depend upon the steady flow Mach number at the nozzle entrance. These three terms may be considered as representing wave energy losses resulting from the presence of a mean flow and the remaining term is the radiative wave energy loss. For later reference, it should be pointed out that both sides of Equation (2-24) are nondimensional. When $|y_N|$ and $\bar{M}$ are much smaller than 1, then Equation (2-24) can be simplified to the following form:

$$\left(\frac{2\bar{\rho}\bar{c}\hat{V}}{S_N|P_N|^2}\right)\alpha_N = -\left[\bar{M} + \mathrm{Re}\left\{y_N\right\}\right] \tag{2-25}$$

In some investigations of combustion instability in solid propellant rocket motors[22] the following definition of nondimensional nozzle admittance is used:

$$A_N = \left(\frac{\gamma\bar{P}}{\bar{u}}\right)\frac{u_1}{p_1} = \left(\frac{\gamma\bar{P}}{\bar{u}}\right)Y_N \tag{2-26}$$

Substituting Equation (2-26) into Equation (2-23), rearranging terms, and assuming that the flow conditions across the nozzle entrance are uniform yield the following result:

$$\left(\frac{2\bar{\rho}\bar{c}\hat{V}}{S_N|P_N|^2}\right)\alpha_N = -\bar{M}\left[(1+\bar{M}^2)\,\mathrm{Re}\left\{A_N\right\} + \bar{M}^2|A_N|^2 + 1\right] \tag{2-27}$$

where A_N is the modified admittance, defined in Equation (2-26), evaluated at the nozzle entrance. Assuming that $|A_N|$ is a quantity of order one or smaller and that $\bar{M}^2 \ll 1$, Equation (2-27) may be simplified to

the following form:

$$\left(\frac{2\bar{\rho}\bar{c}\hat{V}}{S_N|P_N|^2}\right)\alpha_N = -\bar{M}\left[\mathrm{Re}\left\{A_N\right\} + 1\right] \tag{2-28}$$

which is equivalent to the relationship used in Reference 22 to evaluate the nozzle decay coefficient.

To proceed with the determination of the nozzle decay coefficient α_N, for a cylindrical chamber subject to axial instabilities, the real parts of p_1 and u_1 obtained from Equations (2-2) and (2-3) are substituted into Equations (2-20) and (2-21) and the indicated space integration and time averaging are performed (see Appendix B for details). These manipulations yield the following expression for the nondimensional nozzle decay coefficient Λ_N:

$$\Lambda_N = \left(\frac{\alpha_N L_c}{\bar{c}}\right) = -\left[\frac{\bar{M} + \left(\frac{1+\bar{M}^2}{2}\right)\tanh(2\pi\alpha)}{1 + \bar{M}\tanh(2\pi\alpha)}\right] \tag{2-29}$$

An examination of Equation (2-29) indicates that for the case under consideration, the nondimensional nozzle decay coefficient is a function of the mean flow Mach number $\bar{M}$ and the admittance parameter α. Inspection of Equation (2-6) shows that the parameter α describes the wave amplitude changes at the nozzle entrance, and the latter may be related to the corresponding wave energy changes between the incident and reflected waves. When both $\bar{M}$ and α are small quantities, Equation (2-29) reduces to the following approximate form:

$$\Lambda_N = -\left[\bar{M} + \pi\alpha\right] \tag{2-30}$$

Using Equations (2-10) and (2-30), it can be shown that in the special case when $\beta \simeq \frac{1}{2}$ (i.e., when the nozzle entrance "acts" like a solid wall) the expression for the nozzle decay coefficient reduces to the following approximate form:

$$\Lambda_N = -\left[\bar{M} + \mathrm{Re}\left\{y_N\right\}\right] = -\left[\bar{M} + \Gamma\right] \tag{2-31}$$

When $\bar{M}$ is small, the following relationship[23]

$$\bar{M} \simeq \left(\frac{2}{\gamma + 1}\right)^{\frac{\gamma + 1}{2(\gamma - 1)}} J \tag{2-32}$$

where J is $S_{throat}/S_{chamber}$ holds. In the case of air, the specific heat ratio γ equals 1.4 and Equations (2-30) and (2-32) can be combined to give

$$\Lambda_N = -\left[0.58J + \pi\alpha\right] \tag{2-33}$$

Examination of Equations (2-29) through (2-33) shows that the nozzle decay coefficient is directly proportional to the mean flow Mach number $\bar{M}$ as well as the real part of the nondimensional nozzle admittance Γ. The former represents mean flow effects while the latter represents energy losses due to acoustic energy radiation through the nozzle. Equation (2-30) indicates that increasing both α and $\bar{M}$ will increase the chamber's decay coefficient. However, in contemplating such changes in actual systems one should also consider how these changes may affect other gain or loss mechanisms that are present in the system. For example, increasing $\bar{M}$ may, in addition to increasing nozzle losses, also

increase the gain due to the combustion process. The latter increase in gain may be equal to or larger than the increased nozzle loss and thus result in a more unstable system. Also changing $\bar{M}$ may interfere with other engine design considerations such as grain configuration and propellant properties. Hence it appears that a simpler and safer way to increase nozzle losses would be through nozzle design modifications that will result in an increase in the acoustic energy radiation through the nozzle.

Scaling of Nozzle Admittance Data

Considerations of scaling of nozzle admittance data give rise to the following two questions: (a) what nozzle design features should be reproduced in a small-scale experiment designed to yield meaningful nozzle admittance data, and (b) how can nozzle admittance data, measured in cold flow, small-scale experiments, be used to predict the behavior of full-scale nozzles under normal engine operating conditions? To answer these questions one should determine what variables actually determine the nozzle admittance and then attempt to simulate these variables in a small-scale experiment. To determine these variables one must consult the analyses that are concerned with the prediction of the nozzle admittance.

The nozzle admittance studies of Crocco[5] indicate that for longitudinal mode oscillations the nozzle admittance depends on the nondimensional frequency S, defined as $\omega r_c/\bar{c}$, the axial distribution of the steady state Mach number in the convergent section of the nozzle, and the specific heat ratio. Since the values of the specific heat ratios for different fluids do not differ considerably from each other, Crocco's analysis suggests that, in general, the nondimensional frequency and the

mean flow Mach number distribution are the parameters that should be duplicated in the design of small-scale nozzles to be employed in experimental nozzle admittance studies. Crocco's analysis also indicates that the admittance data of a reference nozzle with a given entrance Mach number can be used to obtain the admittance data of a "family" of nozzles having the same entrance Mach number and designed by a linear "contraction" or "stretching" of the reference nozzle. If z_{ref} is the length of the convergent section of the reference nozzle and z_f is the corresponding length of the modified nozzle obtained by "stretching" or "contracting" the reference nozzle, then a scale factor σ can be defined as

$$\sigma = \frac{z_f}{z_{ref}} \tag{2-34}$$

Then, according to Crocco's analysis, the nondimensional admittance of the modified nozzle is obtained from the following relationship:

$$\left[(y_N)_f\right]_{S = S_f} = \left[(y_N)_{ref}\right]_{S = S_{ref}} \tag{2-35}$$

whose S_f is given by S_{ref}/σ. The geometrical relationships between the reference and modified nozzles are illustrated in Figure 1. Examination of this figure indicates that the modified and actual nozzles have similar conical sections but different radii of curvature at the nozzle throat and entrance sections. According to Crocco, the error introduced due to this difference in the shapes of the two nozzles is expected to be negligible.

Since, in general, the lengths of the convergent sections of

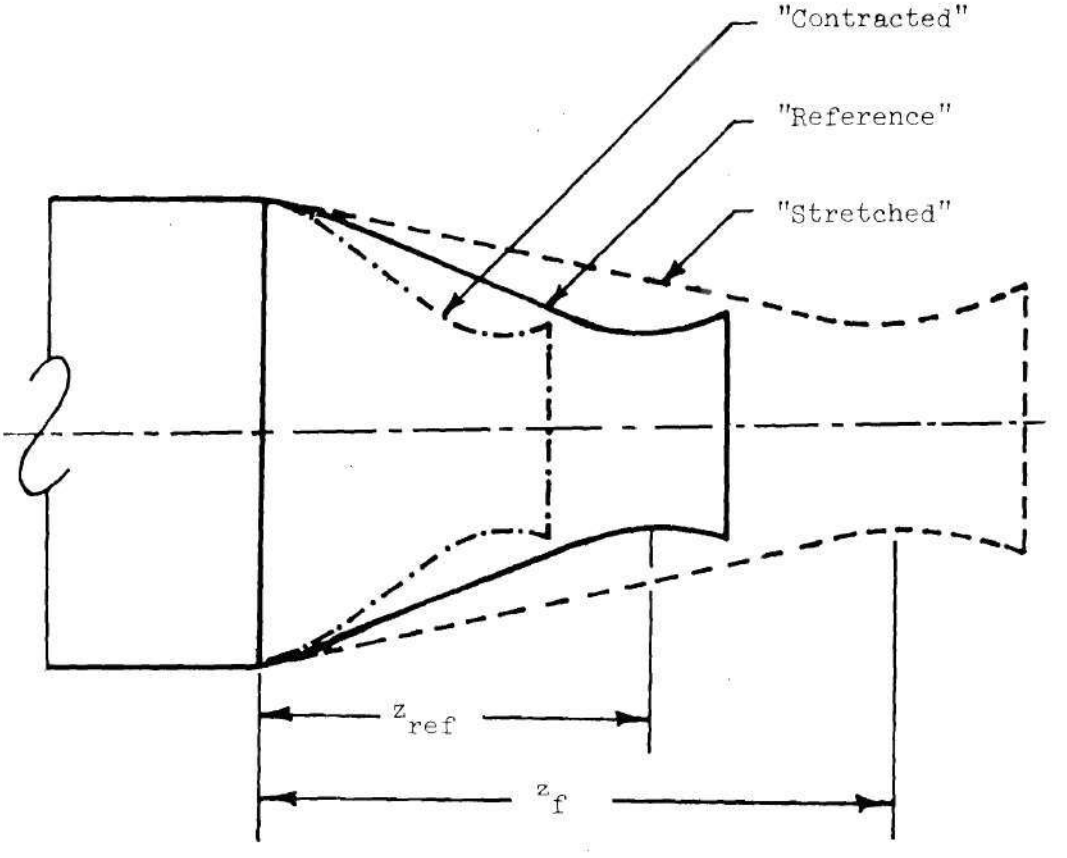

Figure 1. "Family" of Scaled Nozzles.

solid propellant rocket nozzles are considerably shorter than the wavelength of the oscillation, the results of References 6 and 7 that investigate the admittances of short nozzles, also need to be considered in the present discussion. According to these references, the nondimensional nozzle admittance y_N can be expressed as follows:

$$y_N = (\bar{\rho}\bar{c})Y_N = \left(\frac{\gamma - 1}{2}\right)\bar{M} \qquad (2\text{-}36)$$

It follows from Equation (2-36) that in the case of short nozzles the specific heat ratio γ and the mean flow Mach number at the nozzle entrance are the only nondimensional parameters that should be reproduced in small-scale experiments designed to measure nozzle admittances. Since variations in the values of γ between different fluids are relatively small, one might expect that perhaps $\bar{M}$ is the only nondimensional parameter that should be reproduced in the small-scale experiments. Intuition and the previously-mentioned results of Reference 5 also suggest that the full-scale and small-scale nozzles should be similar in the sense that the axial distributions of the steady state Mach numbers in the full-scale and small-scale nozzles are the same. Adopting the latter criterion results in geometric similarity between the full-scale and small-scale nozzles. Whenever possible, this criterion has been used as a guide in the design of the small-scale nozzles tested in this investigation. Equation (2-36) also indicates that the measured nozzle admittance Y_N should be normalized with respect to the admittance of the medium $(1/\bar{\rho}\bar{c})$ and that the measured admittance should be independent of the frequency as long as the short nozzle assumption is satisfied.

Next, the scaling of cold flow nozzle admittance data to actual systems will be considered. The above discussion suggests that the short nozzle admittance data should be presented as plots of y_N versus $\bar{M}$. In applying this data to actual systems, one needs to verify that the actual nozzle is geometrically similar to the small-scale nozzle and that the dimensions of the actual nozzle satisfy the short nozzle criterion requiring that $L_N/\lambda \ll 1$. In this case L_N is a characteristic nozzle dimension and λ is the wavelength of the unstable oscillation. In addition, to obtain data that is applicable to actual systems the cold flow experiments should be conducted over a range of frequencies whose wavelengths are equal to wavelengths observed during axial instabilities inside the actual engines. The restriction on wavelengths results in the following relationship, when $\bar{M}^2 \ll 1$:

$$\lambda_A = \lambda_E = \frac{2\pi\bar{c}_A}{\omega_A} = \frac{2\pi\bar{c}_E}{\omega_E} \tag{2-37}$$

Once these criteria have been verified, one can obtain the admittance of the actual nozzle from the relationship

$$\left(Y_N\right)_A = \frac{\bar{\rho}_E\bar{c}_E}{\bar{\rho}_A\bar{c}_A}\left(Y_N\right)_E \tag{2-38}$$

where $(\bar{\rho}\bar{c}Y_N)_E$ is the experimentally determined nondimensional admittance, $(Y_N)_A$ is the admittance of the actual nozzle, and $1/\bar{\rho}_A\bar{c}_A$ is the specific admittance of the medium in the "hot" or actual engine.

Next, the determination of the nozzle decay coefficient α_N of actual engines from nozzle admittance data, measured in small-scale cold

flow experiments, will be discussed. For this purpose it will be instructive to consider Equation (2-25) or Equation (2-28) that provide analytical expressions for calculating α_N for combustors with low values of $\bar{M}$. Both sides of Equation (2-25) are nondimensional, and the quantity on the left-hand side may be considered as a parameter describing the acoustics of the combustor, while the expression on the right-hand side of the equation may be considered as describing the acoustic properties of the nozzle. Suppose two nozzles having the same admittances y_N and the same mean flow Mach numbers $\bar{M}$, at their entrances, are attached to two different combustors, and suppose one would like to determine the nozzle decay coefficient of one of these combustors by investigating the behavior of the other combustor, which in this discussion will be taken to be the cold flow, small-scale chamber used in the present program. Equation (2-25) can be applied to both systems in order to determine their α_N. However, since the nozzles of both systems are assumed to be identical, then the right-hand side of Equation (2-25) will be the same for both engines, and one can write

$$\left(\frac{\bar{\rho}\bar{c}\alpha_N\hat{V}}{S_N|P_N|^2}\right)_A = \left(\frac{\bar{\rho}\bar{c}\alpha_N\hat{V}}{S_N|P_N|^2}\right)_E \tag{2-39}$$

where the subscripts A and E represent quantities related to the actual and experimental engines, respectively. Rearrangine Equation (2-39) yields

$$(\alpha_N)_A = \frac{\bar{\rho}_E\bar{c}_E}{\bar{\rho}_A\bar{c}_A}\frac{(S_N)_A}{(S_N)_E}\frac{\left(\hat{V}/|P_N|^2\right)_E}{\left(\hat{V}/|P_N|^2\right)_A}(\alpha_N)_E \tag{2-40}$$

Examination of Equation (2-27) shows that the scaling of nozzle decay coefficient data depends upon knowledge of the specific acoustic impedances $\bar{\rho}\bar{c}$ of both media at the nozzle entrances, knowledge of nozzle entrance area S_N, and knowledge of the structures of the acoustic modes inside the combustors as represented by the parameter $\hat{V}/|P_N|^2$. In actual practice it may be more convenient to calculate the desired α_N directly from Equation (2-25). In this case one can substitute the experimentally measured value of y_N into Equation (2-25) and the remainder of the needed information must be supplied from other sources. Determination of the specific acoustic impedance requires knowledge of the actual temperature and composition of the gases at the nozzle entrance, and the determination of the parameter $\hat{V}/|P_N|^2$ requires knowledge of the acoustic mode structure inside the combustor. While the parameter $\hat{V}/|P_N|^2$ can be easily determined for relatively simple acoustical systems (e.g., see Appendix B), its determination for the complex geometries with mean flows found in actual solid propellant rockets, is a formidable if not an impossible task. When the oscillations in the actual engine and experimental setup are longitudinal, the nozzle decay coefficient for the actual engine can be obtained from measured cold flow decay coefficients by using Equation (2-29) or the following relationship:

$$(\alpha_N)_A = \frac{(L_c)_E}{(L_c)_A} \frac{(\bar{c})_A}{(\bar{c})_E} (\alpha_N)_E \qquad (2\text{-}41)$$

Before leaving this section, it should be pointed out that the formulae for the determination of α_N are based on knowledge of the non-

dimensional nozzle admittance y_N. However, nozzle admittance data is usually obtained in experiments where the amplitude of the chamber oscillation neither grows nor decays with time. When one uses such an admittance to compute the nozzle decay coefficient, one is implicitly assuming that the available nozzle admittance, which was measured under conditions of constant wave amplitude, is also applicable to situations in which the amplitude of the oscillation changes with time. The applicability of this assumption is open to question.

CHAPTER III

EXPERIMENTAL APPARATUS

Introduction

In this investigation the damping capabilities of solid rocket exhaust nozzles have been measured using the modified impedance tube technique. The test apparatus includes a cold flow acoustic test facility which is capable of simulating rocket engine combustion instabilities in a laboratory setup in which a wide range of test variables may be investigated. In the experimental setup, the rocket engine combustor is replaced by the modified impedance tube and the gas flow generated by the combustion process is simulated by a steady one-dimensional mean flow. The periodic oscillations in the unsteady rocket combustor are reproduced by means of two electropneumatic acoustic drives which generate discrete frequency pressure oscillations inside the modified impedance tube.

Test Facility Air Supply System

The air supply for the test facility is provided by high pressure storage tanks with a total volume of 500 cubic feet and a maximum operating pressure of 3,000 psig. The air supply can provide four minutes of continuous testing with the available 11-3/8 inch diameter modified impedance tube with a chamber Mach number and static pressure of 0.08 and 25 psig, respectively. A schematic diagram of the flow system is presented in Figure 2 and a sketch showing the components of

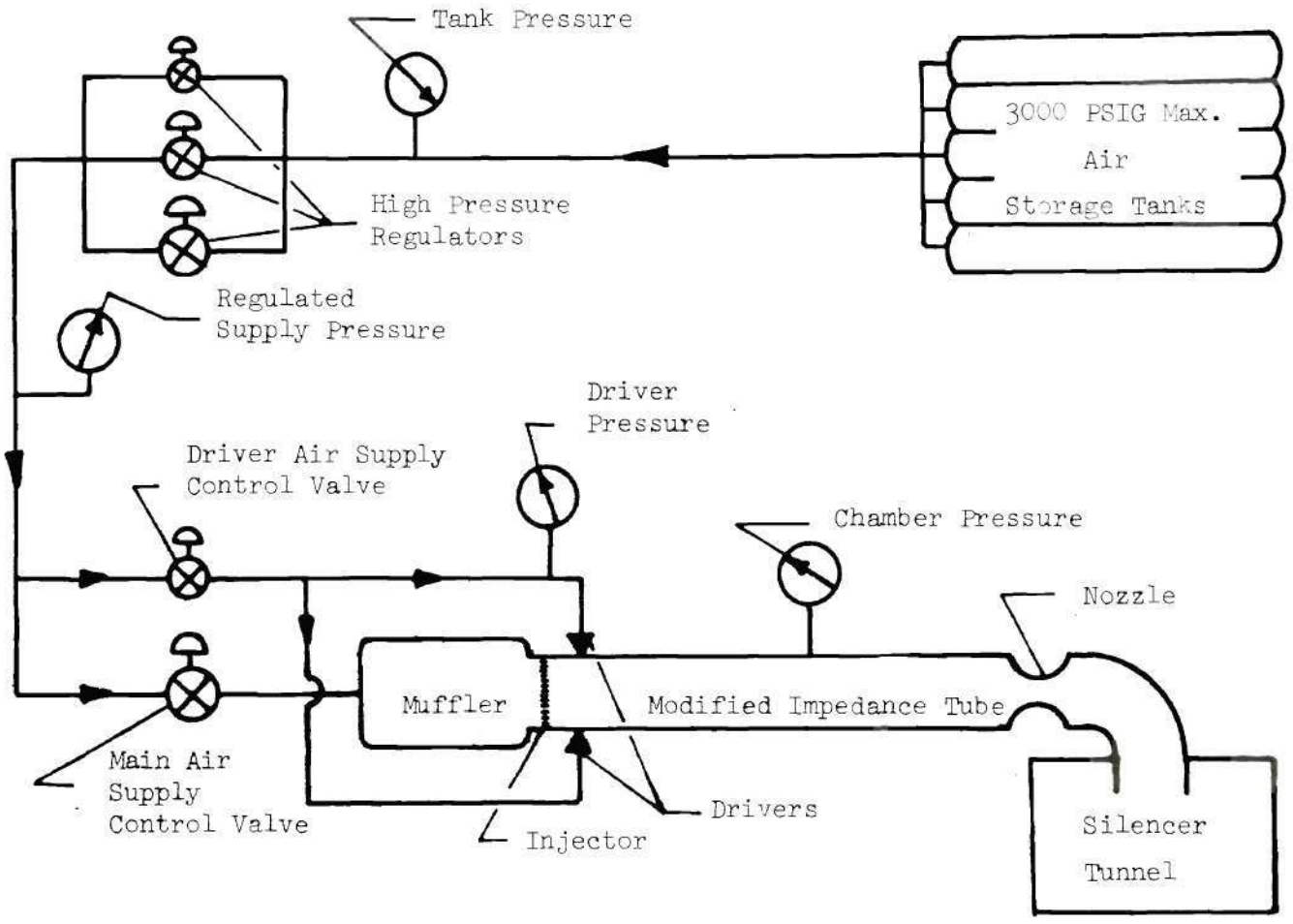

Figure 2. Schematic Diagram of the Acoustic Test Facility Flow System.

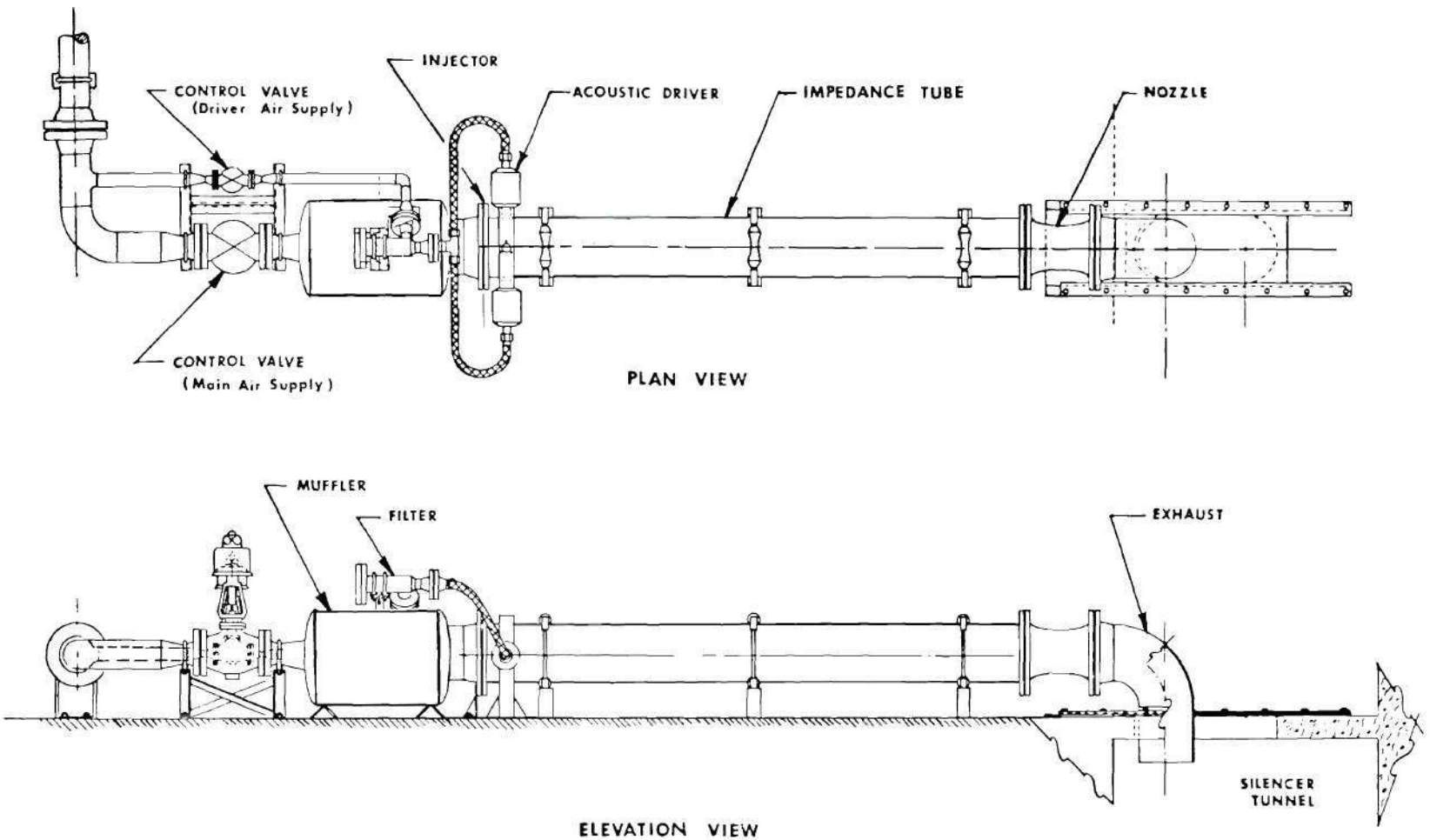

Figure 3. Acoustic Jet Facility.

the facility is presented in Figure 3.

A system of pressure regulators maintain a constant pressure air supply upstream of the main and driver air supply control valves for all impedance tube flow requirements. The main air supply control valve maintains a constant pressure differential across the acoustic drivers. The flow from the main air supply control valve is discharged into a muffler which attenuates the flow noise and provides a uniform pressure distribution across the multiple orifice injector plate located between the muffler and the impedance tube. The flow from the impedance tube, which includes both the flow from the injector and the flow from the acoustic drivers, is exhausted through the test nozzle into a silencer tunnel that is vented to the atmosphere.

Modified Impedance Tube

The modified impedance tubes used in this investigation have been specifically designed to investigate the acoustical damping capabilities of rocket engine exhaust nozzles. Two impedance tubes with inside diameters of 7-5/8 and 11-3/8 inch, respectively, have been utilized in this investigation. Each impedance tube is 120 inches in length. The upstream end of the impedance tube is attached to an injector plate and the test nozzle is coupled directly to the flange at the downstream or the exhaust end of the impedance tube. Provisions have been made along the length of each of the impedance tubes for the installation of acoustic drivers, dynamic pressure transducers, thermocouples, and static pressure orifices. The positions of the acoustic drivers and the locations of the instrumentation ports utilized for this investigation are shown in Figures 4 and 5 for the 7-5/8 inch and 11-3/8 inch

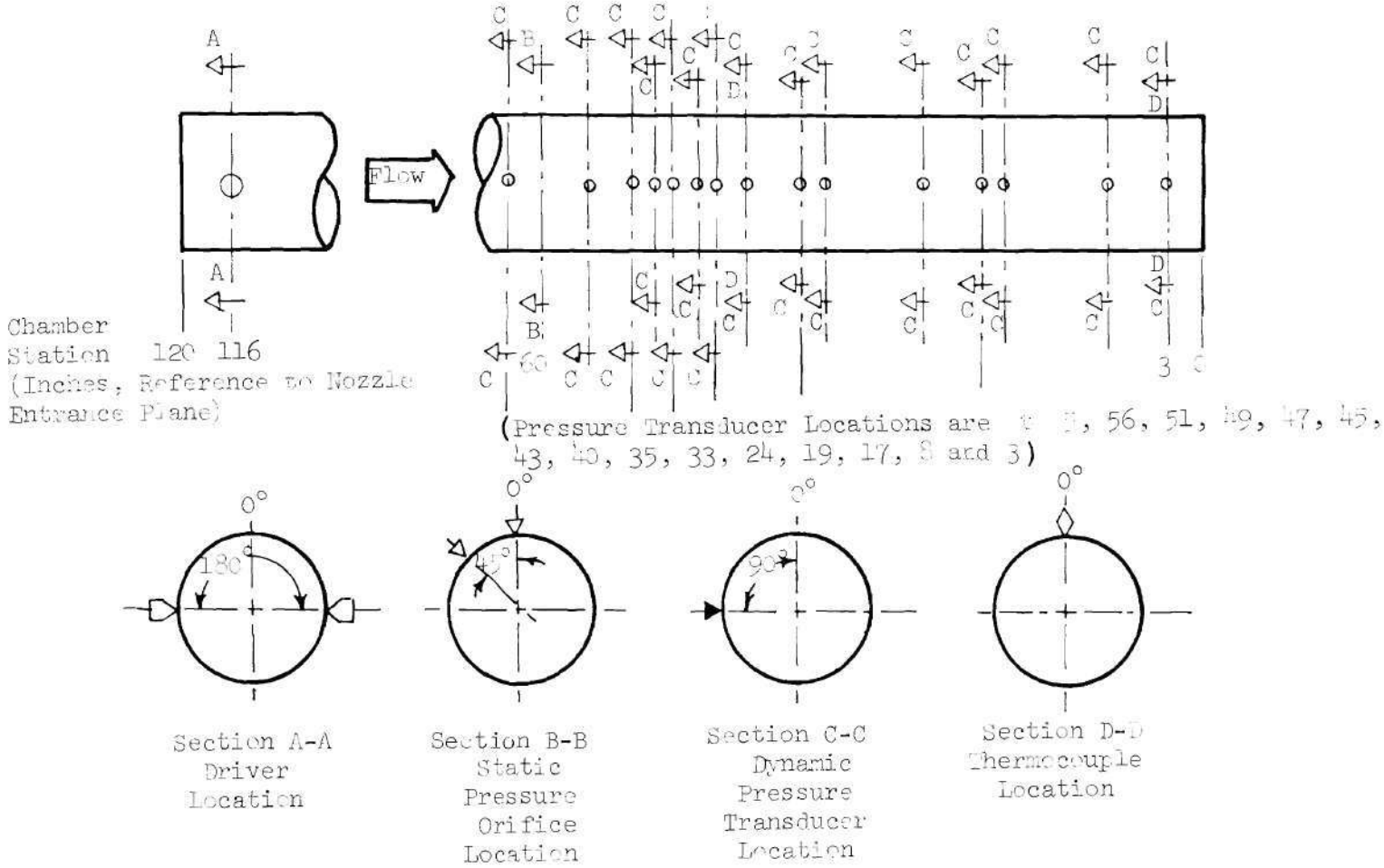

Figure 4. Driver and Instrumentation Locations, 7-5/8 Inch Impedance Tube.

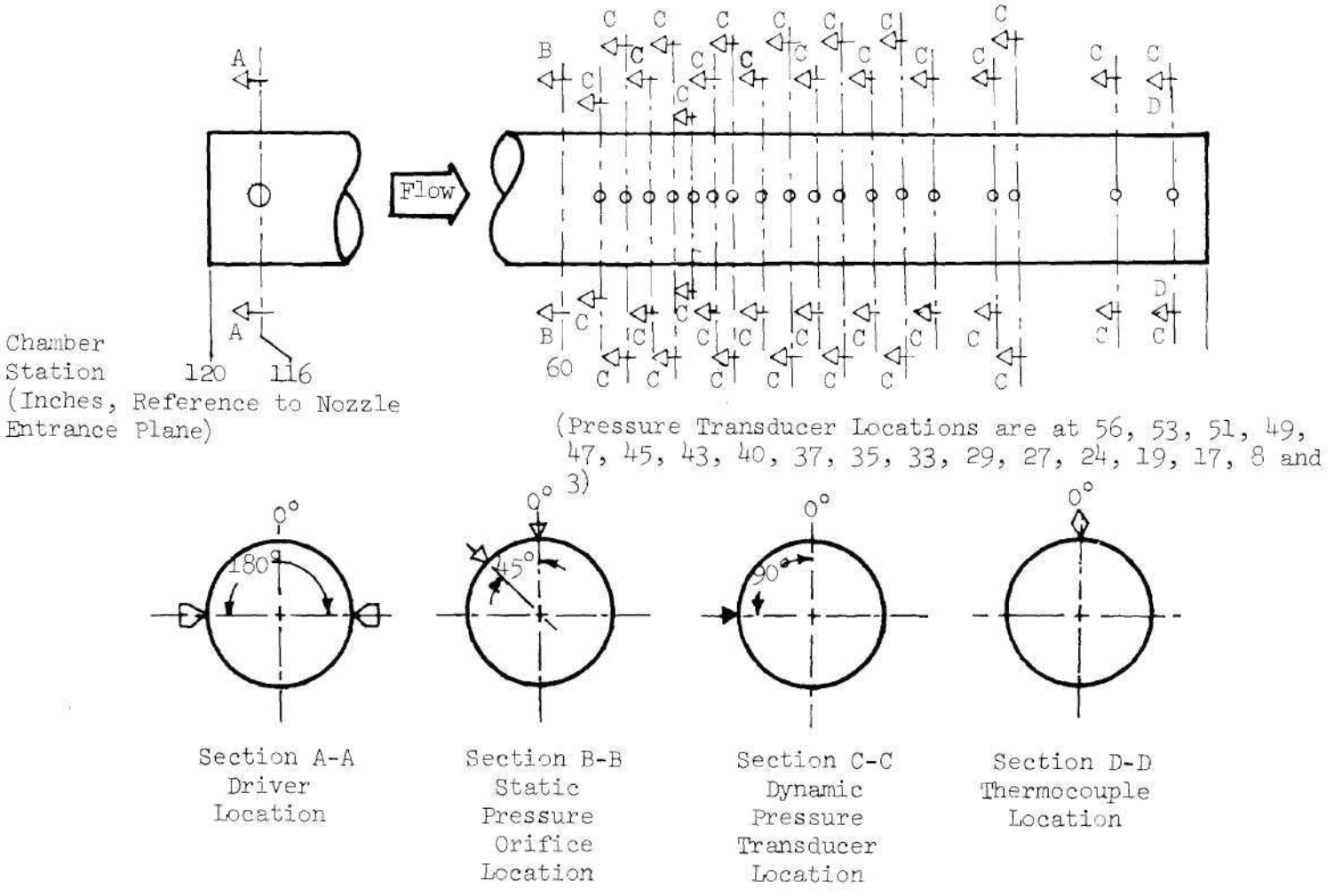

Figure 5. Driver and Instrumentation Locations, 11-3/8 Inch Diameter Impedance Tube.

diameter impedance tubes, respectively.

A multiple orifice injector is attached to the upstream end of the impedance tube to provide a uniform velocity distribution of the entering airflow. During testing a supercritical pressure difference is maintained across the injector to ensure sonic velocity at the exits of the injector orifices. This isolates the muffler from the forced pressure oscillations in the impedance tube and minimizes the acoustic feedback. Several interchangeable injector configurations, designed to provide a wide range of airflows with a relatively constant pressure difference across the injector orifices, are available for each impedance tube. In general, the injectors used in conjunction with the 7-5/8 inch and the 11-3/8 inch diameter impedance tubes have orifice patterns containing 755 and 1,627 orifices, respectively. The flow rates of the injectors are determined by the diameter of the injector orifices.

Two electropneumatic drivers, each capable of developing 4,000 watts of acoustic power, are close-coupled to the chamber wall four inches downstream of the injector. The frequency and waveform output of the acoustic drivers are controlled by a sweep oscillator. For this investigation the waveforms of the oscillations are sinusoidal and during a test, with the drivers driven in phase, the driven-wave frequencies are varied linearly over the range from 40 Hertz to 600 Hertz at a rate of 8 Hertz per second. In this frequency range the two drivers together can develop resonant sound pressure levels greater than 160 decibels (reference pressure = 2×10^{-4} microbar) in the modified impedance tube.

Test Nozzles

General Comments

The available experimental facility is restricted to testing nozzles and combustion chambers with cross section diameters no greater than 11-3/8 inch, which is the inside diameter of the larger impedance tube. Full-scale models of the RN-I and RN-II nozzles exceed the size limitations of the experimental facility. Therefore, the damping provided by the rocket nozzles has been determined by investigating the damping capabilities of geometrically similar small-scale nozzles. The required small-scale nozzles were machined from aluminum billets.

The small-scale nozzles were designed to simulate (a) the nozzle entrance plane mean flow conditions and (b) the geometry of the convergent section of the full-scale nozzles. For each small-scale nozzle configuration, the throat diameter was sized to obtain the desired mean flow Mach number in the impedance tube. All lengths were then normalized with respect to the throat radius and the axial distribution of the nondimensional cross-sectional radius was taken to be the same as in the full-scale nozzle.

The RN-I rocket engine has a single exhaust nozzle which is recessed into the combustion chamber and the solid propellant grain extends into the recessed cavity behind the plane of the nozzle entrance. A sketch showing the geometry of the submerged RN-I nozzle is presented in Figure 6.

The RN-II rocket engine has four exhaust nozzles which interface with the combustor at a conical section. The entrance planes of the nozzles are flush with the surface of the base of the conical section,

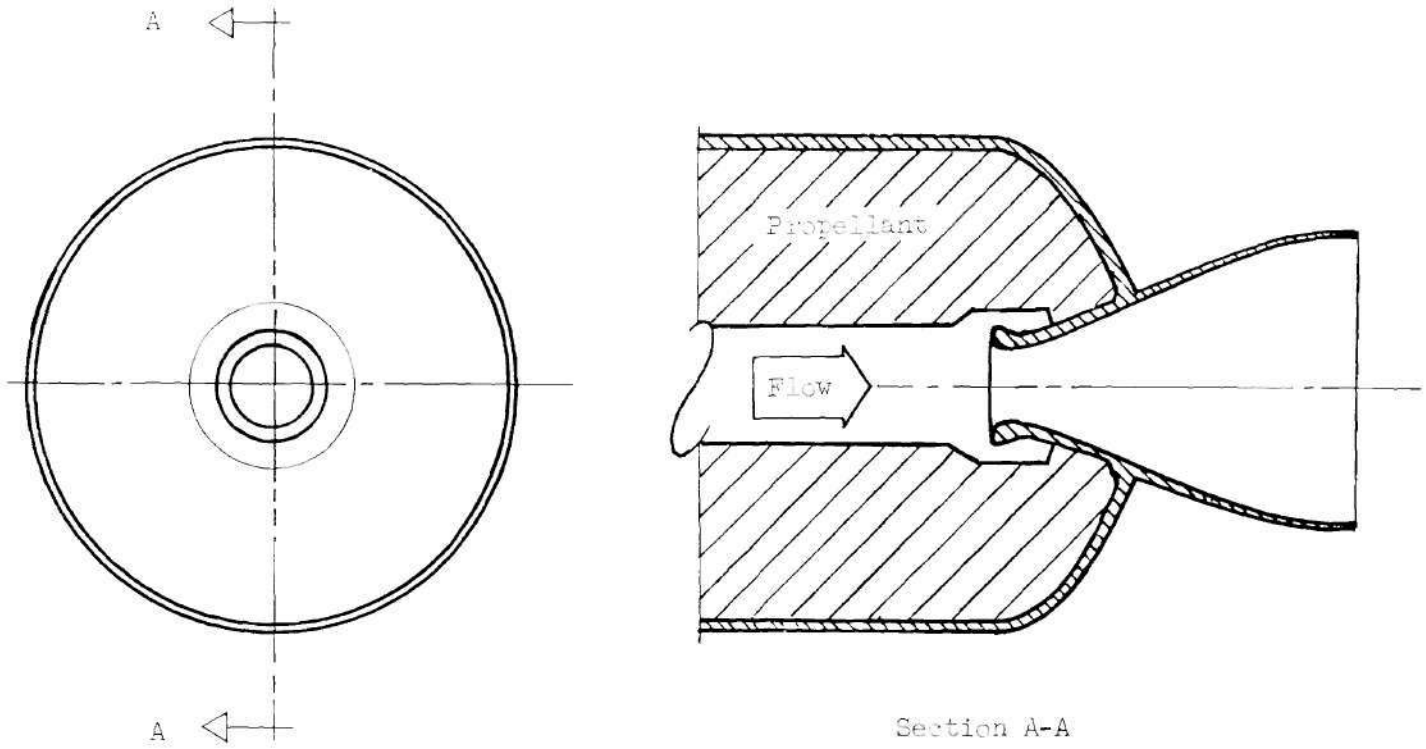

Figure 6. Single-Ported Submerged Rocket Nozzle (SN-1) Configuration.

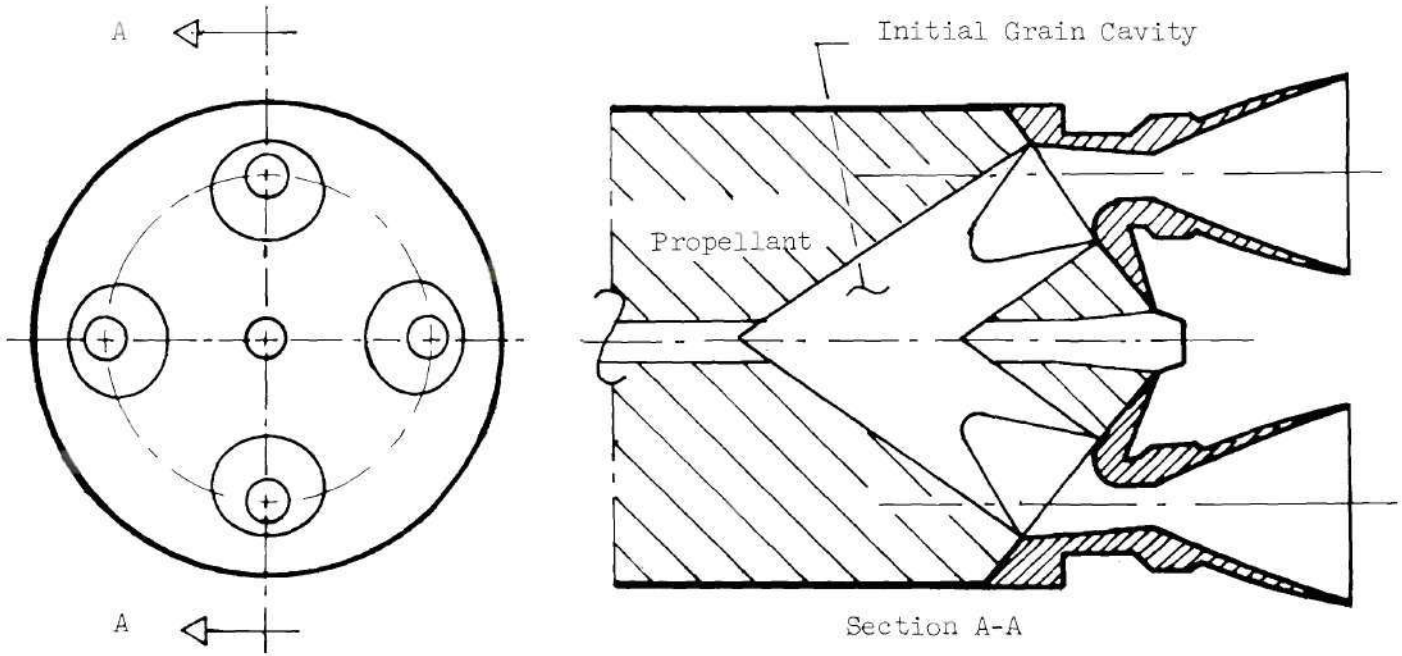

Figure 7. Multiple-Ported Rocket Nozzle (RN-II) Orientation.

and the nozzle centerlines are basically parallel to the centerline of the combustor. A sketch showing the orientation of the RN-II nozzle cluster with respect to the loaded rocket motor is presented in Figure 7.

Study 1: Damping Capabilities of the RN-I and RN-II Small-Scale Nozzles

The objective of this study is to determine the attenuation provided by small-scale models of the RN-I and RN-II nozzles. Details of the small-scale configurations of the RN-I and RN-II nozzles, scaled for testing in the 11-3/8 inch diameter impedance tube, are presented in Figures 8 and 9, respectively. The small-scale nozzle configurations represent the nozzle orientations relative to the combustors and the effective combustion chamber geometries of the rocket engines during that phase of the burn cycle when the engines experience axial instabilities.

The available longitudinal mode instability data of a rocket engine having the RN-I nozzle indicates that an instability starts at a combustor Mach number of 0.15, reaches a maximum amplitude at a combustor Mach number of 0.10, and diminishes at a combustor Mach number of 0.08. The small-scale RN-I nozzle was designed to simulate the full-scale nozzle and cavity geometries during the unstable phase of the burn cycle. Due to experimental facility size limitations the chamber mean flow Mach number for the RN-I nozzle investigation had to be restricted to 0.08, which is still within the range of unstable operation. Also, due to size limitations the chamber mean flow Mach number for the RN-II nozzle investigation had to be restricted to 0.06.

Study 2: Investigation of Acoustic Scaling Criteria

It is generally assumed that the damping capabilities of rocket

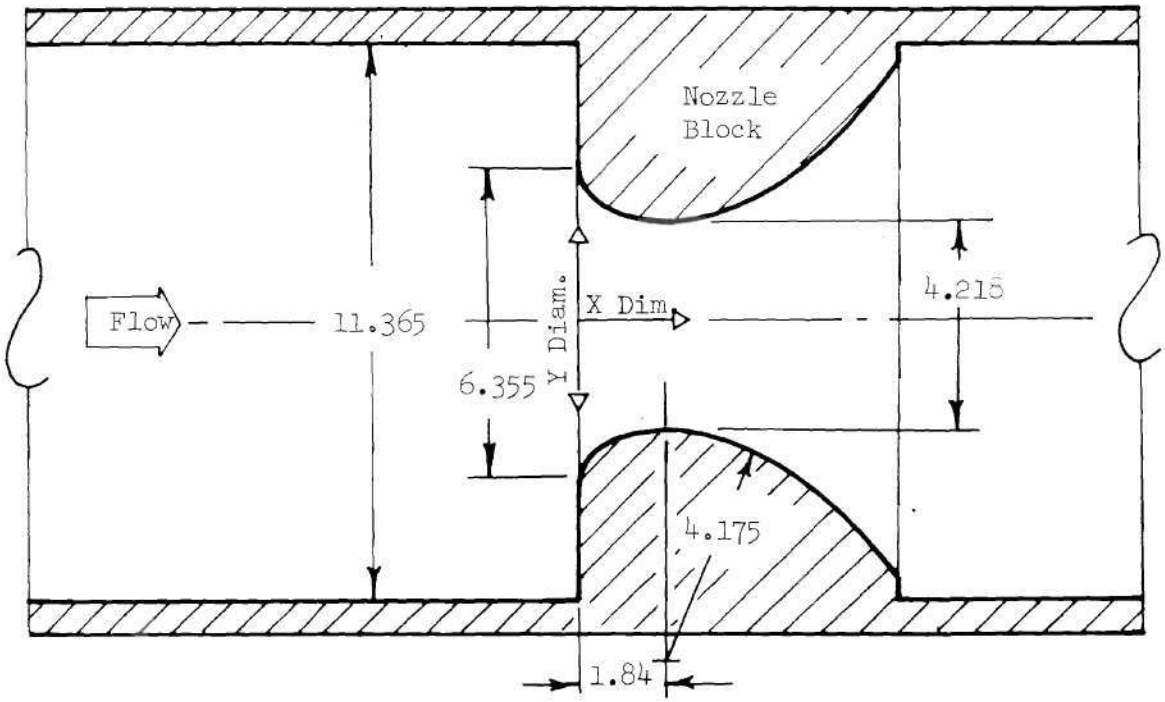

Station	0	1	2	3	4	5	6	Throat
X Dim.	0	0.077	0.153	0.307	0.537	0.843	1.166	1.840
Y Diam.	6.355	5.680	5.410	5.061	4.736	4.472	4.294	4.218

All Dimensions in Inches

Figure 8. Study 1, Small-Scale RN-I Nozzle Configuration.

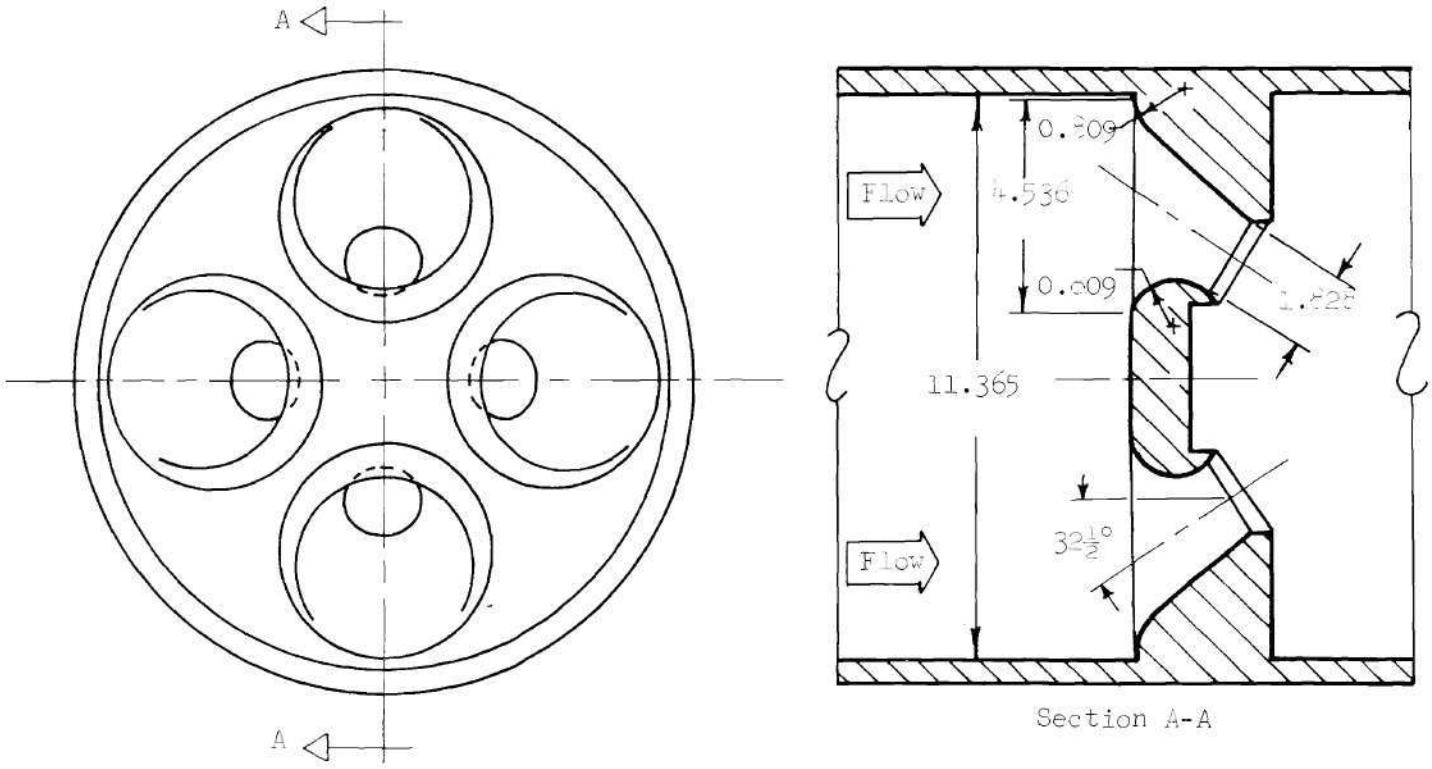

All Dimensions in Inches.

Figure 9. Study 1, Small-Scale RN-II Nozzle Configuration.

nozzles can be obtained by investigating the behavior of geometrically similar small-scale models of the full-scale nozzles. To investigate the validity of this assumption the RN-I and RN-II nozzles were scaled in this study to be compatible with the 7-5/8 inch diameter impedance tube. The small-scale configurations were scaled using the linear scaling criteria that had been used in the design of the test nozzles of Study 1. The measured admittances of the RN-I and RN-II nozzles of Study 2 were then compared with the corresponding admittances measured in Study 1.

The test configurations of the RN-I and RN-II nozzles scaled for the 7-5/8 inch diameter impedance tube are presented in Figures 10 and 11, respectively. The mean flow chamber Mach numbers for the RN-I and RN-II nozzles were 0.08 and 0.06, respectively, which were the same as the Mach numbers used in the testing of the corresponding nozzles in Study 1.

To obtain an additional check on the applicability of the scaling criteria employed in this investigation an additional rocket nozzle, having response characteristics different from those of the RN-I and RN-II nozzles, had been designed. This nozzle (henceforth referred to as RN-III) scaled for testing with the 7-5/8 inch diameter impedance tube, is presented in Figure 12. The measured admittance data of RN-III nozzle were compared with the corresponding admittance data obtained by Bell[15], who had tested a geometrically similar nozzle using the 11-3/8 inch diameter impedance tube.

Study 3: Dependence of Nozzle Damping upon Cavity Depth and Secondary Flow Rate

The RN-I rocket nozzle, shown in Figure 6, is recessed into the combustion chamber of the rocket motor. The solid propellant grain

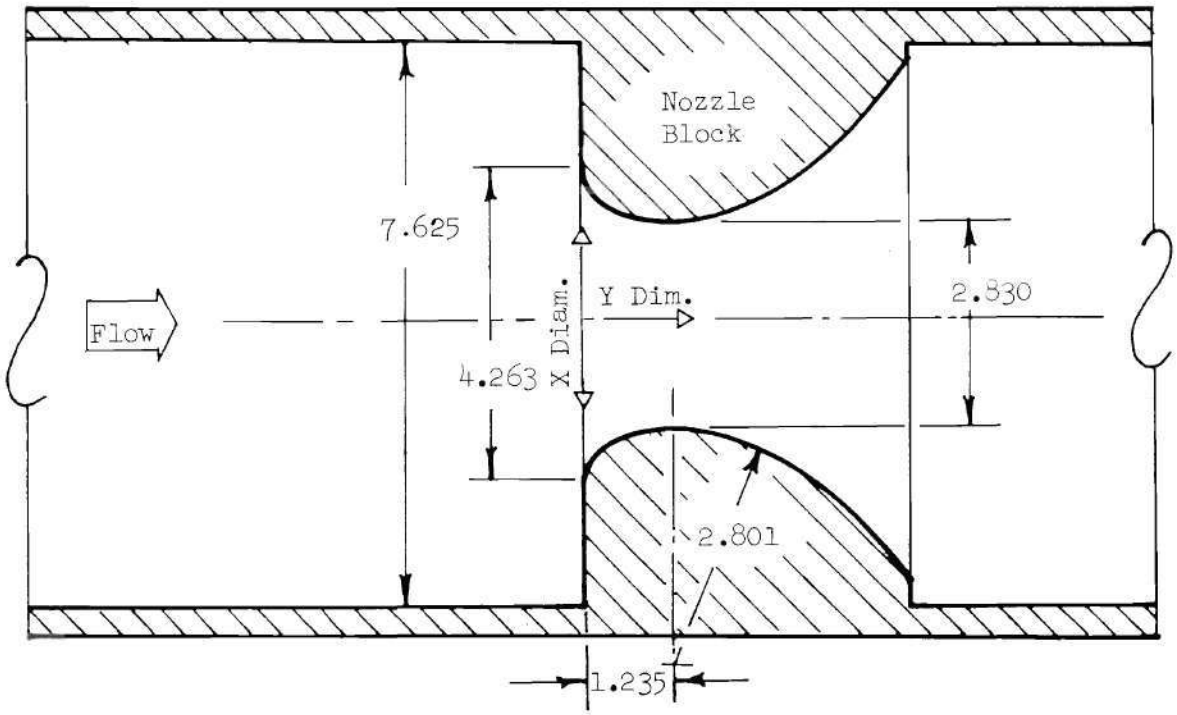

Station	0	1	2	3	4	5	6	Throat
X Dim.	0.000	0.051	0.103	0.206	0.360	0.566	0.782	1.235
Y Diam.	4.263	3.811	3.630	3.395	3.177	3.000	2.881	2.830

All Dimensions in Inches.

Figure 10. Study 2, Small-Scale RN-I Nozzle Configuration.

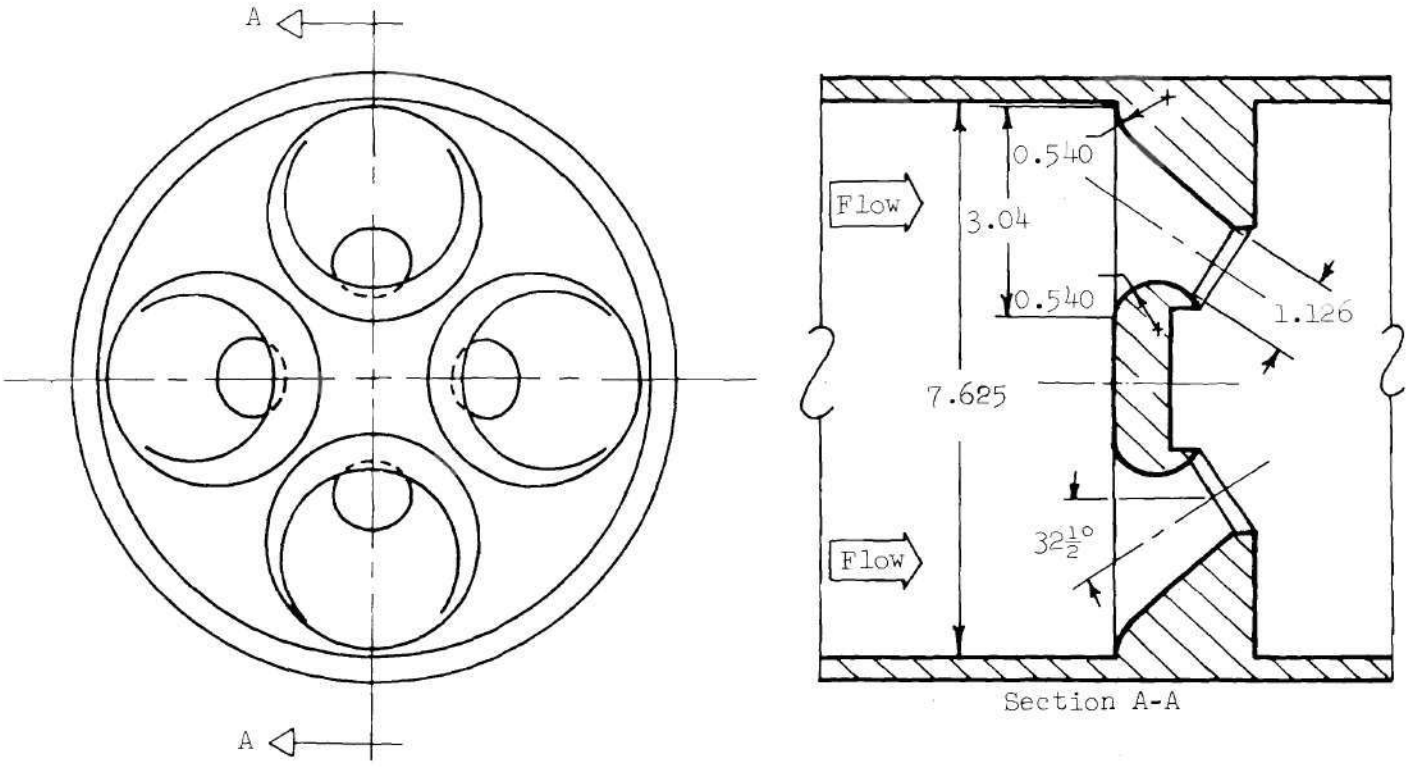

All Dimensions in Inches.

Figure 11. Study 2, Small-Scale RN-II Nozzle Configuration.

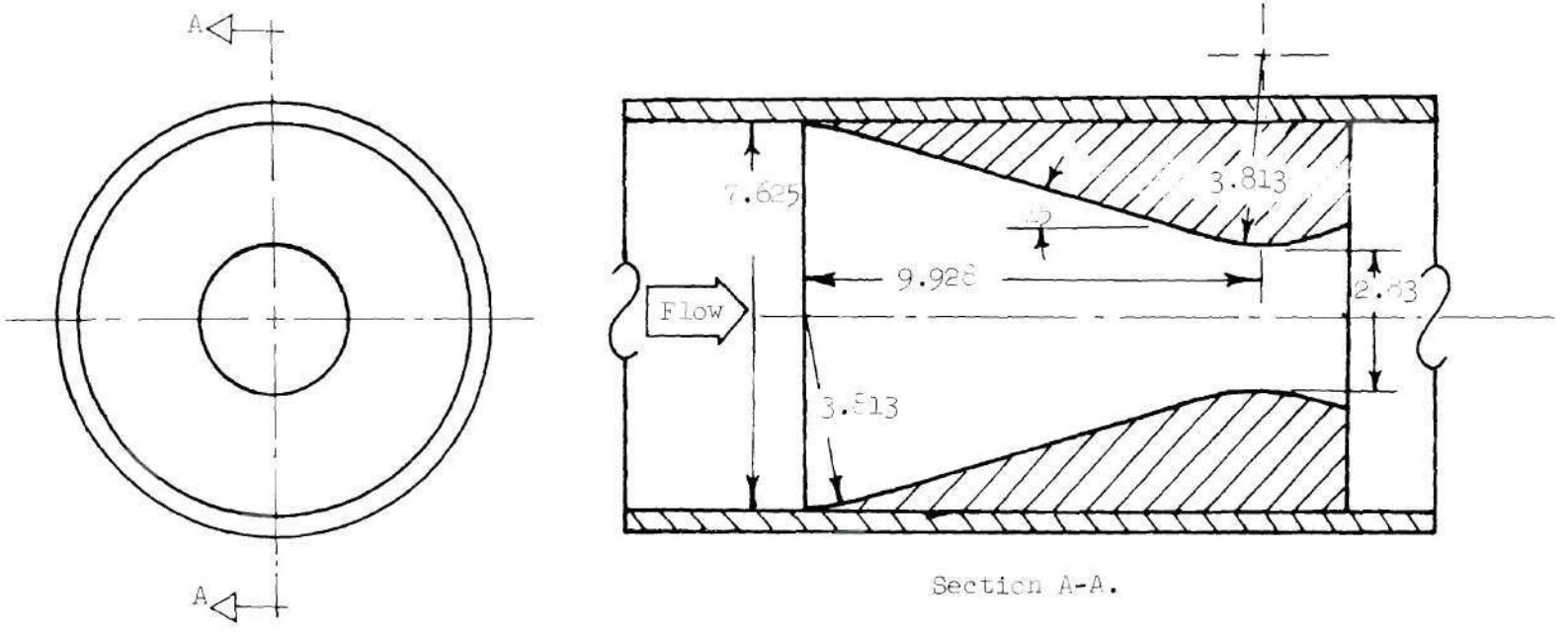

Section A-A.

All Dimensions in Inches

Figure 12. Study 2, 15° "Long" Nozzle Configuration

extends into the recessed cavity behind the nozzle entrance plane. After ignition, the recession of the burning propellant surface results in an increase with time of the depth of the cavity surrounding the nozzle, and the flow rate of the combustion products flowing from the cavity into the chamber. In this study these changes were simulated experimentally, and their effects upon the nozzle admittance were determined.

The nozzle tested in Study 3 was a small-scale version of the RN-I nozzle with provisions for varying the depth of the cavity located downstream of the nozzle entrance plane, and for injecting a secondary airflow into the chamber from the nozzle cavity. The basic RN-I, Study 3 nozzle is scaled to be compatible with the 11-3/8 inch diameter impedance tube using the same criteria as used in the design of the RN-I, Study 1, nozzle. The test nozzle of Study 3 is shown in Figure 13 with the secondary airflow injector positioned at a cavity depth of 24 inches. The location of the secondary airflow injector, which determines the cavity depth, can be varied in 8 inch increments from a position flush with the nozzle entrance plane to a position 24 inches aft of the nozzle entrance plane. This can be done by rearranging the location of the secondary airflow injector with respect to the 8 inch and 16 inch interchangeable nozzle sections.

The secondary airflow injector is a porous plate designed to provide a uniform secondary airflow into the nozzle cavity. The secondary airflow injector has a high acoustic impedance which isolates the secondary airflow plenum chamber from the pressure oscillations in the chamber and nozzle cavity. The air supply for the secondary airflow is diverted from the main air supply at the muffler and piped into the

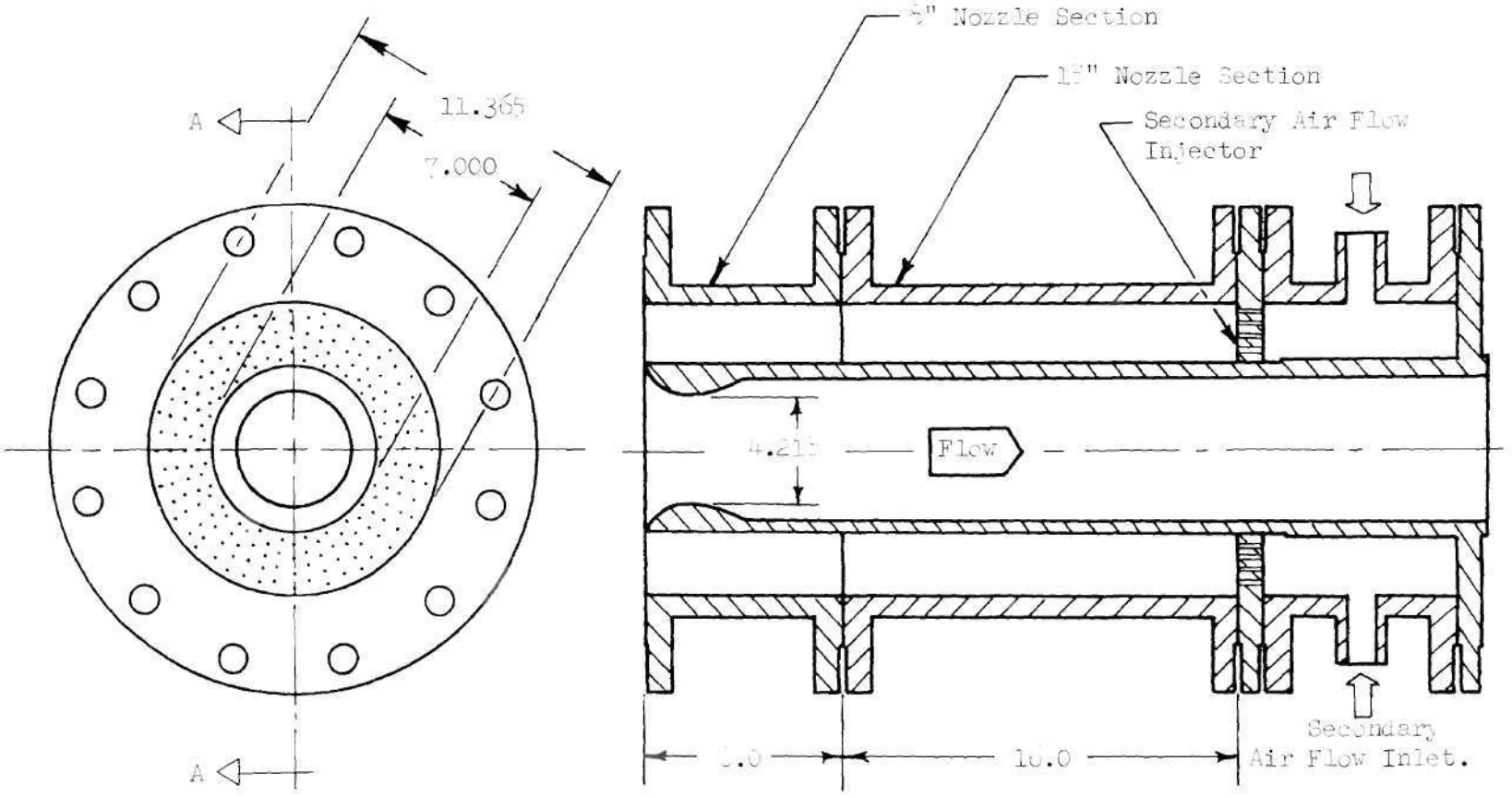

Section A-A.

All Dimensions in Inches.

Figure 13. Study 3, Submerged RN-I Nozzle Configuration.

secondary airflow plenum chamber. The stagnation pressures and temperatures in the plenum chamber and the muffler are assumed to be the same and the ratio of secondary to primary airflows is determined by the ratio of the porosities of the respective injectors.

One secondary airflow injector plate has been used for all the tests conducted in Study 3. The secondary airflow injector was initially tested at cavity depths of 0, 8, 16, and 24 inches with no orifices or zero porosity (i.e., in this case there was no secondary flow present). The orifices for the next higher secondary airflow rate (i.e., 5 percent of primary flow rate) were then machined, and the tests were repeated with cavity depths of 0, 8, 16, and 24 inches. This test sequence was repeated with secondary flow rates equal to 10, 15, 20, and 25 percent of the primary flow rate.

Study 4: Dependence of Nozzle Damping upon Convergent Section Geometry

To investigate the dependence of nozzle damping on the geometry of its convergent section, three nozzle configurations have been designed and tested. These are the conical, equal radii of curvature, and linear velocity profile nozzles shown in Figure 14. These nozzles were designed for initial testing with a nozzle throat diameter which would provide a chamber Mach number of 0.05 and they were later remachined to provide a chamber Mach number of 0.10. The nozzles of this study were tested in the 11-3/8 inch diameter impedance tube. The convergent sections of all of the configurations are of equal length.

Study 5: Damping Provided by Multiple-Nozzle Clusters

The RN-II nozzle configuration shown in Figure 7 has four nozzle ports. It was the objective of this study to investigate the effects of

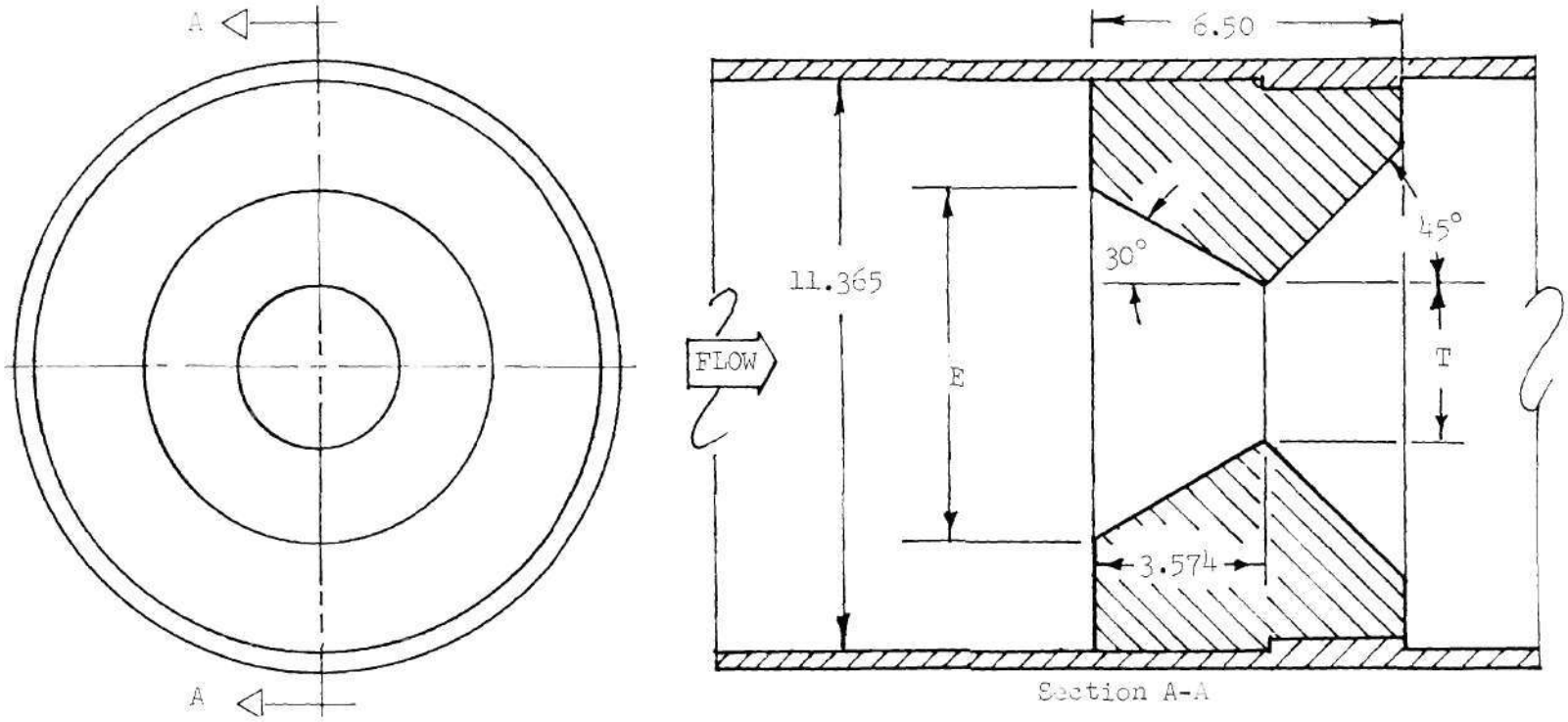

$\bar{M}$	E	T
0.05	7.464	3.338
0.10	8.836	4.710

All Dimensions in Inches.

(a) Conical Nozzle

Figure 14. Study 4, Different Convergent Section Geometry Nozzles.

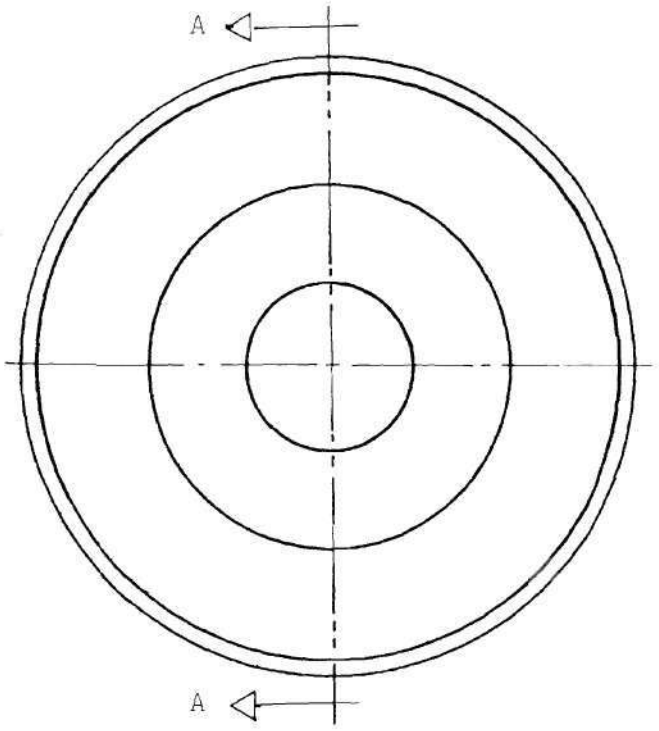

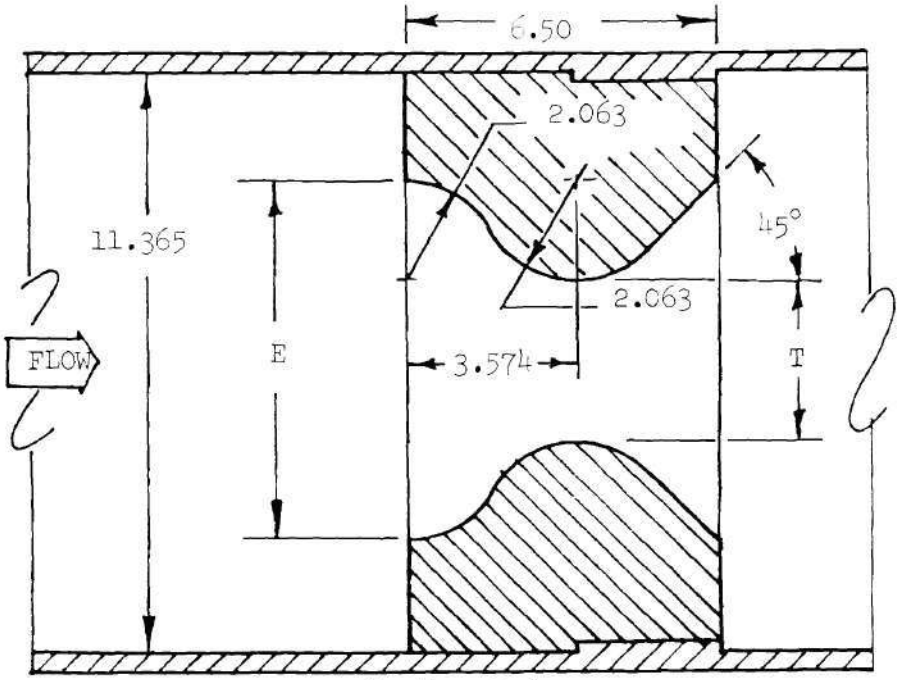

Section A-A

$\bar{M}$	E	T
0.05	7.464	3.338
0.10	8.836	4.710

All Dimensions in Inches

(b) Equal-Radii-of-Curvature Nozzle

Figure 14. Continued.

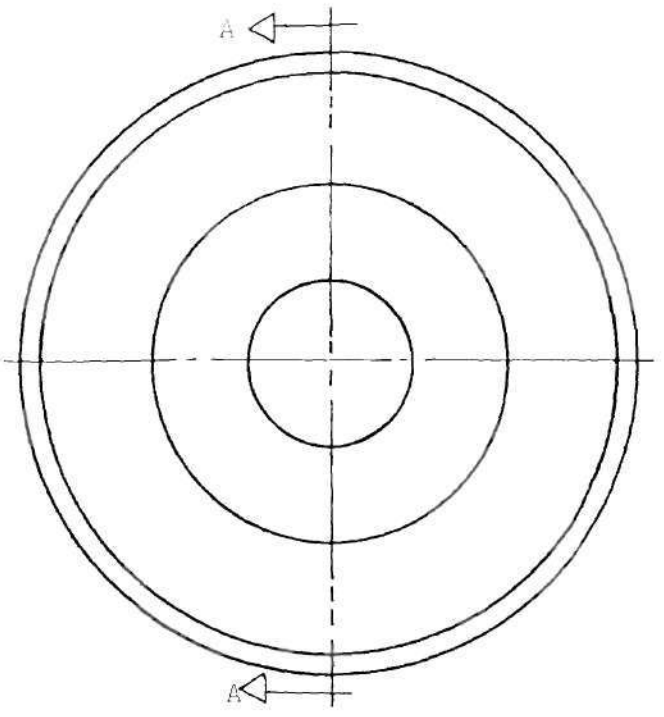

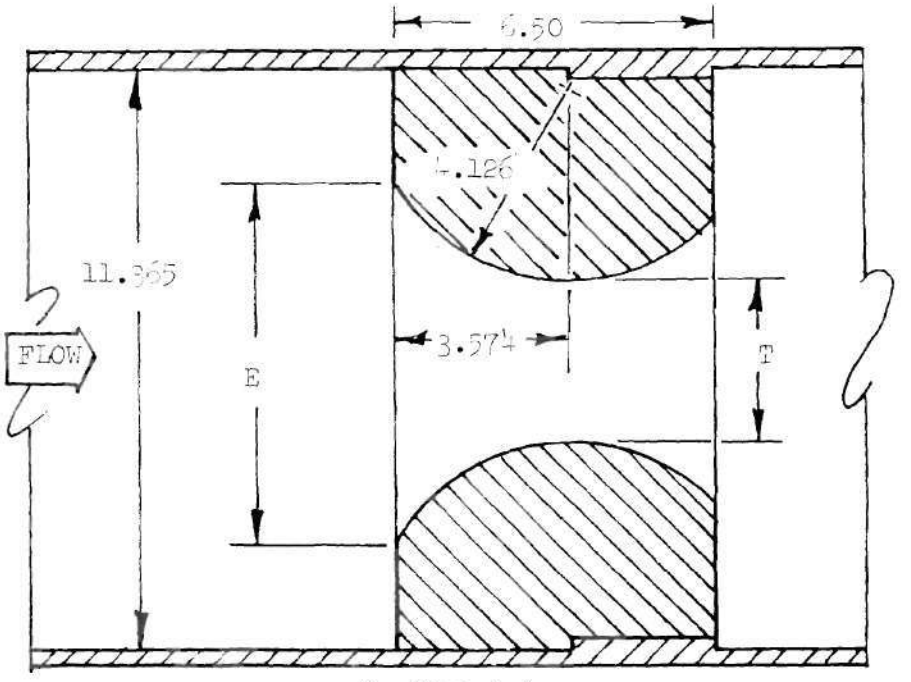

Section A-A

$\bar{M}$	E	T
0.05	7.464	3.335
0.10	8.836	4.710

(c) Linear-Velocity-Profile-Nozzle

Figure 14. Concluded.

the number of nozzles present in a multiple nozzle configuration on the damping capabilities of solid propellant rocket exhaust nozzles.

Dimensional sketches of the quadruple-, dual-, and single-nozzle configurations used in Study 5 are presented in Figure 15. These nozzles were scaled for testing in the 11-3/8 inch diameter impedance tube with a chamber Mach number of 0.06. Unlike the RN-II nozzles tested in Study 1, the Study 5 nozzles are aligned with the axis of the impedance tube. However, the basic geometric features of the nozzles tested in Study 1, such as entrance diameter, entrance lip radius, and throat diameter are duplicated in the design of the quadruple-nozzle cluster shown in Figure 15a. The dual- and single-nozzle configurations shown in Figures 15b and 15c, respectively, are designed to maintain the same total area distribution in the convergent sections as the quadruple-nozzle configuration. This ensures similar velocity distributions in the convergent sections of all the test nozzle configurations of Study 5.

Instrumentation and Data Processing

A diagram of the instrumentation system used to regulate, measure, and record the test conditions in the modified impedance tube is shown in Figure 16. The location and orientation of the instrumentation along the length of the impedance tubes are shown in Figures 4 and 5 for the 7-5/8 inch and 11-3/8 inch diameter impedance tubes, respectively.

The steady state pressure in the chamber and at the inlets to the drivers are established by monitoring two 12 inch Heise gauges and manually setting the desired pressure levels to be maintained by the respective control valves.

The two electropneumatic drivers which generate the desired pres-

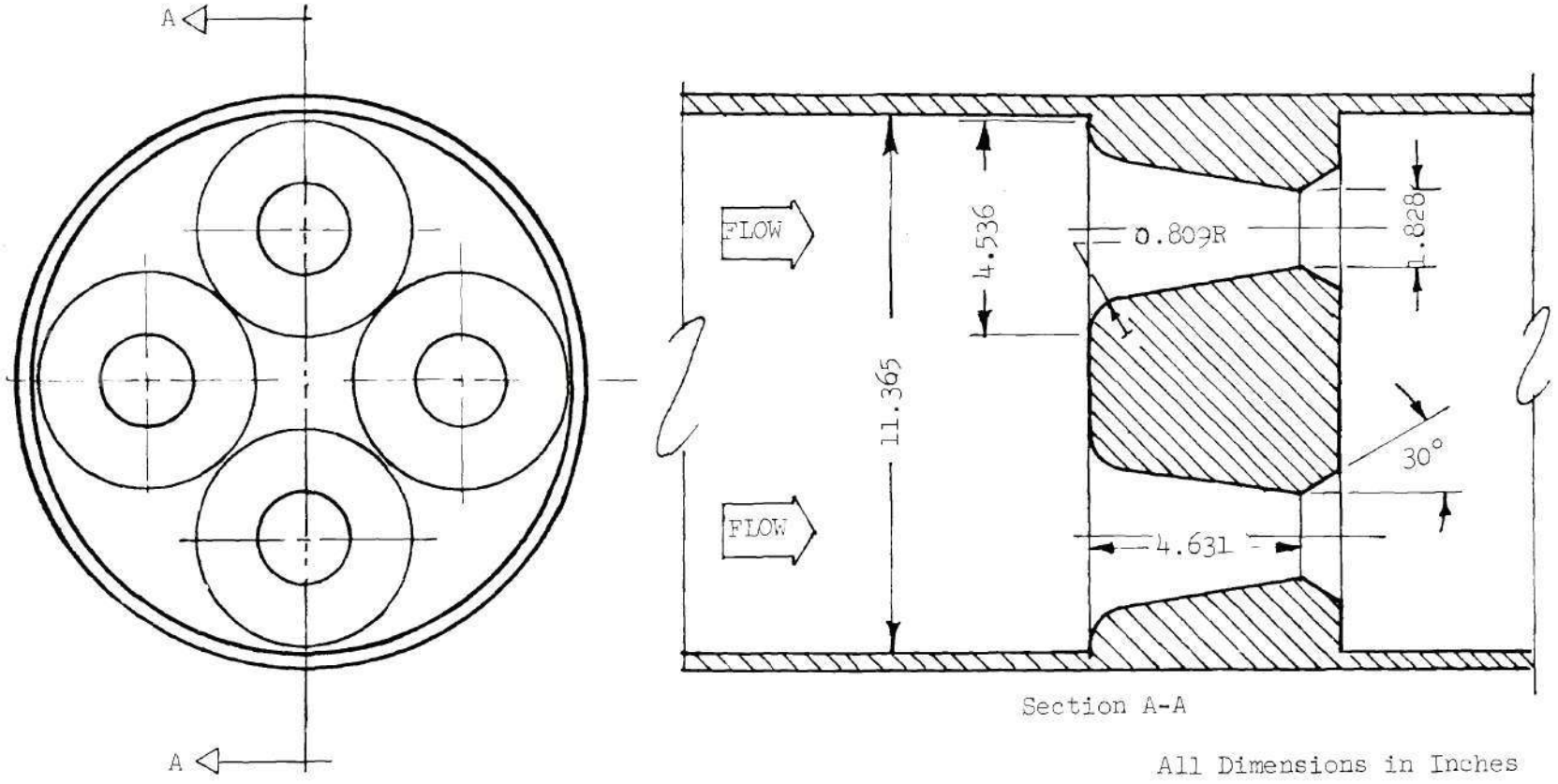

(a) Quadruple-Orifice Nozzle

Figure 15. Study 5, Multiple-Ported Nozzle Configurations.

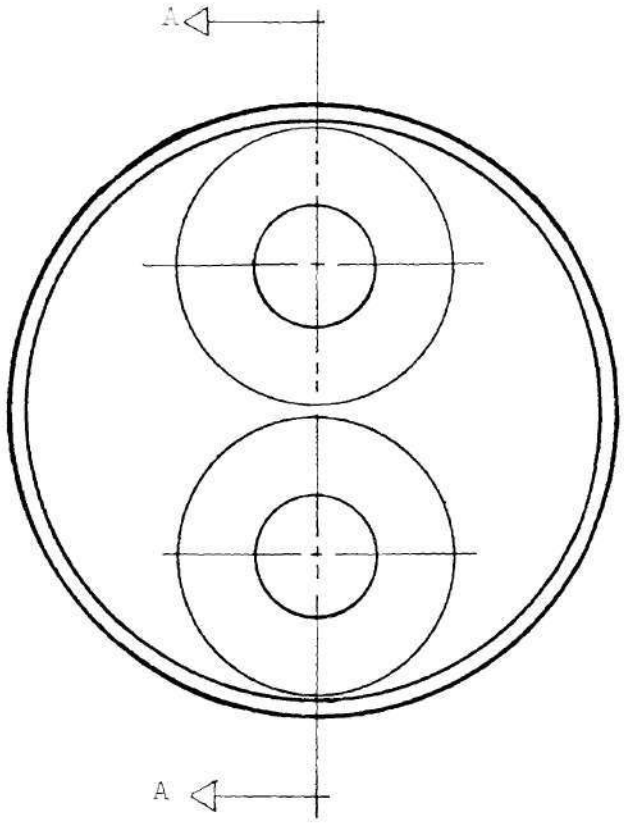

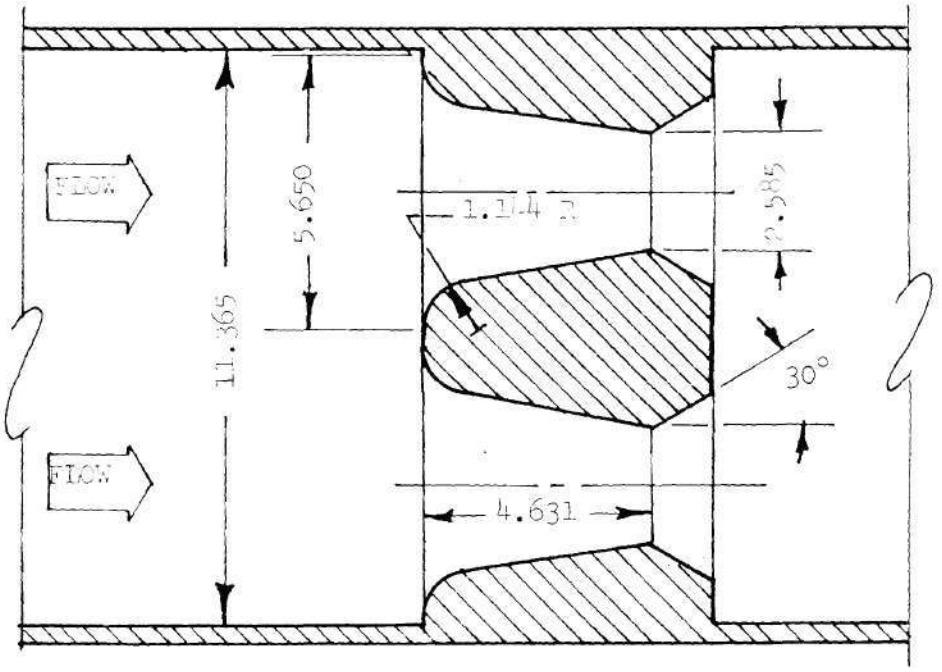

Section A-A

All Dimensions in Inches

(b) Dual-Orifice Nozzle

Figure 15. Continued.

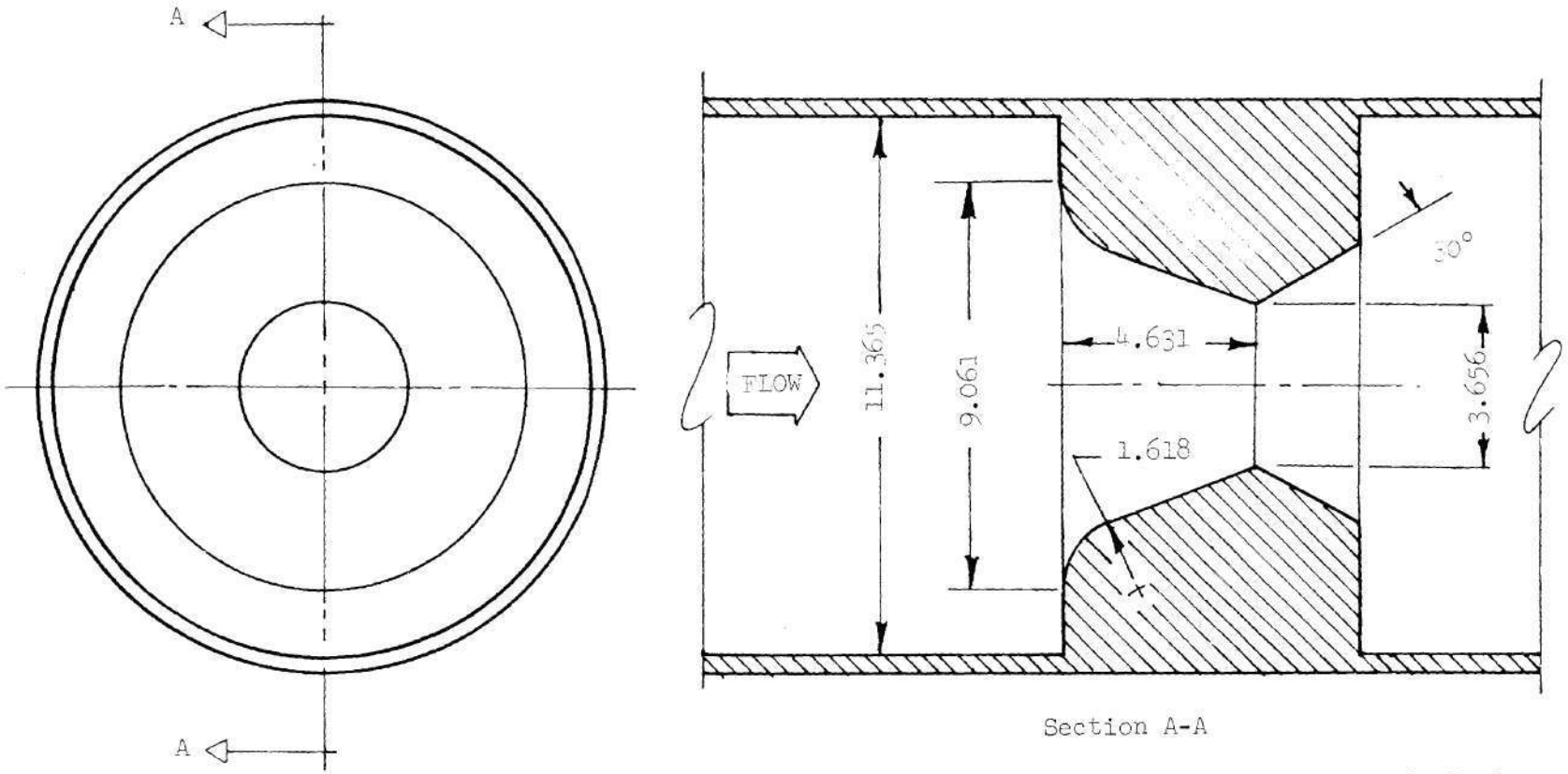

Section A-A

All Dimensions in Inches

(c) Single-Orifice Nozzle

Figure 15. Concluded.

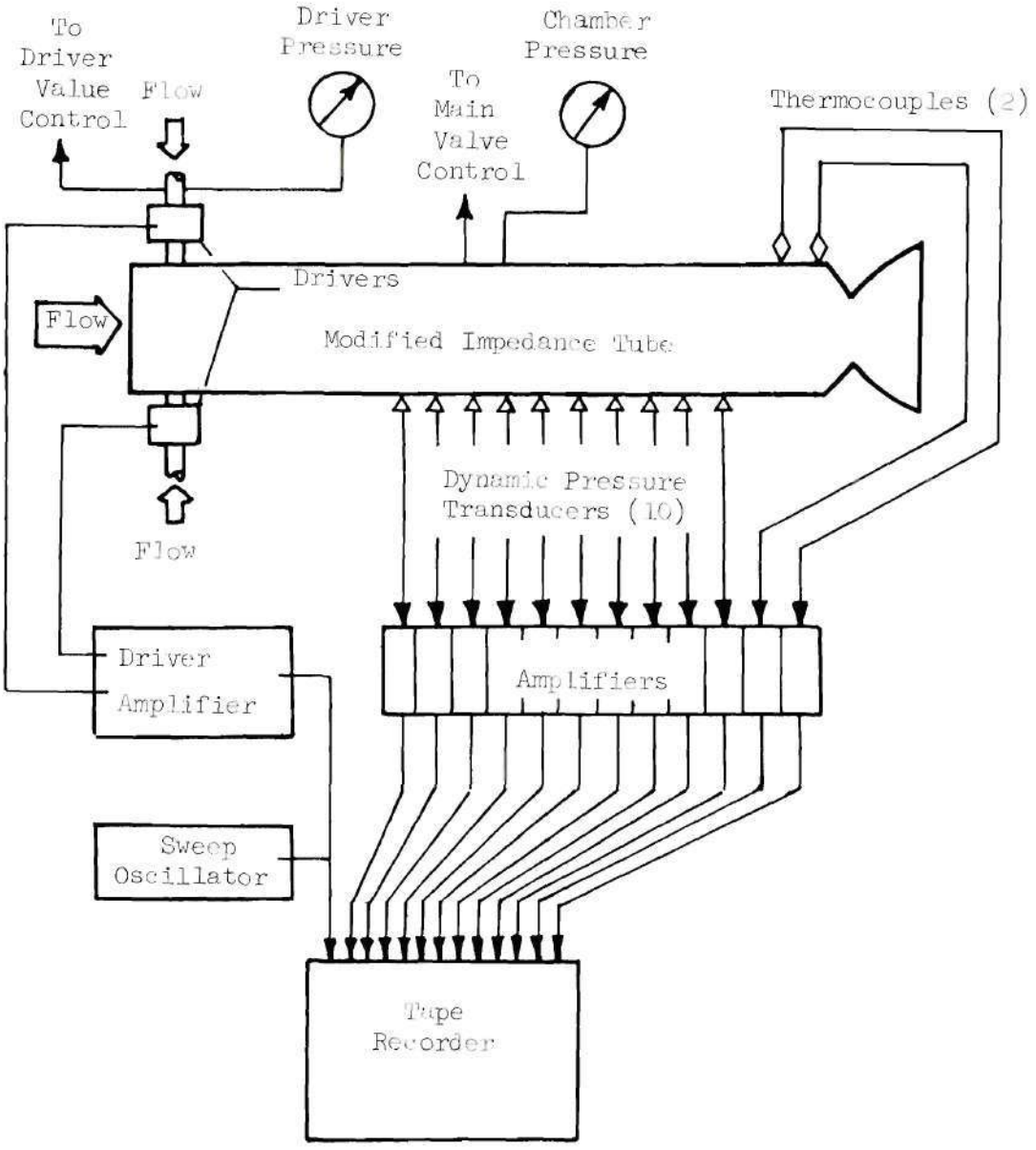

Figure 16. Instrumentation Diagram.

sure oscillations in the impedance tube are controlled by a sweep oscillator (Spectral Dynamics Model SD-104 A-5). The pressure oscillations in the impedance tube are measured by ten pressure transducers (Photocon Model 403). The air temperature in the impedance tube is measured by two copper-constantan thermocouples. The dynamic pressure signals from the transducers and the outputs from the thermocouples are amplified and recorded on a tape recorder (Ampex Model FR-1300). The transducers have a dynamic range from 110 decibels to approximately 180 decibels and exhibit a flat frequency response over the range from 10 Hertz to 3,000 Hertz. In addition to the output from the transducers and thermocouples, the signal from the sweep oscillator to the acoustic drivers is also recorded during the tests to be used as a reference frequency for data reduction.

The analog data recorded on the tape recorder during each test are digitized by a 14-channel analog-to-digital conversion system (Radiation Corporation). The digitized data are processed on a computer (Univac 1108) using a special computer program which uses a Fourier Analysis to compute the amplitudes and phases of the chamber pressure oscillations as a function of the driver input frequency. This program also computes the chamber air temperature data. Detailed description of the associated computer program is presented in Reference 24. The resulting pressure amplitudes and phases along with the temperature data are then used to determine the admittance parameters α and β and the real and imaginary parts of the nondimensional admittance y_N of the test nozzle.

Test Procedures

Before each test, the components of each dynamic pressure data

channel are calibrated by recording a known sinusoidal pressure signal from an acoustic calibrator (Whittaker Corporation Model PC-125) on the respective data channels of the analog tape recorder. This signal is used during data reduction as a reference pressure for the calibration of the pressure transducer, amplifier, and tape recorder channel which make up the data channel. The thermocouples measuring the impedance tube air temperature are calibrated by recording reference voltage outputs on the corresponding data channels of the tape recorder.

At the beginning of a test, the high pressure regulator valves are set to maintain 300 psig pressure upstream of the main and driver control valves. The sweep generator, which controls the driver output waveform and frequency, is set to generate a sinusoidal signal at the low frequency limit of the frequency range. The driver flow control valve is then set to maintain 40 psi pressure differential across the drivers. Finally, the main flow control valve is set to automatically maintain a pressure level of 20 psig in the impedance tube throughout the test.

After test conditions are established in the impedance tube, the recording of pressure and temperature data is initiated simultaneously with the start of the frequency sweep. The sweep oscillator maintains an 8 Hertz per second rate of change of the driver frequency from the initiation of the sweep until the upper limit of the test frequency range is reached. The test is concluded when the upper limit of the frequency sweep is reached.

CHAPTER IV

RESULTS AND DISCUSSION

Introduction

This section will describe and discuss the results that have been obtained in this investigation. The results reported in this section were obtained by investigating the acoustic responses of geometrically similar small-scale nozzles, under cold flow conditions, over a range of frequencies whose wavelengths are equal to the wavelengths observed during axial instabilities inside typical rocket engines.

Available test data[2,3] indicate that rocket engines with nozzles similar to RN-I and RN-II experience axial instabilities in the range of frequencies between 120 Hertz to 1200 Hertz. Substituting this information together with appropriate temperature data into Equation (2-37) leads to the conclusion that testing the small-scale nozzles over a range of frequencies between 40 Hertz and 600 Hertz will ensure that conditions during axial instabilities in the actual engines are duplicated in cold flow experiments. All the cold flow nozzle admittance data presented in this thesis were obtained in the above-mentioned frequency range.

To establish the applicability of the chosen experimental techniques and to assure the repeatability of the experimental data, each of the data reduction schemes discussed in Chapter II was checked by measuring the frequency dependence of the nozzle admittance on two different occasions. The results obtained in these tests are presented in

Figures 17 and 18. The data presented in Figure 17 were obtained by measuring the standing wave pressure amplitudes along the modified impedance tube while the data shown in Figure 18 were obtained from pressure phase measurements along the length of the modified impedance tube. The mean square deviation between the two tests in the values of the admittance parameter α obtained by pressure amplitude measurements is 0.007 and between those obtained by pressure phase measurements is 0.0046. In Figure 19, the admittance parameter α obtained from pressure amplitude measurements is compared with corresponding data obtained from pressure phase measurements. An examination of these figures indicates that both measurement techniques yield comparable data. However, these figures also illustrate that the admittance parameter α obtained from pressure amplitude measurements has more scatter than the corresponding data obtained from phase measurements. On the other hand, a similar series of tests have established that pressure amplitude measurements yield better data as far as the phase parameter β is concerned. Hence, unless otherwise stated, the admittance data presented in this thesis will be based upon values of α obtained from pressure phase measurements and values of β obtained from pressure amplitude measurements.

Study 1: RN-I and RN-II Small-Scale Nozzle Admittance Data

To approximate the flow conditions during axial instabilities in rocket engines, the small-scale model of the RN-I nozzle was tested with a chamber Mach number of 0.08 and the small-scale model of the RN-II nozzle was tested with a chamber Mach number of 0.06 using the 11-3/8 inch impedance tube. These experiments were conducted over the above-

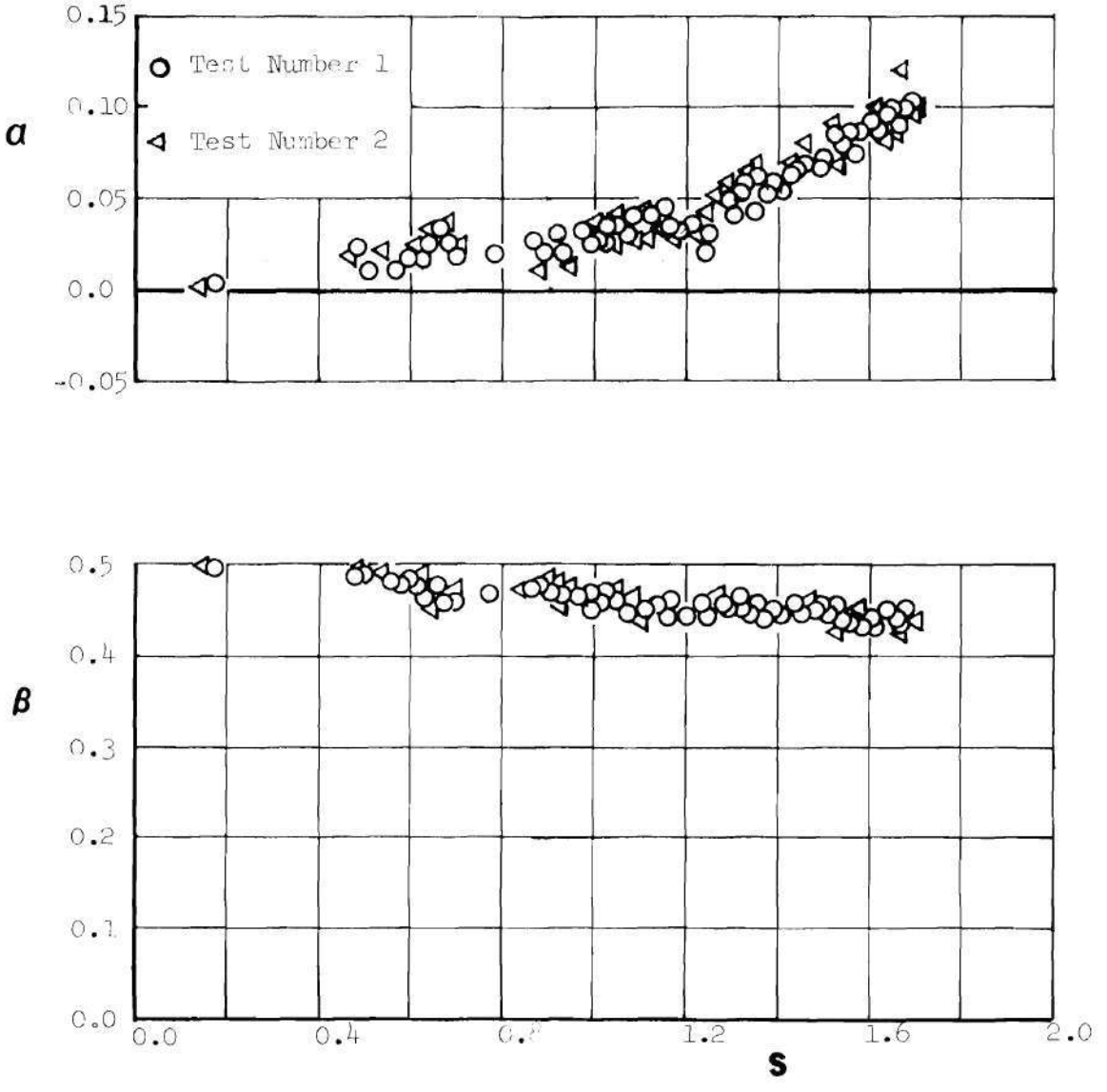

Figure 17. Repeatability of The Admittance Data Obtained From Pressure Amplitude Measurements.

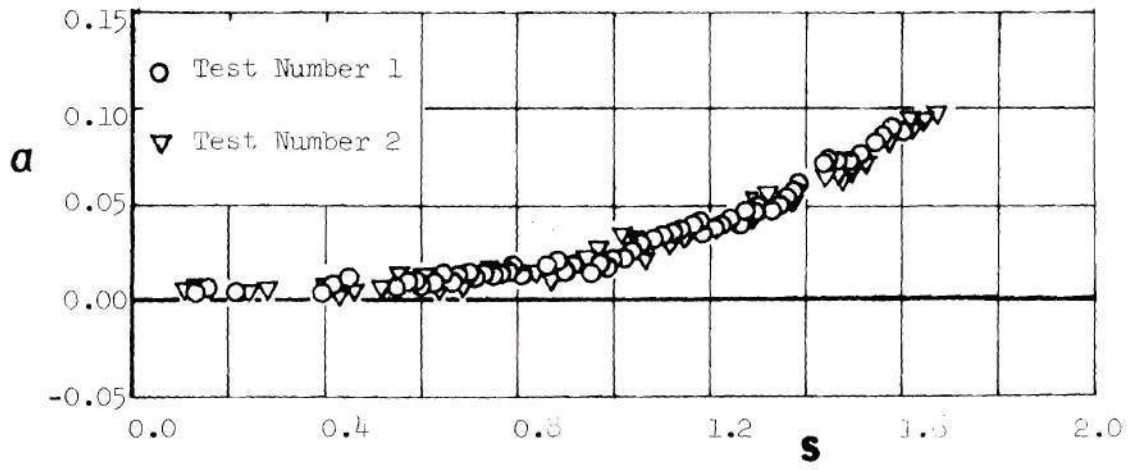

Figure 18. Repeatability of Admittance Parameter α Obtained From Pressure Phase Measurements.

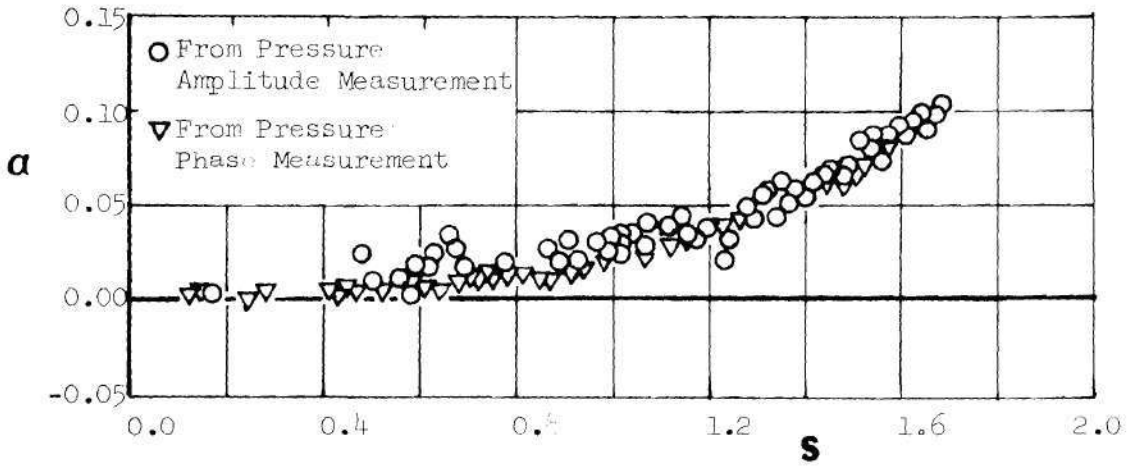

Figure 19. Comparison of Admittance Parameter α Obtained From Pressure Amplitude and Phase Measurements.

mentioned frequency range in which the tested RN-I and RN-II nozzles satisfy the "short nozzle" approximation (i.e., $L_N/\lambda \ll 1$).

The RN-I and RN-II nozzle admittance data, measured in Study 1, are presented in Figures 20 and 21, respectively, as a function of the nondimensional frequency S, where

$$S = \frac{2\pi f r_c}{\bar{c}} \qquad (4\text{-}1)$$

The figures pertaining to each of the nozzles include the measured values of the admittance parameters α and β as well as values of the real and imaginary parts of the nondimensional nozzle admittance y_N.

Examination of the measured data indicates that both nozzles exhibit similar damping characteristics over the frequency range of this investigation. Figures 20 and 21 show that for both nozzles, the values of the admittance parameter α, that describes the amplitude attenuation provided by the nozzles, are very small and practically independent of frequency. The same figures show that the measured values of the admittance parameter β, that describes the phase shift between the incident and reflected pressure waves at the nozzle entrance, are also practically independent of frequency and their magnitudes are close to $\pm$ 0.50. However, a closer examination of the measured values of β indicates that the RN-II nozzle causes a larger phase shift, between the incident and reflected pressure waves, than the RN-I nozzle. This effect is probably caused by the more complex geometry of each of the nozzles that form the cluster of the RN-II nozzles as well as the non-uniformities of the flow field upstream of the nozzle entrance. This larger phase shift indicates

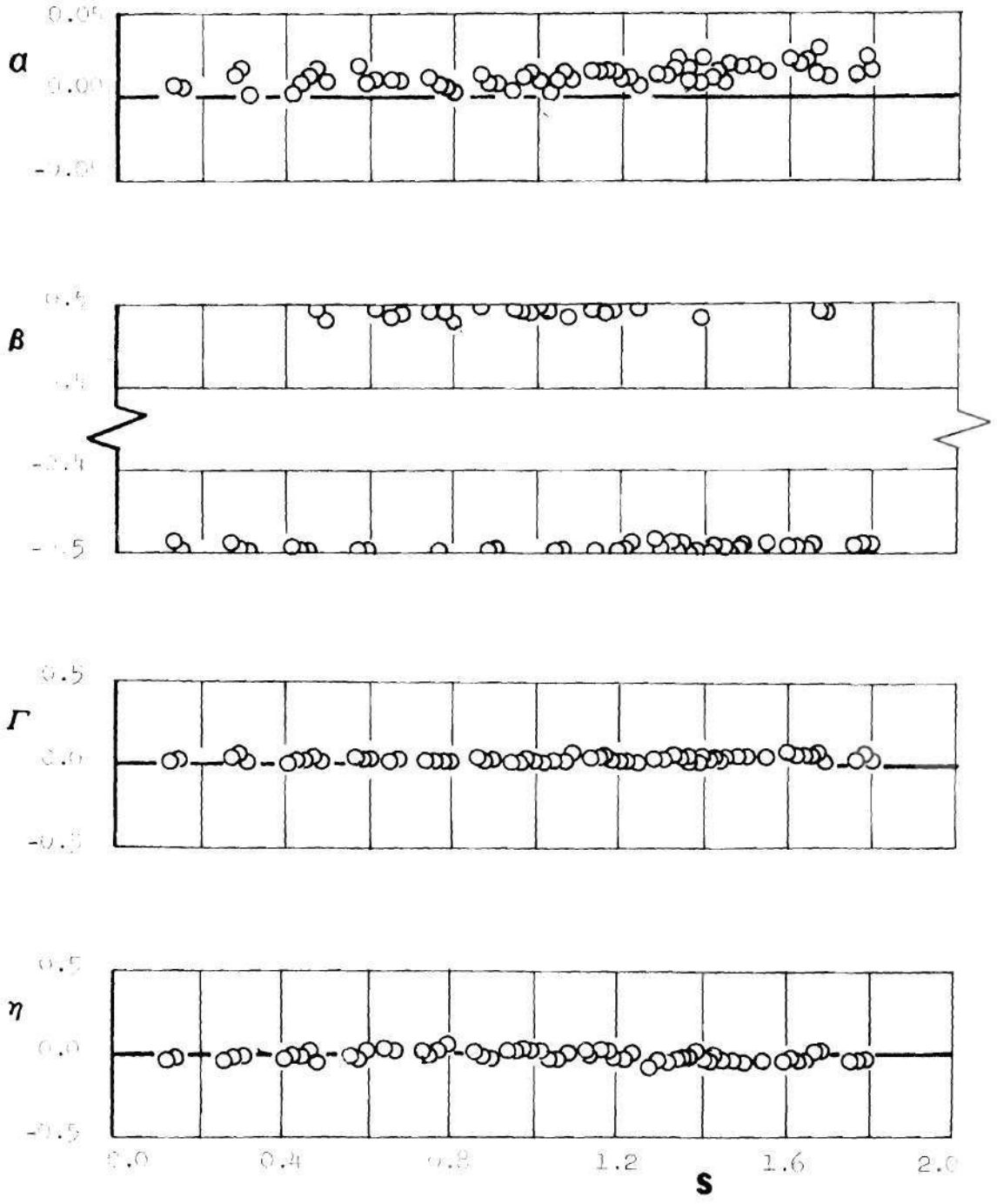

Figure 20. Study 1, Admittance Data of the Small-Scale Fin-1 Nozzle.

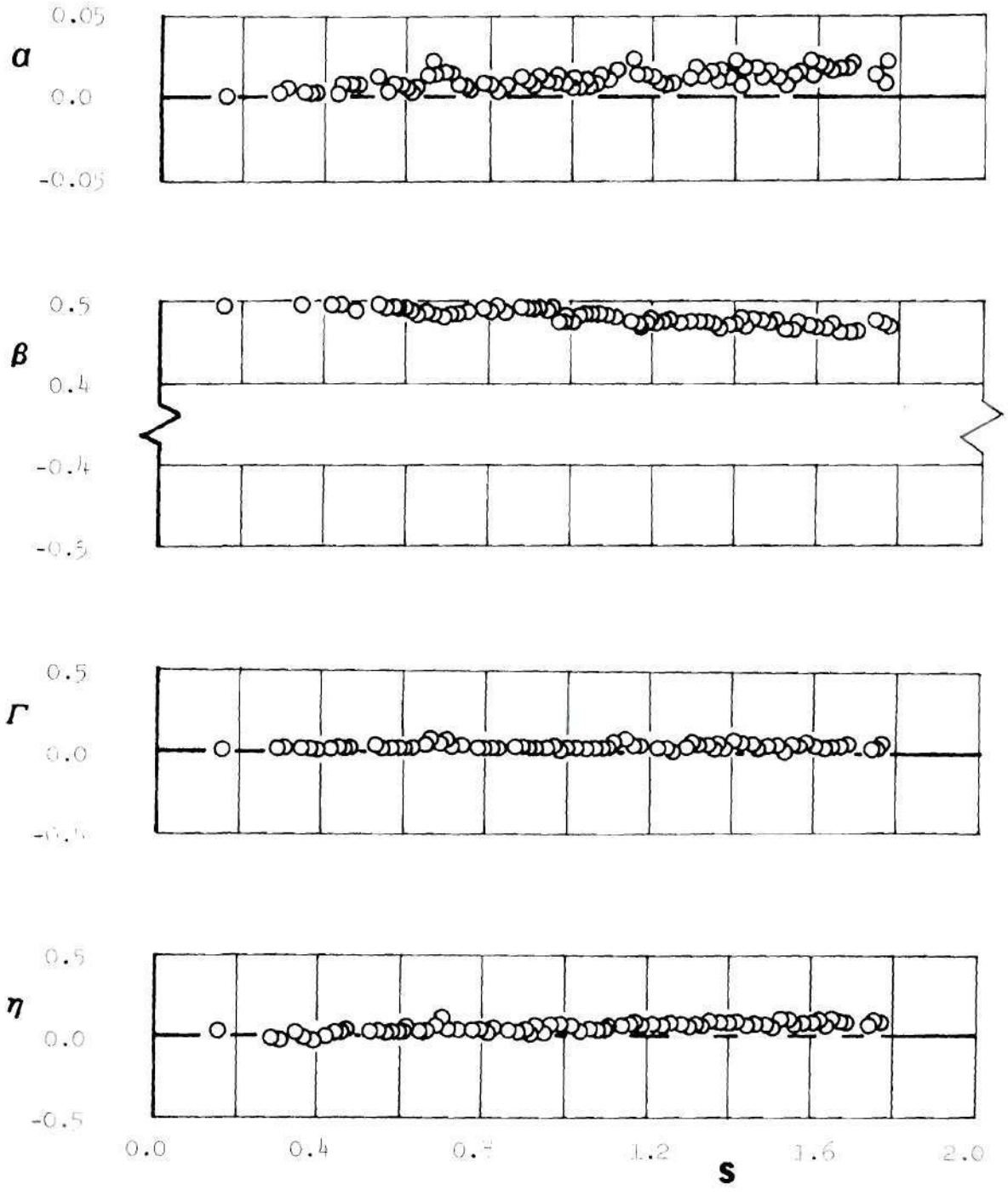

Figure 21. Admittance Data of the Small-Scale RN-II Nozzle

that the RN-II nozzle configuration "appears" to the oscillations in the chamber as being "longer" than the RN-I nozzle.

It should be pointed out that if the nozzle entrance plane was replaced by a solid wall then the resulting values of α and β would be 0.0 and 0.5, respectively. The closeness of the measured values of α and β, for both nozzles, to 0.0 and 0.5 suggests that the admittances of each of these nozzles is close to that of a solid wall. The measured low values of α indicate that an incident pressure wave loses little energy when it impinges upon the nozzle entrance plane and the closeness of the measured values of β to 0.5 implies that an incident pressure wave almost reflects instantaneously at the nozzle entrance plane. It is interesting to note that in the case when there is no mean flow in the impedance tube and when the nozzle is replaced by a solid wall, the velocity and pressure oscillations are 90^{o} out of phase and as a result there is no mean acoustic energy radiation through the chamber or through the solid boundary. The data measured in the present series of experiments show that the solid wall boundary condition is only slightly modified when models of the nozzles tested in this study are present at the end of a rocket chamber. This observation suggests that the condition of no acoustic energy radiation, that holds for the rigid wall boundary condition, is only slightly modified when these nozzles are present in a system. The closeness of the measured nozzle admittances to the solid wall admittance suggests that the RN-I and RN-II nozzles remove little acoustic energy from the chamber and thus provide little damping for axial instabilities.

The measured values of α and β were substituted into Equations

(2-10) and (2-11) and the resulting values of the admittances, for both the RN-I and RN-II nozzles, are also plotted in Figures 20 and 21, respectively. These figures show that (a) these nozzle admittances are practically independent of frequency and (b) both the real and imaginary parts of the nondimensional admittances are small numbers. These results further support the conclusion that over the tested frequency range, the small-scale models of the RN-I and RN-II exhaust nozzles provide little damping for longitudinal mode instabilities in rocket engines.

The measured admittance data will now be compared with available theoretical predictions[6,7] for the admittance of short nozzles. As stated in Chapter II, the results of the short nozzle theory are based upon the assumption that the length of the convergent section of the nozzle is much shorter than the wavelength of the oscillation. Under this restriction, the flow in the nozzle is expected to respond instantaneously to any changes in flow properties taking place at the nozzle entrance. Consequently, such nozzles are expected to behave in a quasi-steady manner. The short nozzle theory predicts (see Equation (2-36)) that the admittance of a short nozzle is a real number whose magnitude depends upon the properties of the gas and the magnitude of the Mach number at the nozzle entrance. If the predictions of the short nozzle theory are correct, then the measured admittances of such nozzles should be independent of frequency and they should have no imaginary part (i.e., such nozzles will cause no phase change between the incident and reflected pressure waves at the nozzle entrance). Since the test conditions and geometries of the tested models of the RN-I and RN-II nozzles satisfy the assumptions of the short nozzle theory, a comparison of the

test results with the prediction of this theory is warranted.

To check the applicability of the short nozzle theory[6,7], the predicted values of the real and imaginary parts of the nondimensional nozzle admittance y_N obtained from Equation (2-36) are compared with the measured admittance data of the tested small-scale RN-I and RN-II nozzles. The theoretically predicted admittance data for γ equal to 1.4 and the corresponding experimental data are summarized in Table 1.

An examination of the data of Table 1 and the data presented in Figures 20 and 21 leads one to conclude that both RN-I and RN-II nozzles behave like short nozzles in the sense that their admittances are independent of the frequency. However, the experimentally determined values of the real and imaginary parts of the nondimensional admittances are larger than the corresponding theoretical predictions.

Another parameter that is of interest in solid propellant rocket combustion instability studies is the nozzle decay coefficient α_N that provides a measure of the damping of a pressure oscillation in the chamber when the nozzle is the only means for transferring wave energy into or out of the system. Formulae for evaluating α_N using the experimentally determined admittance data are provided in Chapter II and in Appendix B of this thesis. The corresponding theoretical expression for the nozzle decay coefficient, $(\alpha_N)_t$, can be obtained by manipulating Equations (2-8), (2-31) and (2-36); that is,

$$\left(\Lambda_N\right)_t = \frac{\alpha_N L_c}{\bar{c}} = -\left(\frac{\gamma + 1}{2}\right) \bar{M} \qquad (4\text{-}2)$$

Letting $\gamma = 1.4$ and using the RN-I and RN-II test Mach numbers in Equation

Table 1. Study 1: Summary of the RN-I and RN-II Nozzle Admittance Data

Nozzle	Chamber Mach Number	Experimental Data					Theoretical Data based on Short Nozzle Theory		
		α	β	Γ	η	Λ_N	Γ	η	Λ_N
RN-II	0.06	0.012	0.480	0.038	0.063	-0.097	0.012	0.00	-0.072
RN-I	0.08	0.014	±0.495	0.044	±0.016	-0.123	0.016	0.00	-0.096
Orifice-nozzle	0.06	0.012	-0.490	0.038	-0.031	-0.097	0.012	0.00	-0.072
Orifice-nozzle	0.08	0.012	-0.485	0.038	-0.047	-0.118	0.016	0.00	-0.096

(4-2), the theoretically predicted values of Λ_N were calculated and they are also presented in Table 1 along with corresponding values of Λ_N determined by using experimental admittance data.

A comparison of the theoretically predicted and experimentally determined values of the nondimensional nozzle decay coefficients shows that the experimentally determined values are larger than the corresponding theoretical predictions. These data also indicate that the RN-I nozzle provides more damping than the RN-II nozzle; a result that is probably due to the higher mean flow Mach number at the RN-I nozzle entrance. In this connection it should be pointed out that both the theoretical and experimental predictions indicate that the nozzle decay coefficient increases with an increase in the magnitude of the mean flow Mach number at the nozzle entrance.

An additional check on the applicability of short nozzle theory was carried out by measuring the admittances of sharp-edged orifices drilled in a flat plate. In this study, two such orifice-nozzles were tested in the 11-3/8 inch diameter impedance tube at chamber Mach numbers of 0.06 and 0.08, respectively. The measured admittance data of these configurations were found to be practically independent of the frequency. This data is also presented in Table 1 where it is compared with the admittances of the RN-I and RN-II nozzles. An examination of this data provides further support to the observation that the short nozzle theory underestimates the damping provided by short nozzles.

In this section an attempt will be made to qualitatively explain the observed differences between the theoretically-predicted and experimentally-measured admittance data of short nozzles. An examination, for

example, of Figure 8, indicates that the manner in which the tested short nozzles are attached to the combustor gives rise to a step at the nozzle entrance plane. This step results in the flow stream separating from the chamber walls, at some location upstream of the nozzle entrance. When this occurs there exists a region, having nonuniformities in the steady state properties of the gas medium, separating the upstream uniform flow and the nozzle entrance plane. Hence, intuitively, the measured nozzle admittance of such a configuration must be influenced by both the nozzle and the non-uniform flow region. However, in theoretical analyses[6,7] of short-nozzle admittances the wave-energy loss due to dissipative processes present in the region just upstream of the nozzle entrance is neglected and the flow is assumed to be isoenergetic and isentropic everywhere in the flow field. Consequently, the predicted damping data accounts for damping provided by the nozzle only. When the damping provided by the short nozzle is very small (particularly, this would be so at low chamber Mach numbers) the damping provided by the nonuniform region may be of the same order of magnitude as the nozzle damping and thus possibly account for the observed difference between the predicted and measured short nozzle damping data. Marble[25] in a recent analysis of the response of short nozzles subject to one-dimensional disturbances considered the presence of entropy waves. For this situation, Marble has shown that the theoretical nondimensional nozzle admittance takes on the following form:

$$y_N = \left(\frac{\gamma - 1}{2}\right)\bar{M} + \frac{1}{2}\frac{(s_1/c_p)}{(p_1/\gamma\bar{p})}\bar{M} \qquad (4\text{-}3)$$

where s_1 is the entropy perturbation. In view of the above remarks, a comparison of the above equation with Equation (2-36) suggests that the

term $\frac{1}{2}\ \frac{(s_1/c_p)}{(p_1/\gamma\bar{p})}\ \bar{M}$ is a measure of the damping provided by the nonuniform region present upstream of the nozzle entrance.

The experimentally determined nozzle decay coefficients of the nozzles tested in this study will now be compared with the available data published in literature. According to Buffum et al.[9,10], who determined nozzle acoustic losses by use of the steady state resonant method as well as the pressure decay method, the nondimensional nozzle decay coefficient for longitudinal instabilities in a cylindrical chamber is given by the following empirical relationship:

$$\left(\Lambda_N\right)_E = - J \qquad (4-4)$$

where $J = S_{throat}/S_{chamber}$. According to Equation (2-33) and the data presented in Table 1, the nondimensional nozzle decay coefficients for cylindrical chambers outfitted with the RN-II and RN-I nozzles are

$$\begin{aligned} &\text{RN-II nozzle} \quad (\bar{M} = 0.06): \quad \left(\Lambda_N\right)_E = - \left(0.58 + \frac{0.038}{J}\right)J = -0.947J \\ &\text{RN-I nozzle} \quad (\bar{M} = 0.08): \quad \left(\Lambda_N\right)_E = - \left(0.58 + \frac{0.044}{J}\right)J = -0.90J \end{aligned} \qquad (4-5)$$

On the other hand, using Equations (2-32) and (4-2) yields the following expression for the theoretical nondimensional short nozzle decay coefficient:

$$\left(\Lambda_N\right)_t = - 0.69J \qquad (4-6)$$

A comparison of the formulae presented in Equations (4-4) through (4-6) shows a good agreement between the two experimental sets of data and considerable difference between the experimental and theoretical results. This comparison indicates that the available short nozzle theory underestimates the damping provided by short nozzles. It is also interesting to note that the good agreement between the experimental data was obtained in spite of the fact that the tested nozzles had considerably different geometries. This observation suggests that the damping provided by short nozzles is almost independent of the geometrical details of the nozzle designs and primarily depends upon the nozzle area ratio J. If the latter observation is indeed correct, then the evaluation and prediction of the damping provided by short nozzles of various geometrical designs will be considerably simplified.

The main conclusion of this study is that short exhaust nozzles provide little damping for axial instabilities. The measured admittances are independent of the frequency and they are larger than the admittances predicted by the short nozzle theory. Since longitudinal oscillations are independent of the shape of the cross section of the duct in which the oscillations are occurring, then it is quite plausible that the empirical results presented in Equation (4-5) are also applicable to real engines experiencing axial instabilities.

Study 2: Scaling of Nozzle Admittance Data

This study was designed to determine whether reliable nozzle admittance data may be obtained from cold flow, small-scale experiments. For this purpose, the tests conducted in Study 1 were repeated with the smaller of the two impedance tubes and the nozzles described in Chapter III. If

the previously stated scaling criteria (see the discussion in Chapter II) hold, then the tests conducted under Study 1 and Study 2 should yield comparable data.

The results obtained during the Study 2 investigation are presented in Figures 22 and 23. Examination of the data presented in these figures shows that, as in Study 1, the experimentally determined Study 2 admittance data are independent of the frequency and that the magnitudes of both the real and imaginary parts of the nondimensional admittance for the Study 2 nozzles are small. The experimentally determined admittance data of Study 2 are summarized in Table 2.

A comparison of the Study 2 data, presented in Figures 22 and 23 and summarized in Table 2, with the Study 1 data, presented in Figures 20 and 21 and summarized in Table 1, shows a good agreement between the two sets of data. This good agreement between Studies 1 and 2 data supports the assertion that the damping of axial instabilities by short nozzles can be determined by investigating the behavior of geometrically similar small-scale versions of the actual nozzles. It remains, however, to prove that the nozzle admittance data measured under cold flow conditions is also applicable to real engine operating conditions where the gases are considerably hotter than the air used for testing in this program. Investigation of this point would require the repetition of the Study 1 or Study 2 tests at elevated temperatures. The high temperature experiments were not attempted in this investigation.

To investigate whether, in general, reliable nozzle admittance data can be obtained by investigating the behavior of a geometrically similar small-scale model of the actual nozzle, the admittances of the nozzle shown

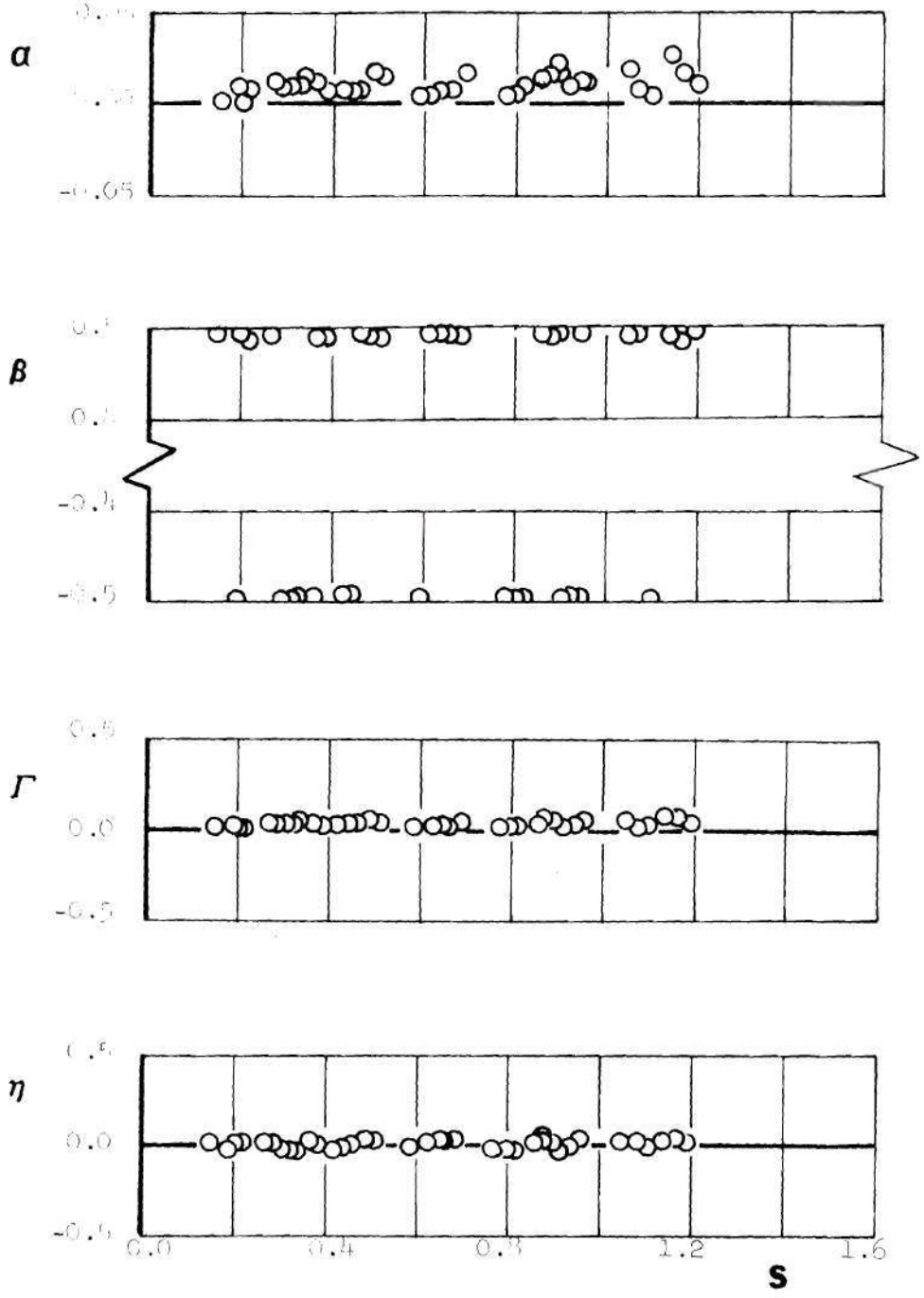

Figure 22. Study 2, Admittance Data of the Small-Scale RN-I Nozzle.

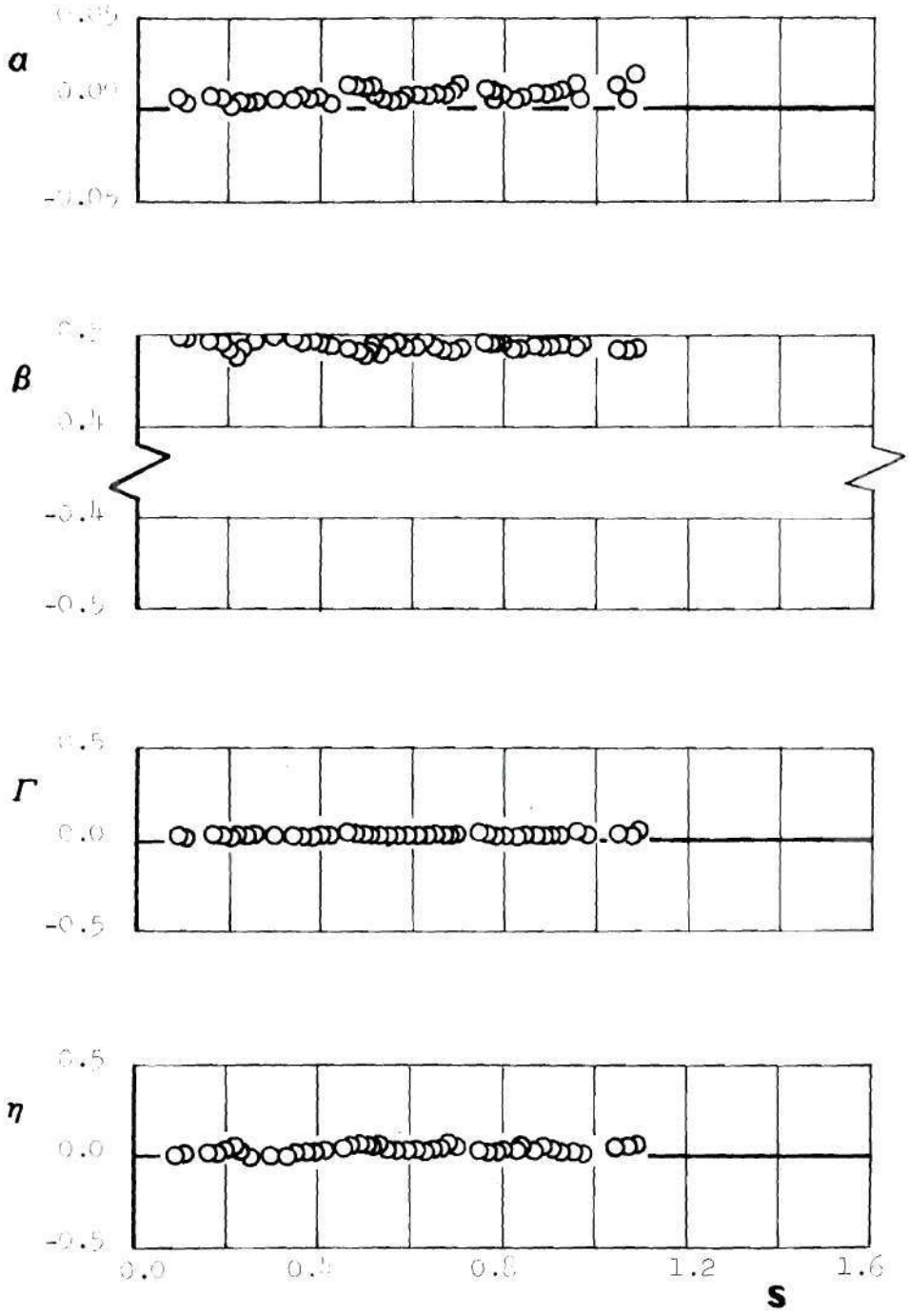

Figure 23. Study 2, Admittance Data of the Small-Scale RN-II Nozzle.

Table 2. Study 2: Summary of the RN-I and RN-II Nozzle Admittance Data

Nozzle	Chamber Mach Number	Experimental Data				
		α	β	Γ	η	Λ_N
RN-II	0.06	0.010	0.485	0.032	0.047	-0.091
RN-I	0.08	0.015	±0.495	0.047	±0.016	-0.126

in Figure 12 were measured and compared with *available*[15,18] admittances of a geometrically similar larger nozzle. It has been shown by Bell[15,18] that the magnitudes and the frequency dependence of the admittance of the nozzle geometrically similar to the one shown in Figure 12 are entirely different than the magnitudes and frequency dependences of the RN-I and RN-II nozzles. In studies by Bell, this nozzle was tested in the 11-3/8 inch diameter impedance tube while in the present study this nozzle was tested in the 7-5/8 inch diameter impedance tube. In this connection it should also be pointed out that Bell's experimental admittance data were found to be in good agreement with the predicted admittances obtained using Crocco's nozzle admittance theory.[5]

The measured frequency dependence of the real and imaginary parts of the nondimensional admittance y_N of the nozzle configuration of Figure 12 is presented in Figure 24. For comparison purposes the data of Reference 15 is also presented in this figure. Examination of this figure indicates that the two sets of experimental data do not quite agree with one another. A closer examination of this figure further indicates that while the two sets of data are similar in magnitudes and shapes, there is also a slight frequency shift between them. For example, the maximum value of Γ obtained during the present investigation occurs at $S = 0.99$ while the corresponding peak in the data presented in Reference 15 occurs at $S = 0.91$, indicating a frequency shift of 0.08.

In an effort to explain the observed frequency shift, the possibility of errors in the measured temperature, the calibration of the transducer systems, and the scaling procedures were investigated. When these checks produced no errors, the small-scale nozzle was measured to

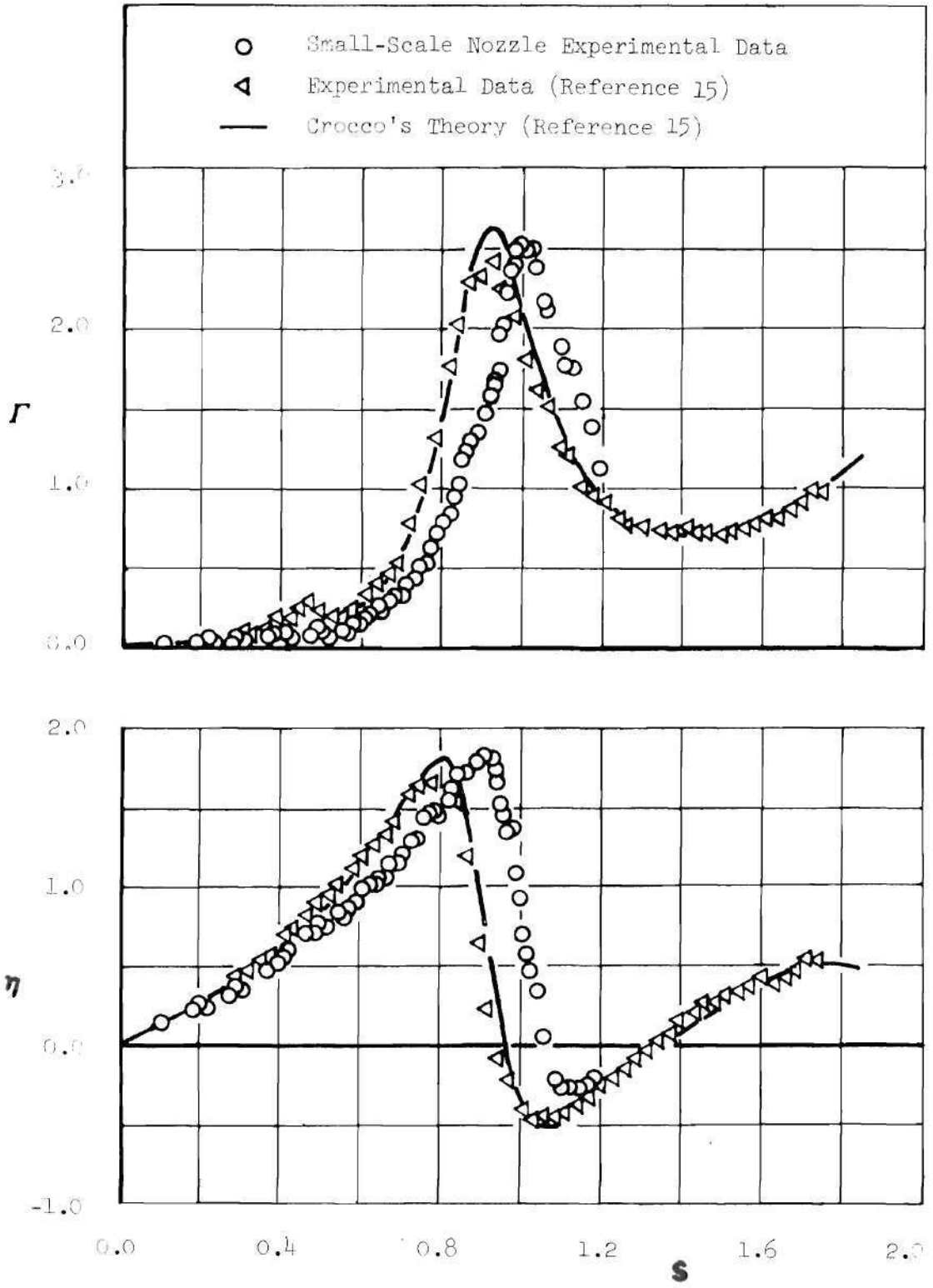

Figure 24. Admittance Data of the Small-Scale 15° "Long"Nozzle.

check whether it had been machined according to specifications. Referring back to Figure 12 it can be seen that the length of the convergent section of the nozzle is required to be 9.93 inches. For some unexplainable reasons, the small-scale nozzle had been machined with the length of the convergent section of the nozzle measuring 9.13 inches. It will now be shown that this discrepancy in the actual nozzle length is the cause for the observed frequency shift in the measured admittance data.

In Chapter II of this thesis Crocco's analysis was used to show how the admittance data of a reference nozzle can be employed to determine the admittances of a "family" of nozzles obtained by a linear "contraction" or "stretching" of the reference nozzle. It follows from this discussion that the admittances $(y_N)_f$ of the nozzle illustrated in Figure 12 (z_f = 9.93 inches) can be obtained from the measured admittances $(y_N)_{ref}$ by considering the nozzle of Figure 12 as a "stretched" version of the tested nozzle (z_{ref} = 9.13 inches). Using Equation (2-34) and the lengths of the reference and "stretched" nozzles, it can be shown that the scale factor σ that is associated with the "stretched" nozzle equals 1.09. Using Equation (2-35) the admittance data of the scaled nozzle illustrated in Figure 12 is given by

$$\left[(y_N)_f\right]_{S=S_f} = \left[(y_N)_{ref}\right]_{S=S_{ref.}} \tag{4-7}$$

where

$$S_f = S_{ref.}/\sigma \tag{4-8}$$

To illustrate the use of Equations (4-7) and (4-8) the frequency at which the real part of the nondimensional admittance of the "stretched" nozzle

is a maximum will be calculated. It is shown in Figure 24 that the corresponding maximum for the "reference" nozzle occurs at $S_{ref} = 0.99$. Using the scale factor the maximum value in Γ for the "stretched" nozzle occurs at $S_f = 0.99/1.09 = 0.91$. As mentioned earlier in this discussion this was the frequency at which the maximum value in Γ was observed in Reference 15. Equation (4-8) can be rewritten as

$$S_{ref} - S_f = \frac{\sigma - 1}{\sigma} S_{ref} \qquad (4\text{-}9)$$

With $\sigma = 1.09$, Equation (4-9) reduces to $(S_{ref} - S_f) = 0.0825 S_{ref}$. This is the frequency correction that needs to be applied to the measured admittance data in order to obtain the admittance data of the "stretched" nozzle. Applying the above-mentioned frequency correction to the measured data presented in Figure 24, the admittance data of the "stretched" nozzle was obtained and is presented in Figure 25. An examination of this figure indicates that the admittance data of the "stretched" nozzle is in good agreement with the corresponding data of Reference 15. As mentioned earlier, the "stretched" nozzle is the one which is geometrically similar to the nozzle tested in Reference 15.

The main conclusion of this study is that the damping of axial instabilities by "short" and "long" full-scale nozzles can be investigated by experimentally investigating the behavior of geometrically similar small-scale nozzles.

Study 3: Dependence of Nozzle Damping upon Cavity Depth and Secondary Flow Rate

Prior to ignition, the cavity surrounding a submerged nozzle in a rocket engine is almost completely filled with solid propellant (see Figure 6). After ignition, the surface of the burning solid propellant recesses

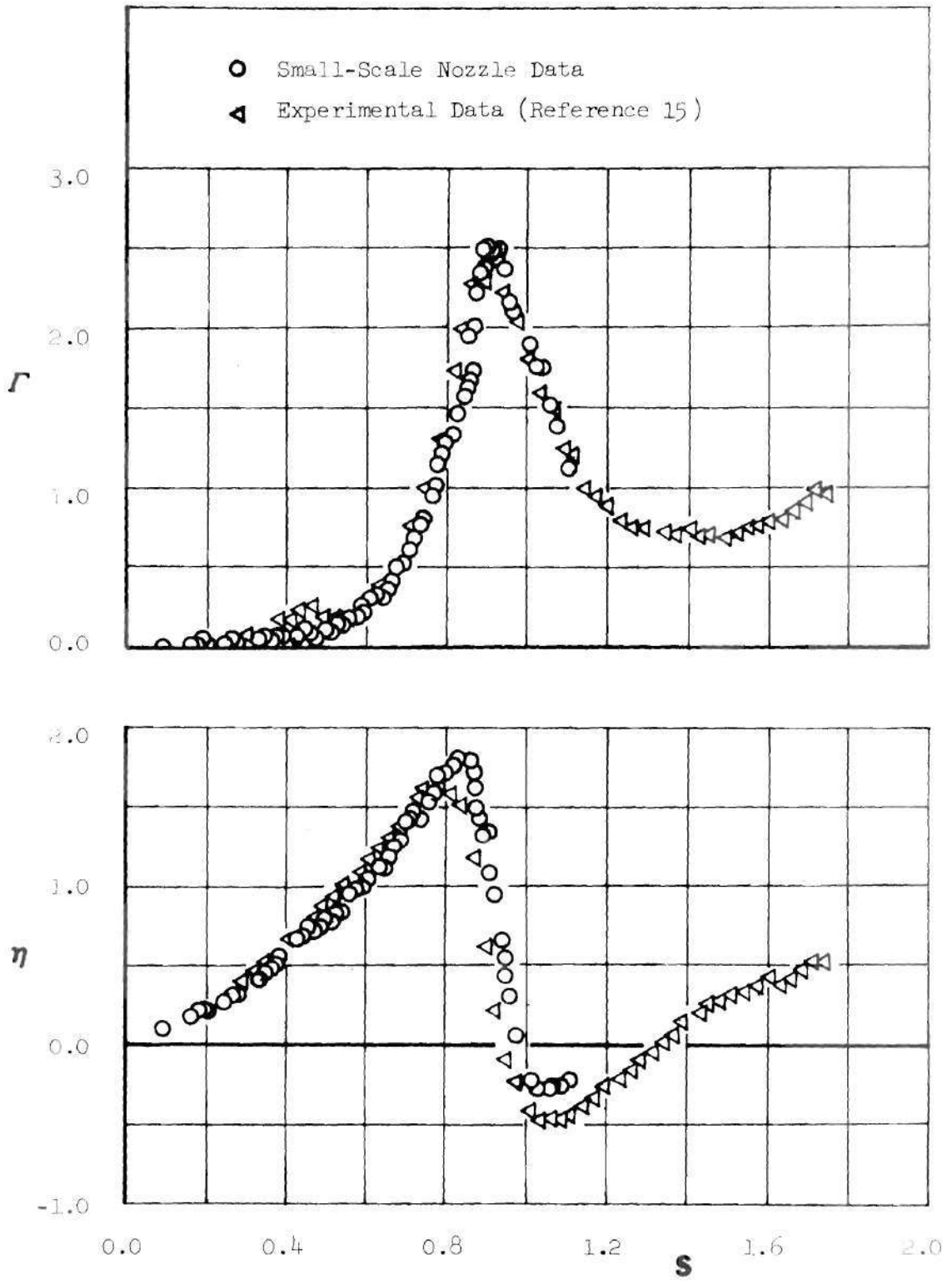

Figure 25. Comparison of 15° Small-Scale Nozzle Admittance Data with Data of Reference 15.

inward resulting in an increase with time of the volume and depth of the cavity surrounding the nozzle, and the flow rate of hot gases issuing from this cavity. Study 3 was designed to determine the effects of these changes upon the damping capabilities of the RN-I nozzle. To achieve this objective, the damping provided by the RN-I nozzle was measured with cavities of different depths surrounding the RN-I nozzle and with different flow rates of secondary flow issuing from this cavity. Detailed description of the experimental setup used in Study 3 investigation is provided in Chapter III.

To determine the dependence of the RN-I nozzle damping upon the desired range of parameters, tests with cavity depths varying between zero to 24 inches and secondary-to-primary flow rate ratios varying between zero and 25 percent were conducted under the Study 3 test program. The needed admittance data were obtained from pressure amplitude measurements and the significant results of this study are presented in Table 3; only the data required for discussing the observed experimental results are graphically presented in this section. However, before presenting the results of Study 3, some comments regarding the special geometrical features of the tested configuration are in order. The situation can be best explained by referring to Figure 13 and considering the unsteady flow conditions at the nozzle entrance plane. When a plane wave generated inside the modified impedance tube reaches the nozzle entrance plane it "splits" into two waves with one of them moving into the centrally-located nozzle and the other moving into the surrounding cavity. As a result, the local flow conditions at the nozzle entrance plane are non-uniform and the flow there cannot be one-dimensional. This situation is contrary to the previously used assumption that the flow at the nozzle entrance is one-dimensional. Since the frequencies tested in this program are below the

Table 3. Study 3: Summary of the Submerged RN-I Nozzle Admittance Data.

Cavity Depth, L_{cavity} (inches)	Secondary to Primary Flow Rate Ratio q (%)	Chamber Mach Number $\bar{M}$	Nondimensional Frequency S	Experimental Admittance Data α	β	Γ	η	Secondary Flow Mach Number $\bar{M}_s$	$\frac{L_{cavity}}{\lambda}$
0	0	0.080	All	0.014	0.488	0.044	0.037	0.000	0.00
8	0	0.080	1.080	0.014	0.000	---	---	0.000	0.24
16	0	0.080	0.560	0.015	0.000	---	---	0.000	0.25
16	0	0.080	1.680	0.015	0.000	---	---	0.000	0.75
24	0	0.080	0.380	0.016	0.000	---	---	0.000	0.26
24	0	0.080	1.170	0.016	0.000	---	---	0.000	0.78
0	5	0.076	All	0.014	0.485	0.044	0.048	0.007	0.00
8	5	0.076	1.080	0.015	0.000	---	---	0.007	0.24
16	5	0.076	0.560	0.015	0.000	---	---	0.007	0.25
16	5	0.076	1.700	0.016	0.000	---	---	0.007	0.76
24	5	0.076	0.370	0.012	0.000	---	---	0.007	0.25
24	5	0.076	1.130	0.015	0.000	---	---	0.007	0.76
0	10	0.073	All	0.016	0.480	0.050	0.063	0.011	0.00
8	10	0.073	1.080	0.016	0.000	---	---	0.011	0.24
16	10	0.073	0.560	0.020	0.000	---	---	0.011	0.25
24	10	0.073	0.390	0.025	0.000	---	---	0.011	0.26
24	10	0.073	1.130	0.025	0.000	---	---	0.011	0.76

Table 3. (Concluded)

L_{cavity}	q	$\bar{M}$	S	α	β	Γ	η	$\bar{M}_s$	$\frac{L_{cavity}}{\lambda}$
0	15	0.070	All	0.019	0.490	0.060	0.030	0.016	0.00
8	15	0.070	1.090	0.018	0.000	---	---	0.016	0.24
16	15	0.070	0.540	0.019	0.000	---	---	0.016	0.24
16	15	0.070	1.650	0.021	0.000	---	---	0.016	0.74
24	15	0.070	0.370	0.022	0.000	---	---	0.016	0.25
24	15	0.070	1.110	0.024	0.000	---	---	0.016	0.75
0	20	0.067	All	0.020	0.485	0.063	0.047	0.021	0.00
8	20	0.067	1.100	0.021	0.000	---	---	0.021	0.25
16	20	0.067	0.560	0.020	0.000	---	---	0.021	0.25
16	20	0.067	1.670	0.022	0.000	---	---	0.021	0.75
24	20	0.067	0.370	0.020	0.000	---	---	0.021	0.25
24	20	0.067	1.120	0.025	0.000	---	---	0.021	0.76
0	25	0.064	All	0.022	0.485	0.069	0.047	0.026	0.00
8	25	0.064	1.120	0.023	0.000	---	---	0.026	0.25
16	25	0.064	0.570	0.022	0.000	---	---	0.026	0.26
16	25	0.064	1.660	0.024	0.000	---	---	0.026	0.75
24	25	0.064	0.370	0.022	0.000	---	---	0.026	0.25
24	25	0.064	1.120	0.024	0.000	---	---	0.026	0.25

cutoff frequencies of the transverse modes, the above-mentioned non-uniformities are "concentrated" around the nozzle entrance plane and they cannot propagate in the upstream direction. Keeping these facts in mind, the admittances measured in this study should be interpreted as effective admittances that describe average conditions across the nozzle entrance plane. Stated differently, the admittances measured in this study are the effective one-dimensional nozzle admittances as "seen" by the one-dimensional waves inside the modified impedance tube.

The dependence of the admittance parameters α and β and the real and imaginary parts of the nondimensional admittance upon the cavity depth is presented in Figure 26. The dependence of the RN-I nozzle admittance upon the cavity-to-chamber flow rate ratio is presented in Figures 27 and 28.

In examining the tabulated Study 3 data, one should note that the Mach number of the primary flow $\bar{M}$ slightly decreases as the ratio of the secondary-to-primary flow rate increases. This is caused by the fact that part of the flow exhausted by the nozzle is supplied by the secondary flow issuing from the cavity. The resulting mean flow Mach number in the chamber is determined by computing the increase in the main chamber cross-sectional area that would be necessary in order to accommodate both the secondary and primary flow rates.

Examination of the measured values of the admittance parameter α, which reflects the change in amplitude between the incident and reflected pressure waves, shows that α is practically independent of frequency and that its average value is close to the average values of α measured in Study 1. A closer examination of Study 3 data seems to suggest that the

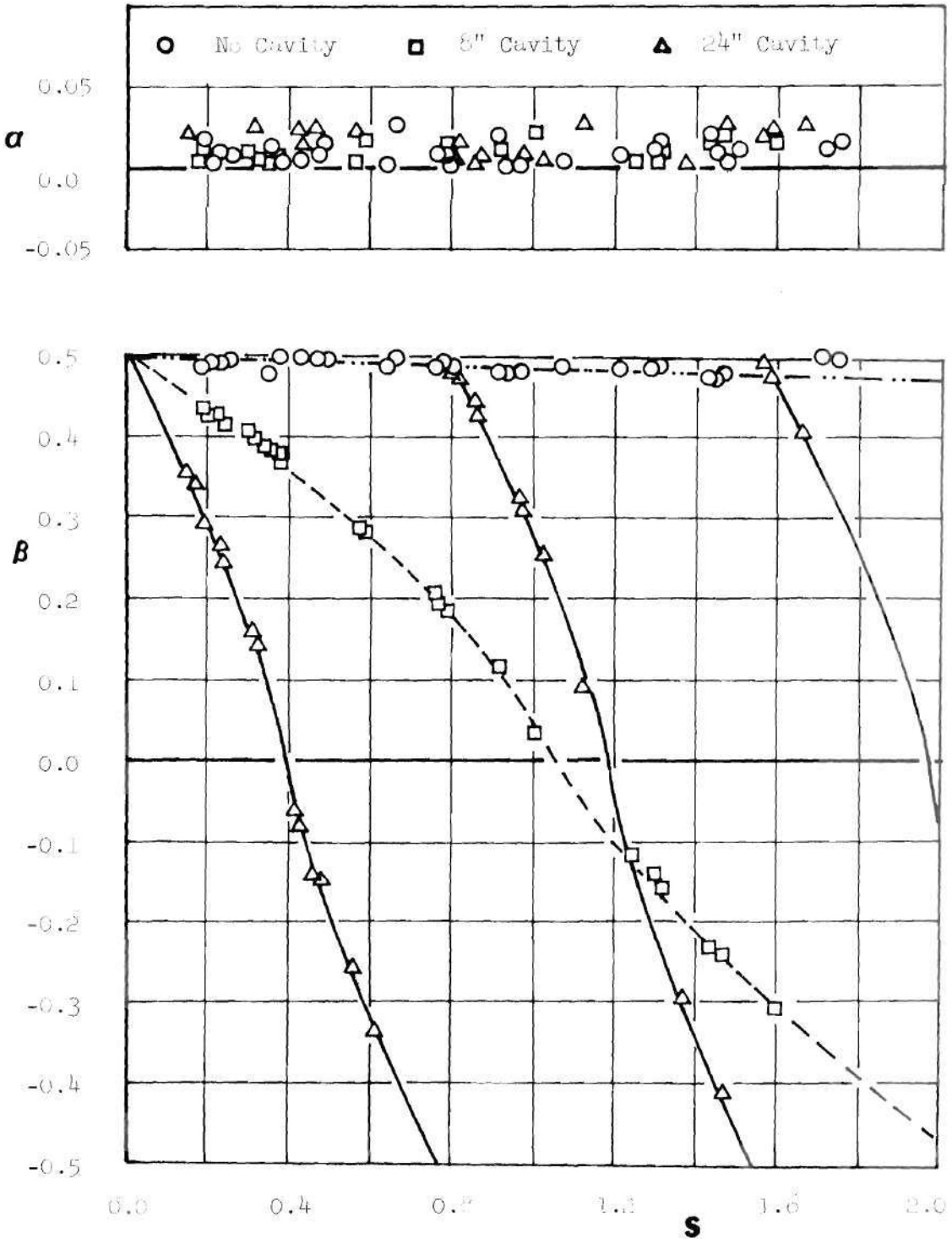

Figure 26. Effect of Nozzle Cavity Depth on the Admittance Data of the RN-I Nozzle; No Cavity Flow.

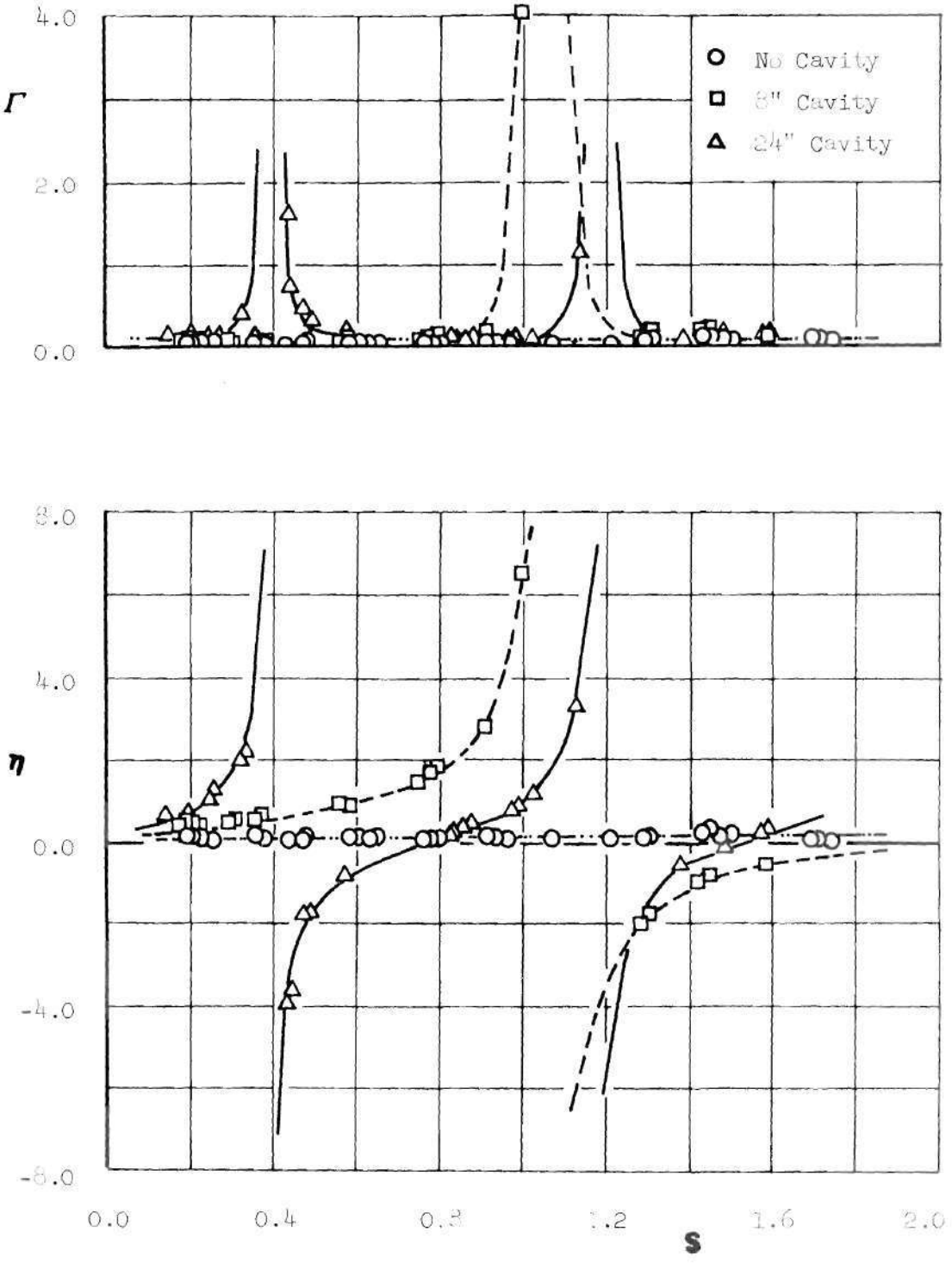

Figure 26. Concluded.

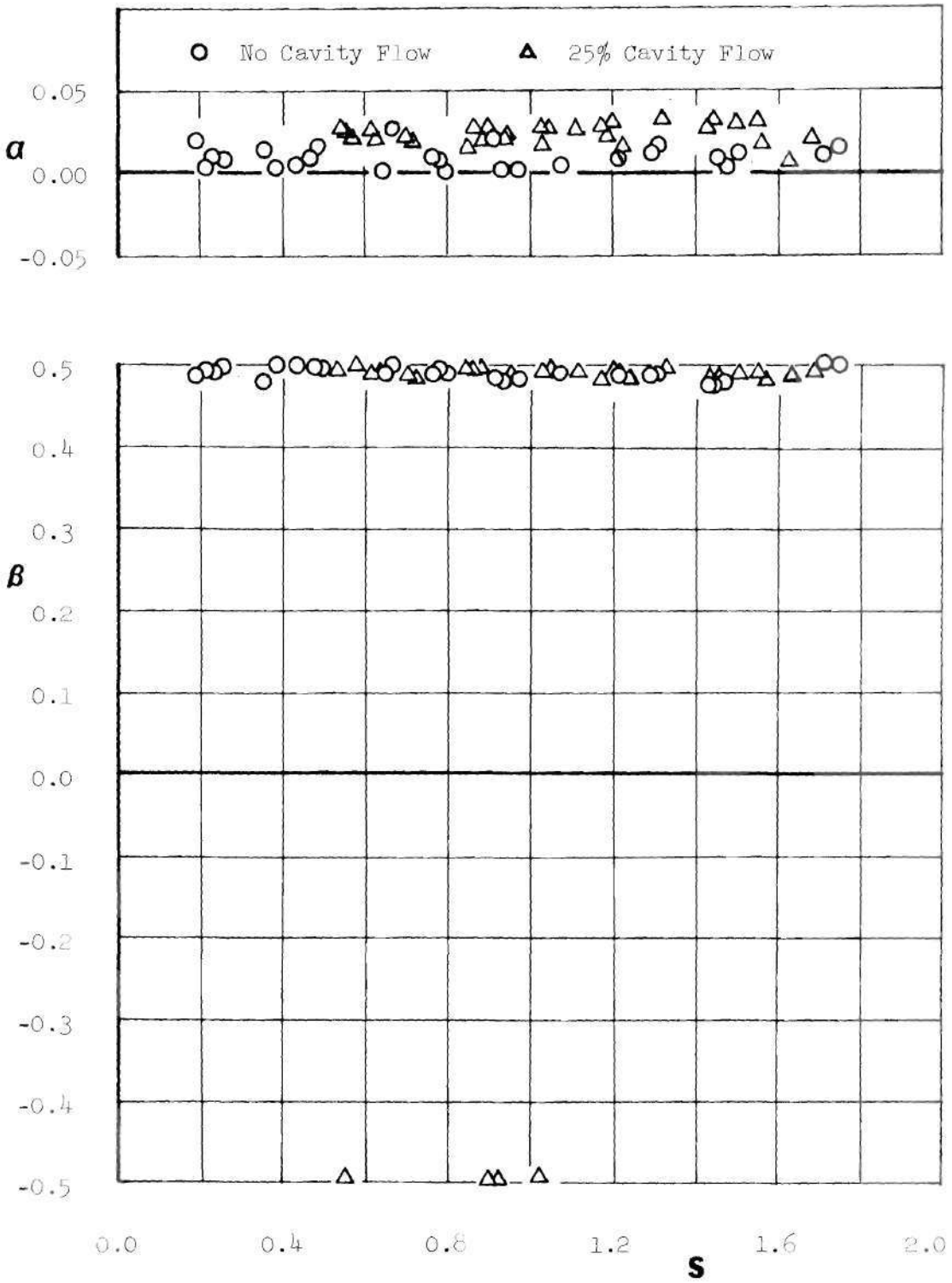

Figure 27. Effect of Nozzle Cavity-to-Chamber Flow Rate Ratio on the Admittance of the RN-I Nozzle; Zero Cavity Depth.

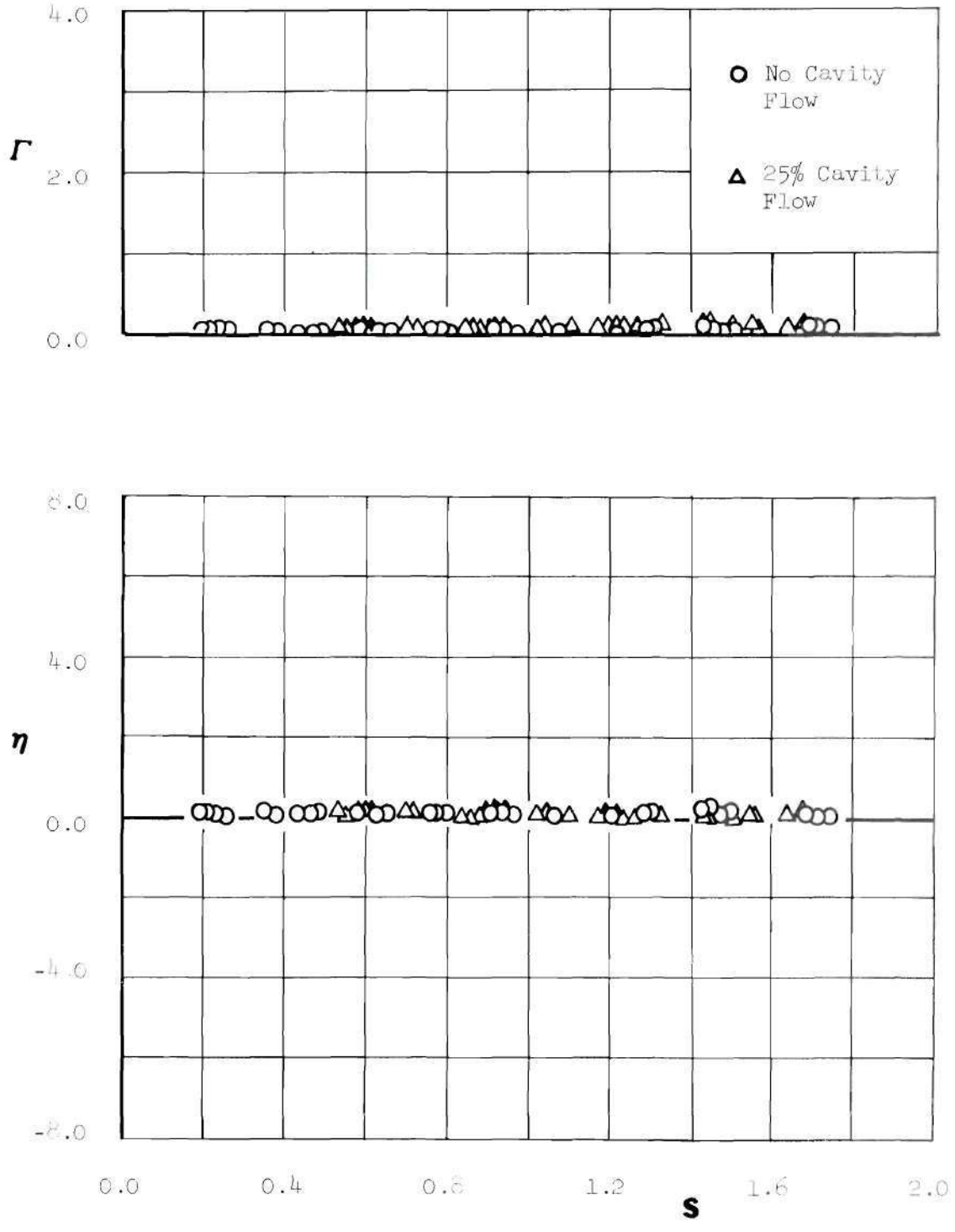

Figure 27. Concluded.

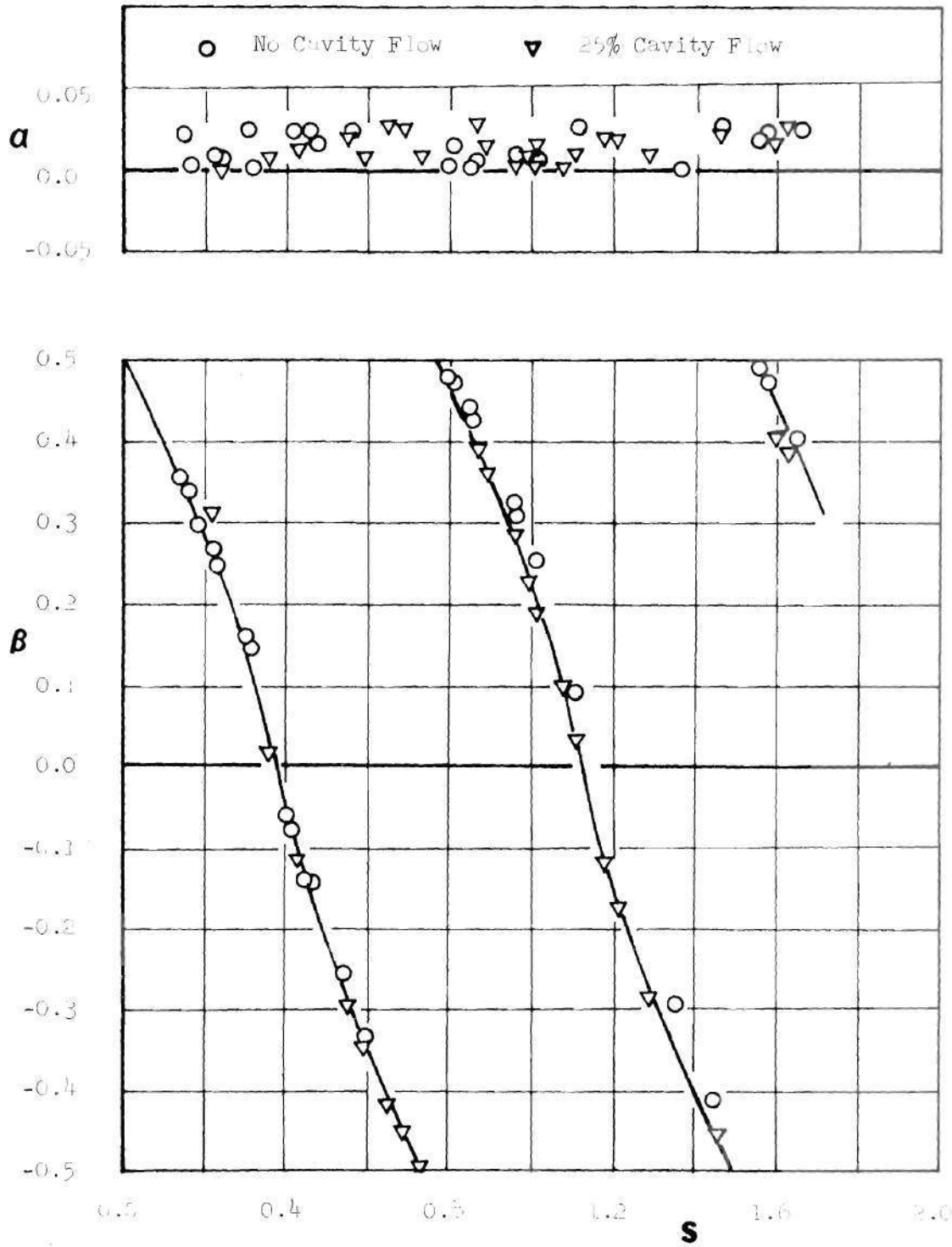

Figure 28. Effect of Nozzle Cavity-to-Chamber Flow Rate Ratio on the Admittance of the RN-I Nozzle; 24" Cavity Depth.

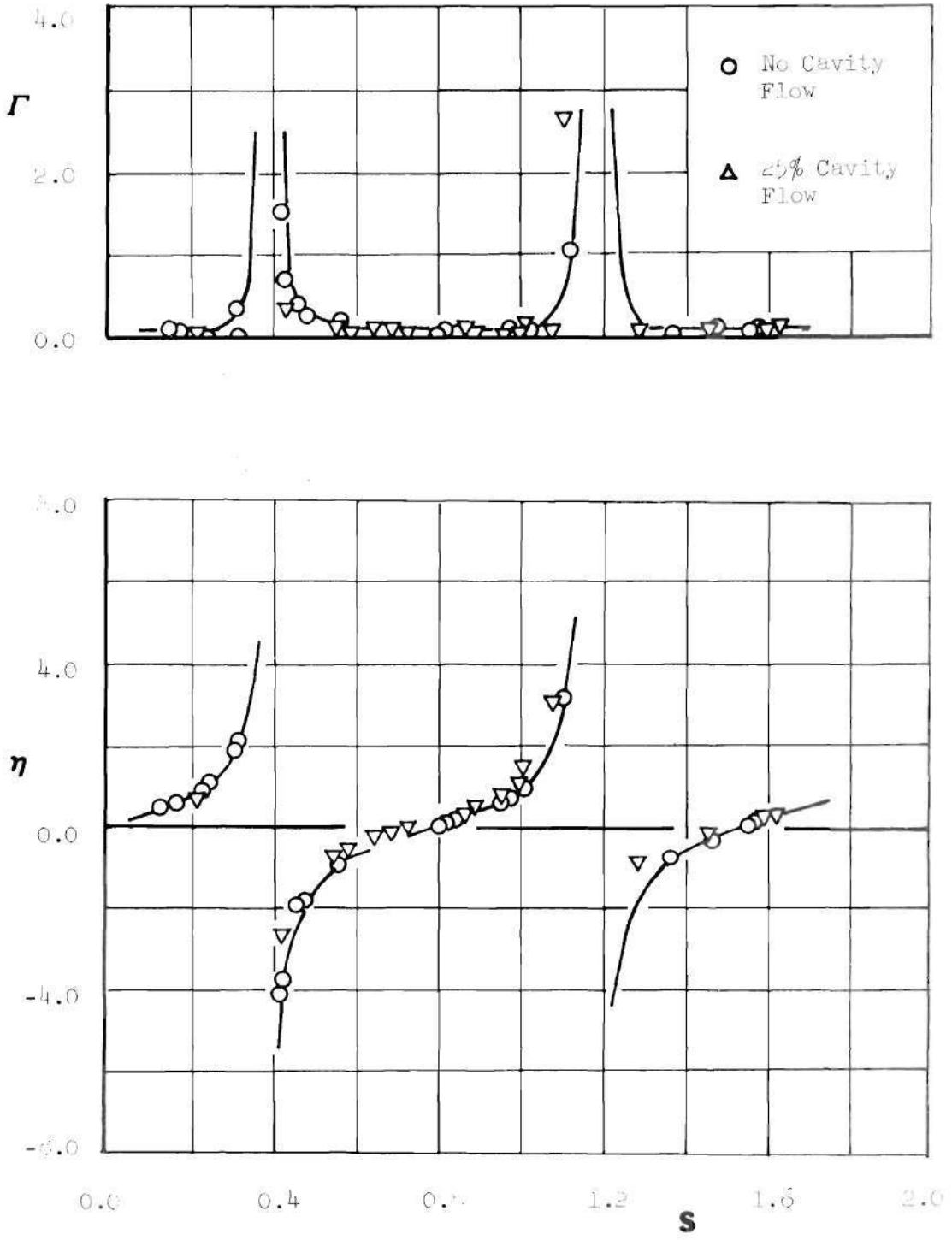

Figure 28. Concluded.

value of α slightly increases with increase in cavity depth. This increase in α can perhaps be explained by the higher wave attenuation caused by the longer wave travel distances that are associated with the deeper cavities.

Examination of the measured values of the admittance parameter β indicates that the magnitude of β is strongly affected by the depth of the cavity surrounding the nozzle. According to Equation (2-7), the parameter β describes the phase difference at the nozzle entrance plane between the incident and the reflected pressure waves. When β is identically zero, the phase θ between the incident and reflected pressure waves equals to π radians. Such a phase difference is known to exist at the opening of a quarter-wave tube when the ratio of the tube length to the wavelength of the oscillation equals 0.25, 0.75, 1.25, and so on. To check whether the cavity surrounding the nozzle acts as a quarter-wave tube, the following relationship was used to compute the ratio of the cavity depth to the wavelength when the measured values of β were identically zero:

$$\frac{L_{cavity}}{\lambda} = \frac{L_{cavity}}{(2\pi r_c/S)} \qquad (4\text{-}10)$$

The values of S for which $\beta = 0$ and the corresponding values of the ratio L_{cavity}/λ are presented in Table 3. The closeness of the computed values of L_{cavity}/λ to 0.25 and 0.75 provides a strong support to the conjecture that at the indicated frequencies the cavity surrounding the nozzle indeed behaves as a quarter-wave tube.

Examination of the results presented in Figures 26 through 28 shows

that the admittance y_N at the nozzle entrance plane is practically independent of the cavity flow rate. These figures also indicate that the behavior of the measured admittance ratio is strongly dependent upon the depth of the cavity surrounding the nozzle. The latter observation is directly related to the strong dependence of the admittance parameter β upon the depth of the cavity surrounding the nozzle. It is also of interest to analyze the behavior of Γ, the measured real part of the nondimensional nozzle admittance. Examination of the data reveals that Γ becomes very large at values of the nondimensional frequency S for which $\beta = 0$. In trying to explain this behavior one should recall the definition of the admittance (i.e., see Equation (2-1)) and examine the structure of the acoustic wave in the chamber and the cavity. At frequencies for which the measured value of β is zero, the cavity acts as a quarter-wave tube and the amplitude of the longitudinal pressure oscillation has a minimum value at the nozzle entrance plane. The larger values of Γ_E are caused by the fact that the value of Γ_E is inversely proportional to the pressure amplitude.

In connection with the above observation it should also be pointed out that it would be misleading to conclude that the nozzle attenuation coefficient α_N is very large whenever Γ is very large. If one examines Equation (2-23), one can see that α_N is proportional to the product $|P_N|^2 \, \mathrm{Re}\{Y_N\}$, and due to the smallness of pressure amplitude $|P_N|$ this product will be finite even though $\mathrm{Re}\{Y_N\}$ is a very large number. In addition, the results presented in the Appendix B illustrate that α_N is proportional to the admittance parameter α, which is practically independent of the frequency according to all of the Study 3 data; hence the α_N

of the submerged RN-I nozzle is also practically independent of the frequency. The above observations are meant to sound a word of caution to those who use the real part of the admittance of a surface as the sole criterion for determining the influence of this surface upon the stability of the system under consideration. To obtain a proper evaluation of the influence of a given boundary upon system stability, one must consider the magnitudes of both the real part of the admittance as well as the square of the pressure amplitude at the location under consideration; the product of these two quantities must be finite. This discussion might also suggest that the use of admittances in the study of combustion instability problems might be misleading and should perhaps be eliminated.

It should be pointed out that Equation (2-29) cannot be employed to determine the decay coefficient α_N of the submerged nozzle configuration. This can be explained by referring to Figure 13 and considering the steady flow directions at the nozzle entrance plane. The secondary air flow from the cavity is flowing in a direction opposite to that of the primary chamber air flow and hence is "convecting" acoustic energy from the cavity to the chamber. Equation (2-29) was derived from Equation (2-20) based on the assumption that all the flow in the nozzle entrance plane was unidirectional. The decay coefficient for a combustor with a submerged nozzle can be obtained from the measured admittance data and Equation (2-20) by suitably taking into consideration the steady flow directions at the nozzle entrance plane before performing the indicated spatial integration (see Appendix B for details).

The conclusions that follow from this study are (a) during axial instabilities in a rocket engine with a submerged nozzle there is wave

motion in both the combustor and the cavity surrounding the submerged nozzle, (b) the depth of the cavity surrounding the submerged nozzle has a significant effect upon the measured nozzle admittance, and (c) the secondary flow rates issuing from the submerged nozzle cavity have negligible effect on the nozzle admittance. Good judgment should be exercised when using the real part of the nozzle admittance to evaluate the effect of the surface in question upon engine stability. Finally, steady flow directions at the nozzle entrance plane should be suitably taken into consideration while calculating the decay coefficient for a combustor with a submerged nozzle.

Study 4: Dependence of Nozzle Damping upon Convergent Section Geometry

The acoustic losses associated with a rocket nozzle of a given contraction ratio depend upon the geometry of the nozzle convergent section and the manner in which the nozzle is attached to the combustor. This study was undertaken to determine the dependence of the damping of solid rocket nozzles upon the geometry of the nozzle convergent section. To determine this geometrical effect, the damping provided by a conical nozzle, an equal-radii-of-curvature nozzle and a linear-velocity-profile nozzle was measured. Descriptions of the nozzles tested in this study are given in Chapter III. The nozzles were initially tested with a Mach number of 0.05 in the impedance tube and they were later remachined and tested with a chamber Mach number of 0.10.

The nozzle admittance data measured in this study are presented in Figures 29 through 34. The figures pertaining to each of the nozzles include the frequency dependence of the measured admittance parameters α and β as well as the values of the real and imaginary parts of the

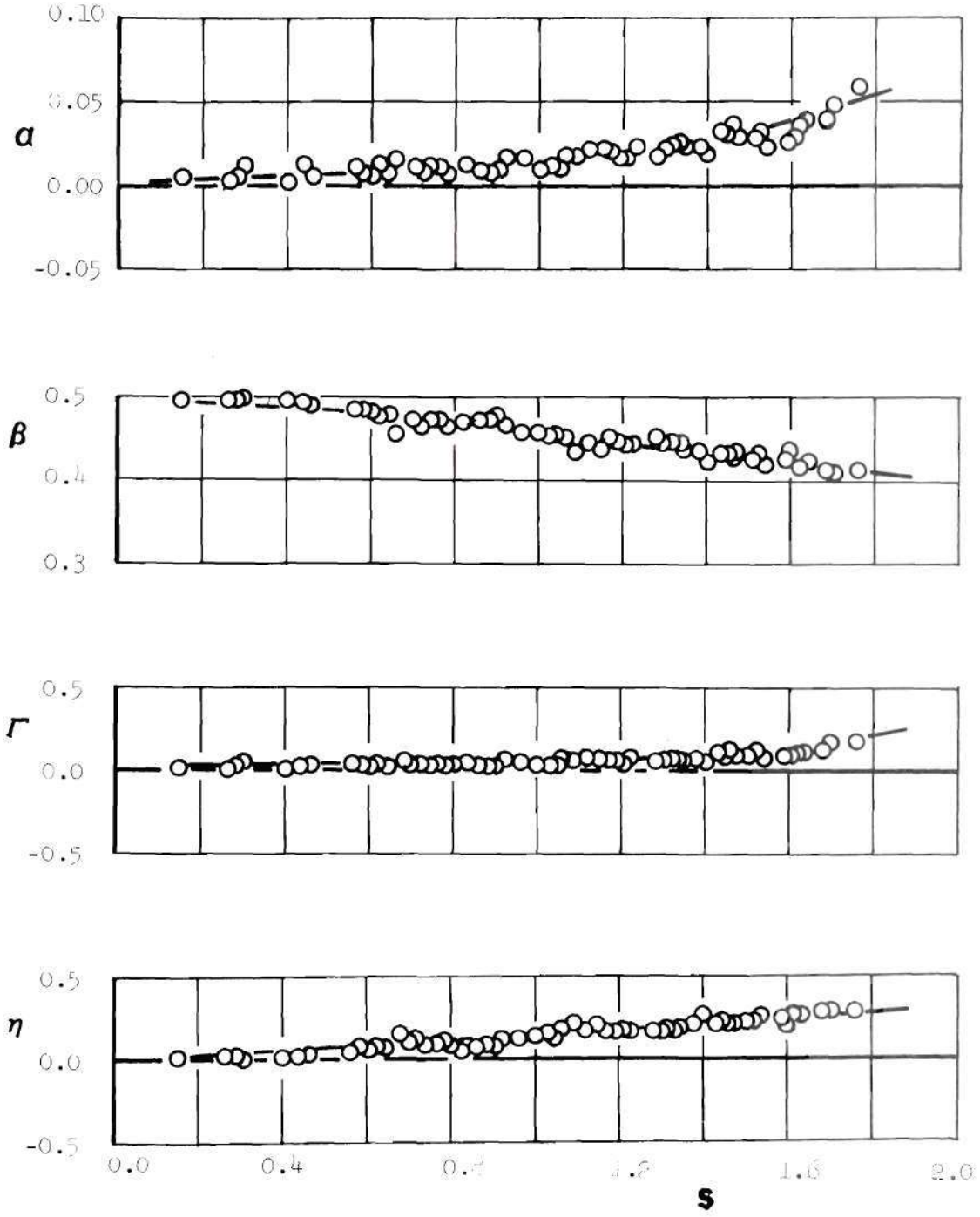

Figure 29. Frequency Dependence of the Admittance Data of the Conical Nozzle with $\bar{M}$=0.05.

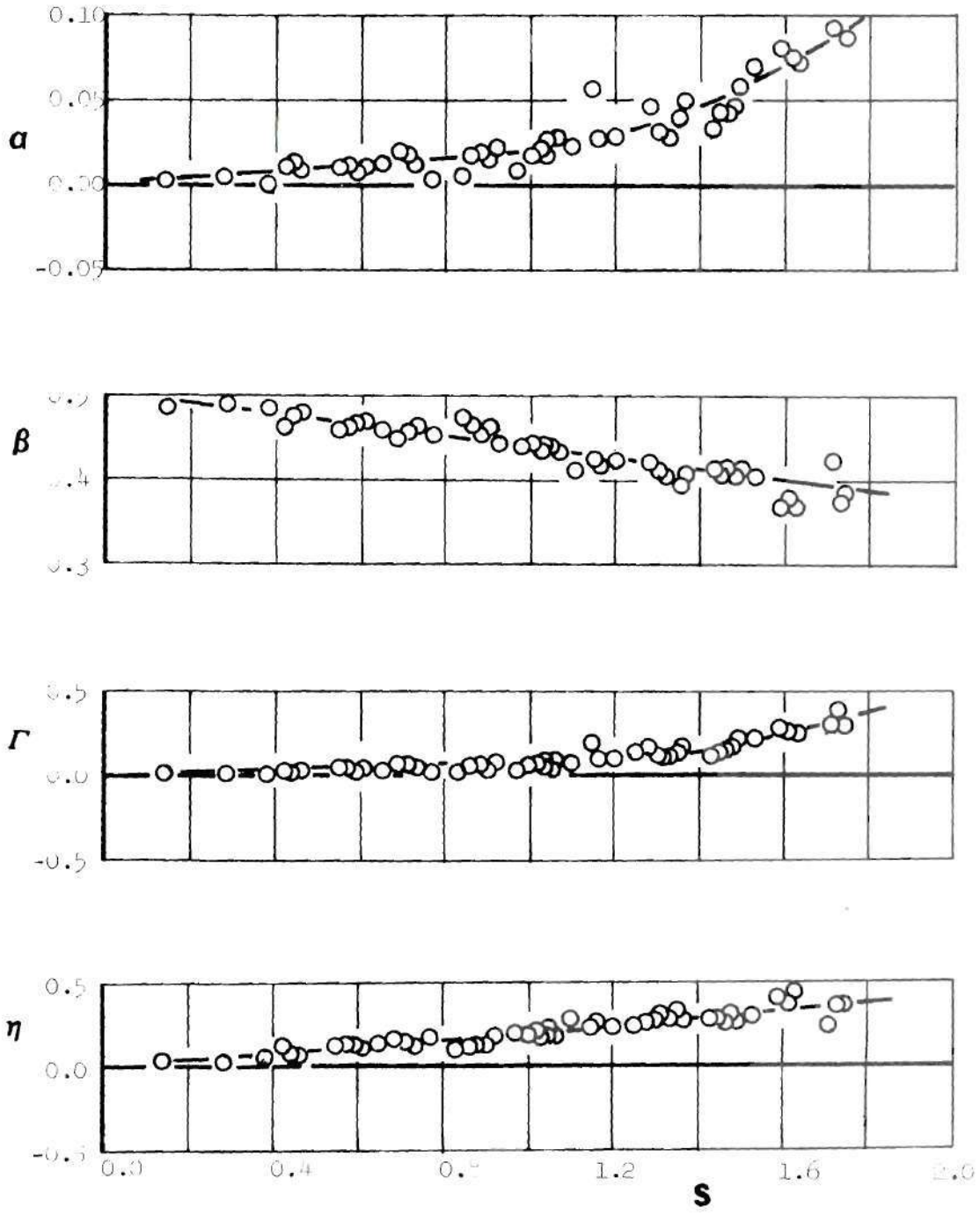

Figure 30. Frequency Dependence of the Admittance Data of the Conical Nozzle with $\bar{M}$ = 0.10.

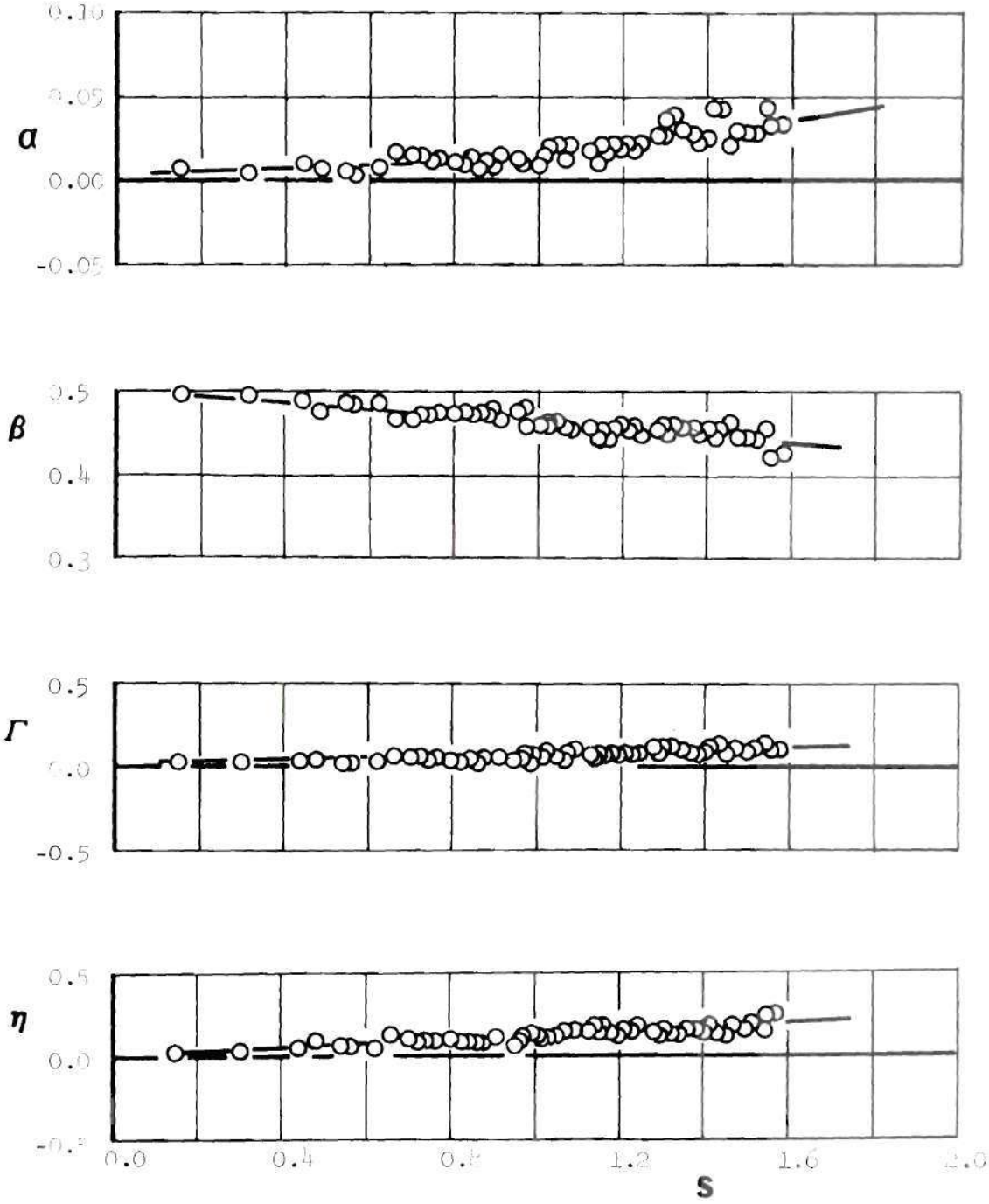

Figure 31. Frequency Dependence of the Admittance Data of the Equal-Radii-of-Curvature Nozzle with $\bar{M} = 0.05$.

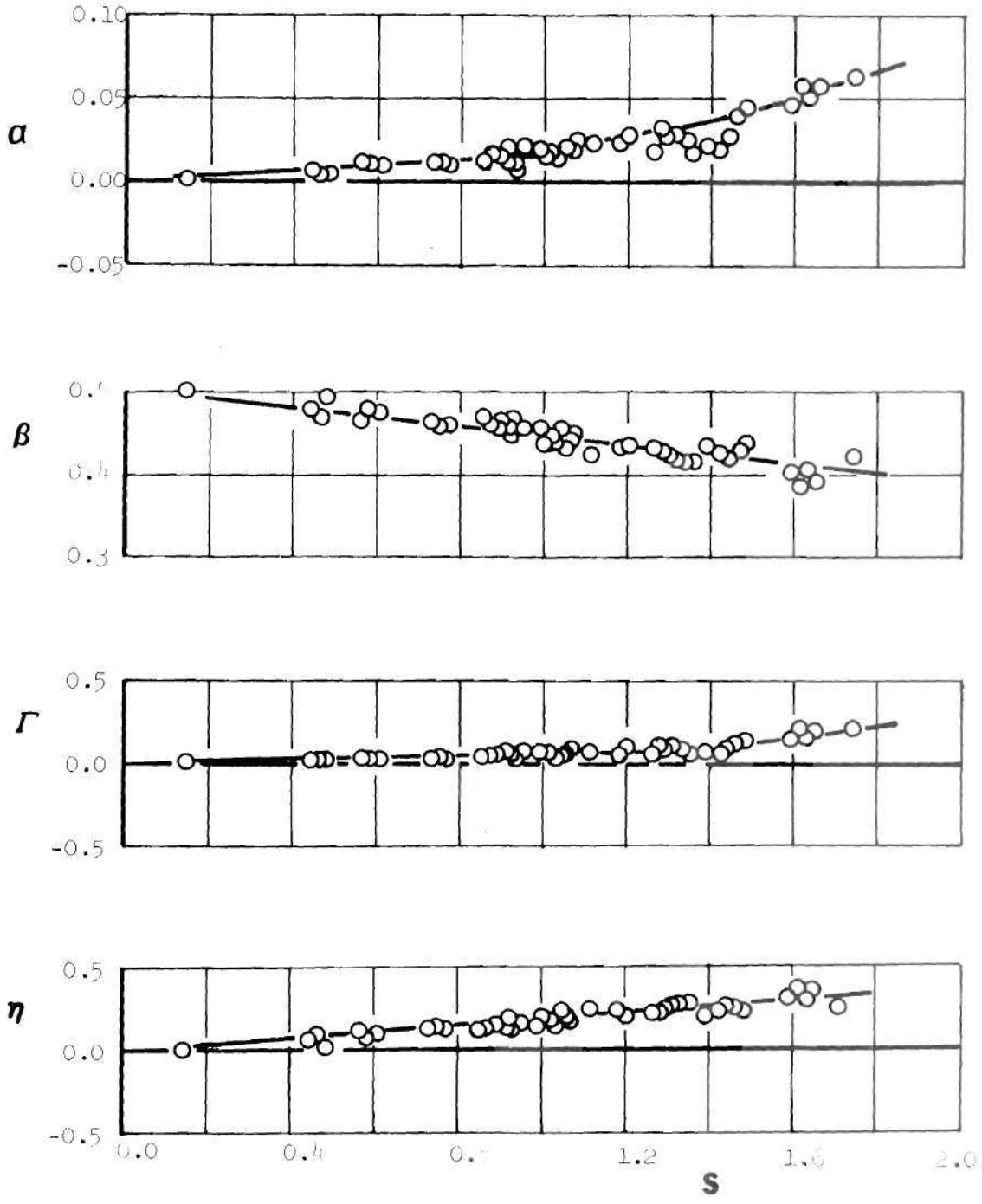

Figure 32. Frequency Dependence of the Admittance Data of the Equal-Radius-of-Curvature Nozzle with $\bar{M} = 0.10$.

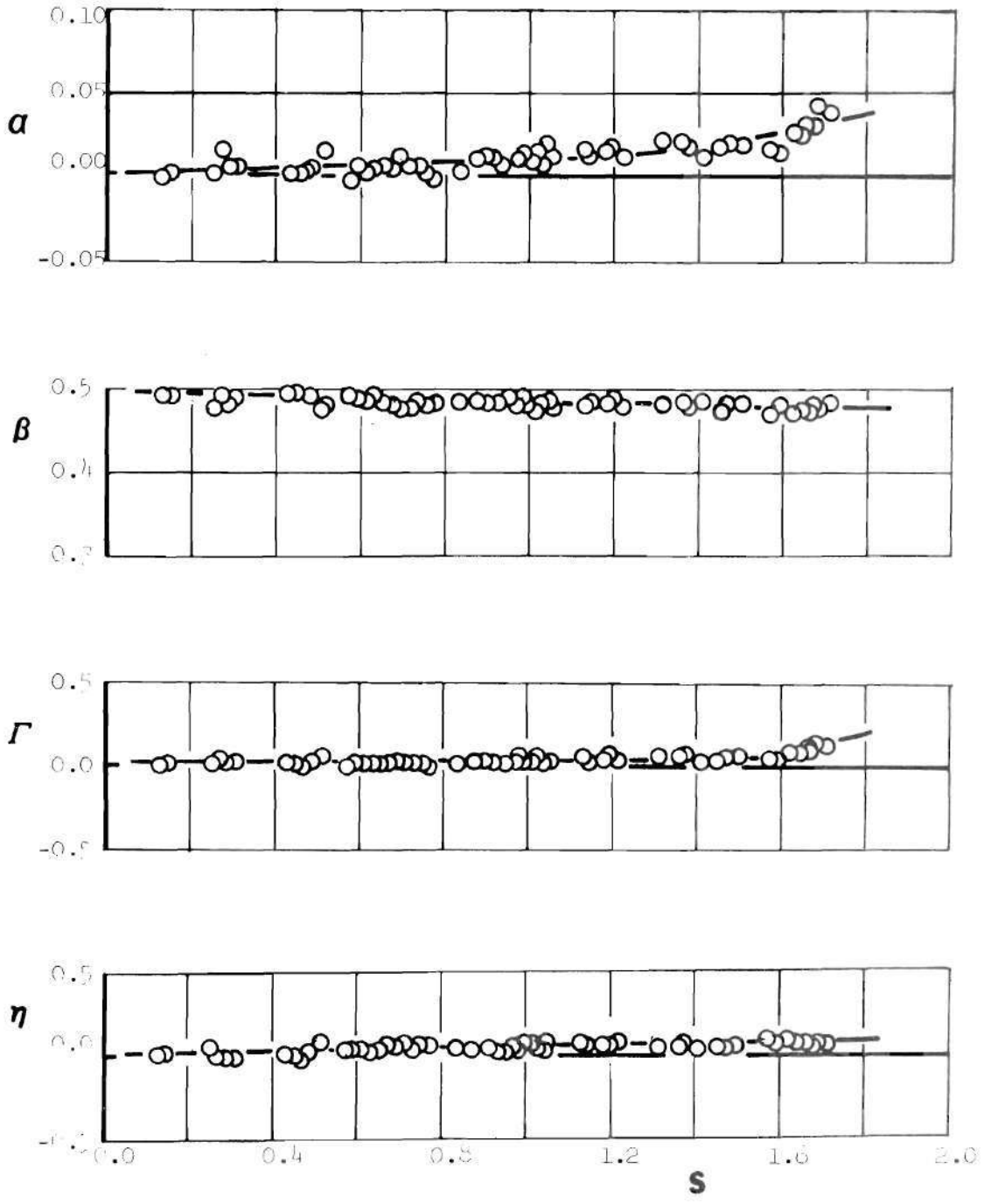

Figure 33. Frequency Dependence of the Admittance Data of the Linear-Velocity-Profile Nozzle with $\bar{M} = 0.05$.

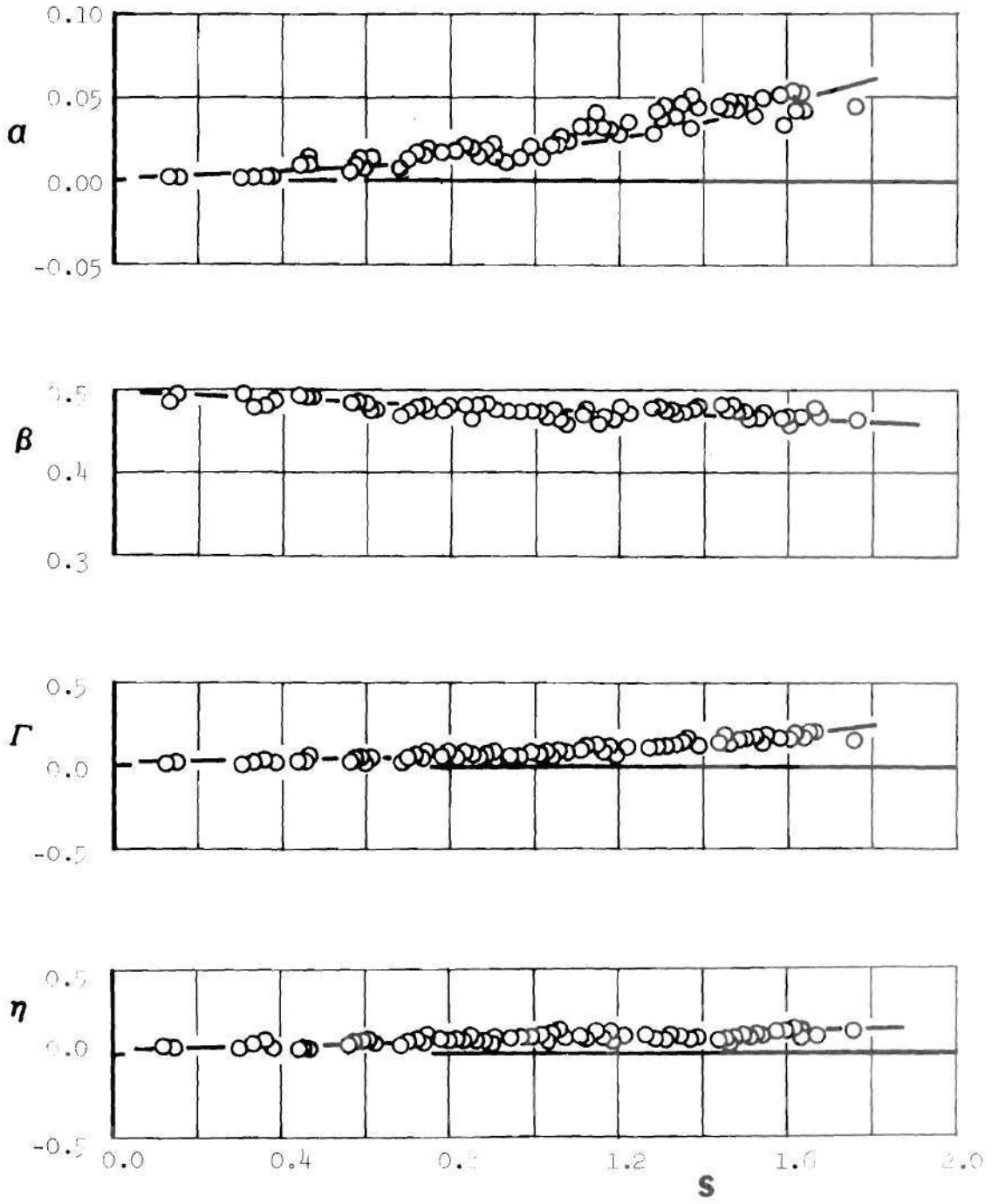

Figure 34. Frequency Dependence of the Admittance Data of the Linear-Velocity-Profile Nozzle with $\bar{M} = 0.10$.

nondimensional admittance y_N.

In order to assess the effect of the convergent section geometry on the damping effectiveness of the tested nozzles, the data presented in Figures 29 through 34 have been replotted for comparison in Figure 35 for chamber Mach number of 0.05 and in Figure 36 for chamber Mach number of 0.10. Using the measured values of the admittance parameter α and Figure 51, which is based on Equation (2-29), the nondimensional decay coefficients Λ_N for the Study 4 nozzles were calculated and the results are plotted in Figure 37. An examination of the measured values of α and Γ and the calculated values of Λ_N (i.e., Figures 35 through 37) leads to the following observations. At a given chamber Mach number all the three nozzle configurations provide approximately the same damping for axial instabilities in the low frequency range. For nondimensional frequencies S greater than approximately 1.0 the difference in the damping capabilities of the three nozzle configurations becomes apparent. For a given nozzle entrance Mach number the conical nozzle provides more damping than the equal-radii-of-curvature nozzle which provides more damping than the linear-velocity-profile nozzle.

Examination of the measured values of β and η indicates that the conical nozzle causes a larger phase shift at the nozzle entrance, between the incident and reflected pressure waves, than the equal-radii-of-curvature nozzle which produces a larger phase shift than the linear-velocity-profile nozzle. These differences in phase shift indicate that the conical nozzle "appears" to the oscillations in the chamber as being "longer" than the equal-radii-of-curvature and linear-velocity-profile nozzles.

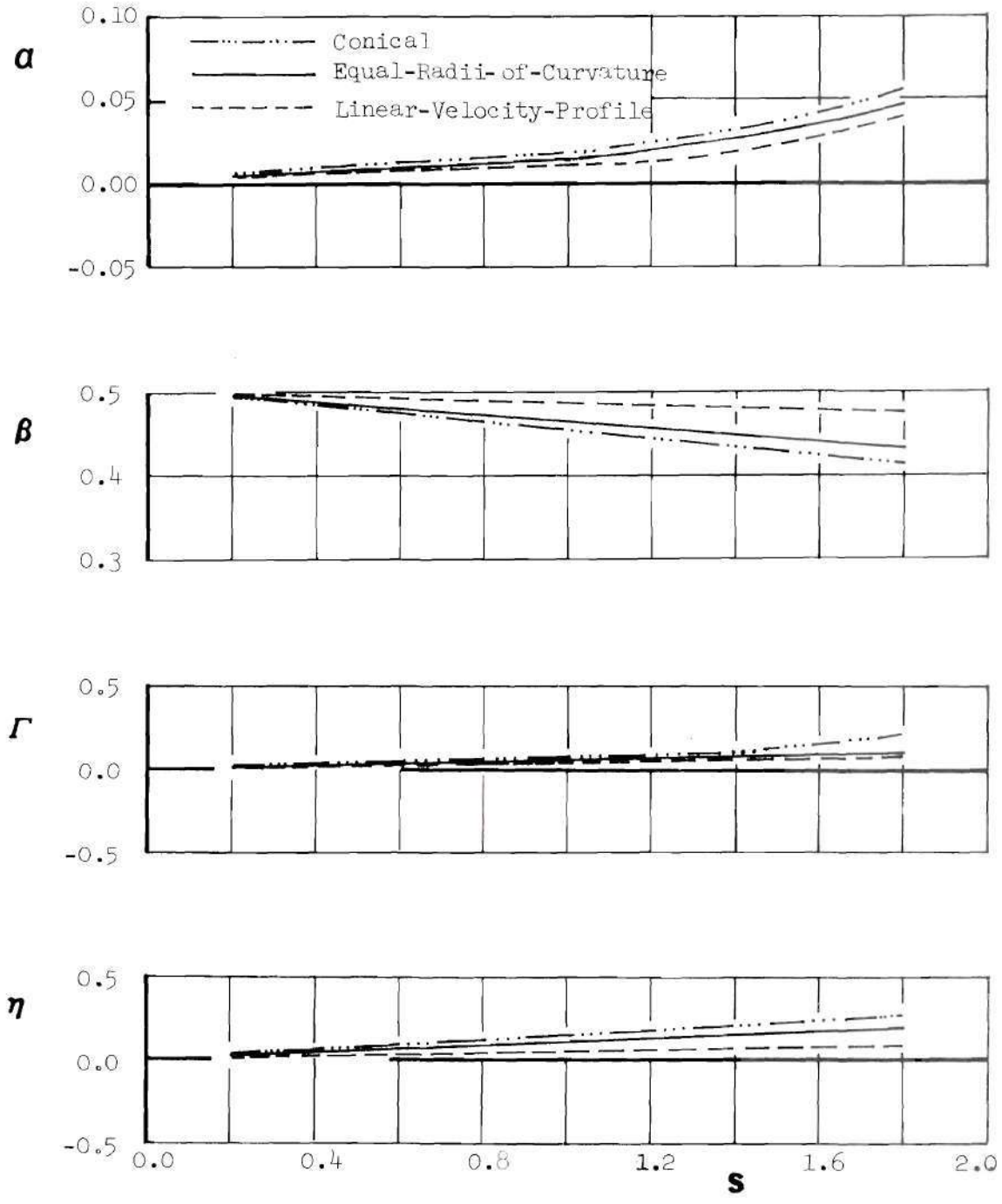

Figure 35. Comparison of the Admittance Data of Study 4 Nozzles ($\bar{M}$ = 0.05)

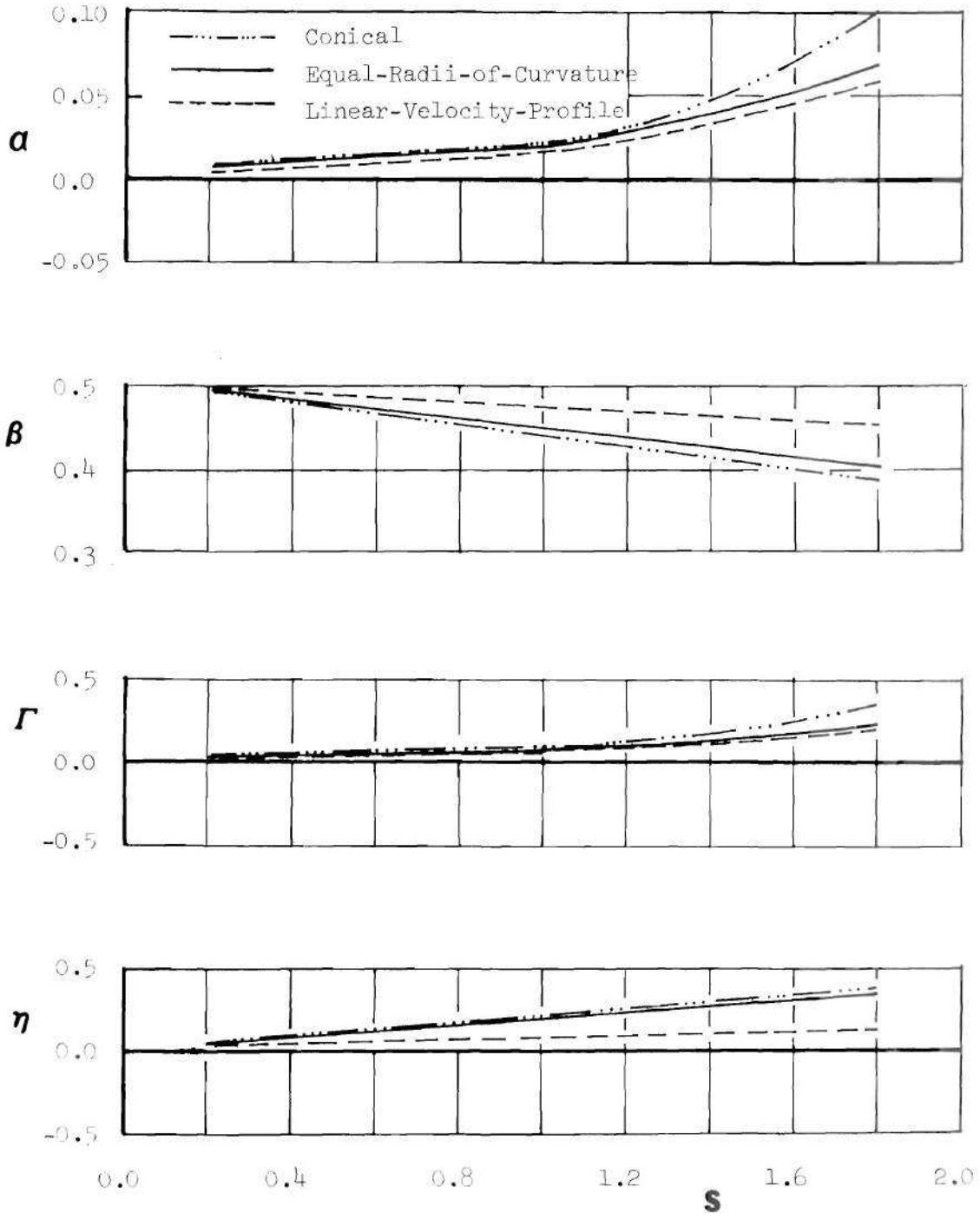

Figure 36. Comparison of the Admittance Data of Study 4 Nozzles ($\bar{M}$ = 0.10)

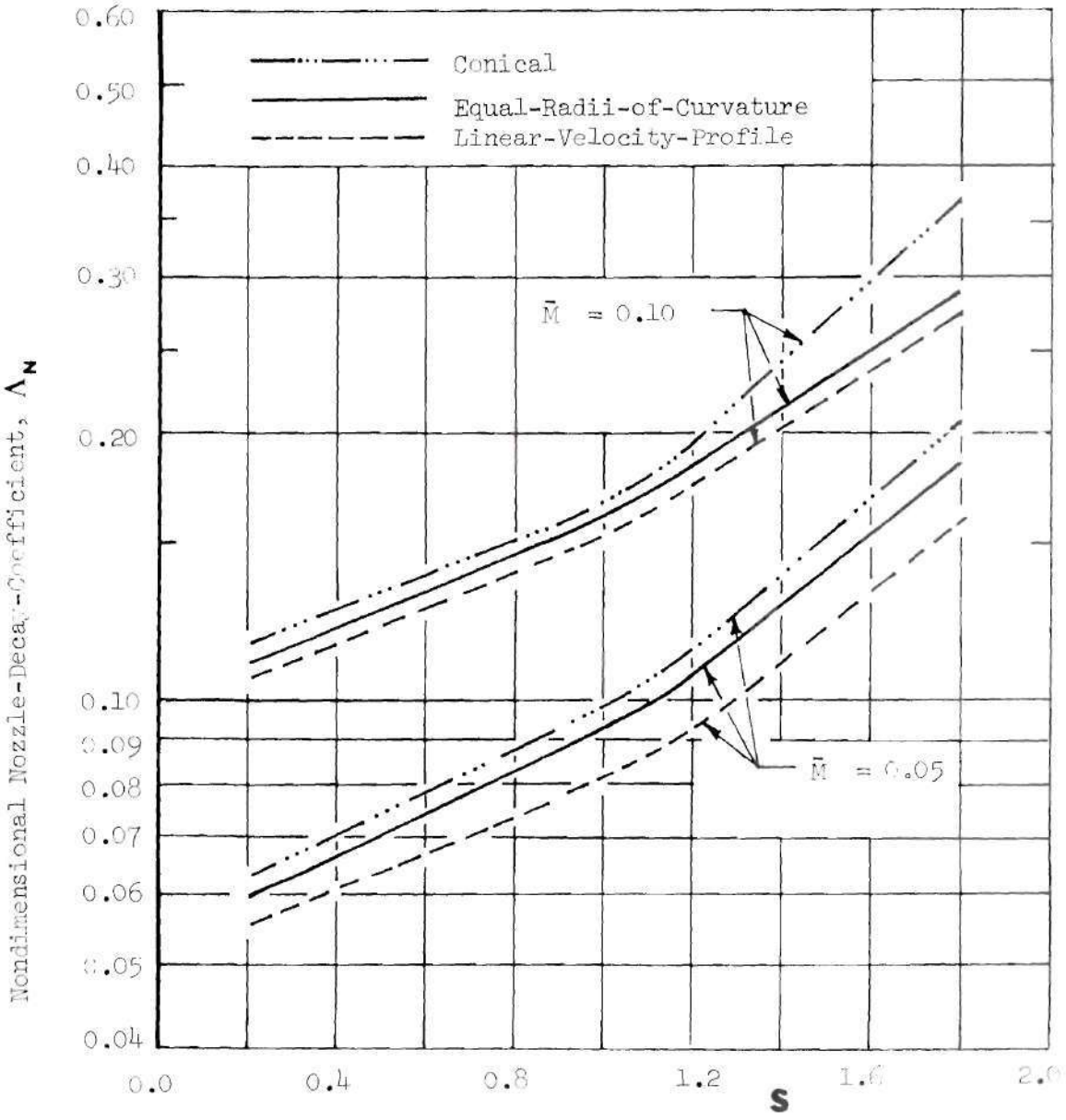

Figure 37. Frequency Dependence of the Nozzle-Decay-Coefficient of Study 4 Nozzles.

It is to be noted that the nozzle admittance data measured in this study are frequency dependent, which is contrary to the predictions of the short nozzle theory. As mentioned earlier, during the discussion of the Study 1 data, this conclusion is related to the assumption requiring that the length of the convergent section of the nozzle be much shorter than the wavelength of the oscillation. In the case of all the nozzles tested in this task, the length L_N of the convergent section is 3.57 inches; and, therefore, at higher frequencies the basic assumption of the short nozzle theory is no longer satisfied.

A further examination of Figure 37 indicates that the behavior of $\log \Lambda_N$ exhibits two distinct trends depending upon the value of the non-dimensional frequency S; the transition between these trends occurs at a value of S between 1.0 and 1.2. When S equals 1.0 the wavelength of the oscillation in the impedance tube approximately equals to 36 inches. By taking the ratio of the length of the convergent section of the nozzles tested in this task to the above value of λ, one obtains

$$\frac{L_N}{\lambda} \approx 0.1 \qquad (4\text{-}11)$$

In light of the above discussion and from an examination of the data presented in Figures 35 through 37 it appears that the admittances of nozzles tested in this task are practically independent of the frequency when the condition $L_N/\lambda < 0.1$ is satisfied. The frequency dependence of the admittance data becomes prominent when $L_N/\lambda > 0.1$.

In order to assess the effect of the Mach number on the damping capabilities of the nozzles tested in this task, the admittance data for

the conical nozzle, presented in Figures 29 and 30 were replotted in Figure 38. An examination of this figure indicates that increasing the Mach number from 0.05 to 0.10 has little effect on the values of the α and Γ for all values of S less than approximately 1.0 (or $L_N/\lambda < 0.1$). For values of S greater than 1.0 (or $L_N/\lambda > 0.1$), an increase in the Mach number from .05 to 0.1 results in a small increase in values of α and Γ. The above observations regarding the effect of increasing the mean flow Mach number on the damping of the conical nozzle also apply to the equal-radii-of-curvature and the linear-velocity-profile nozzles. These results seem to indicate that the admittances of solid rocket nozzles may be practically independent of the mean flow Mach number for values of $L_N/\lambda < 0.1$. On the other hand the magnitudes of α and Γ slightly increase with increase in Mach number for all values of $L_N/\lambda > 0.1$.

To facilitate the use of the measured Study 4 data in the design of solid rockets, rational functions were used to derive empirical relationships that describe the frequency dependence of the nondimensional decay coefficient Λ_N. The derived empirical expressions are presented in Table 4. The error associated with these relations, when compared with the data of Figure 37, is between 2 to 5 percent.

Next, the results obtained in this study will be compared with trends predicted in a related theoretical study. In the GEMSIP program,[26] Crocco's nozzle admittance theory was used to predict the stability of several identical combustors attached to nozzles with different geometries. The GEMSIP study also investigated the acoustic energy losses associated with conical, equal-radii-of-curvature, and linear-velocity-profile nozzles. This data will now be compared with the

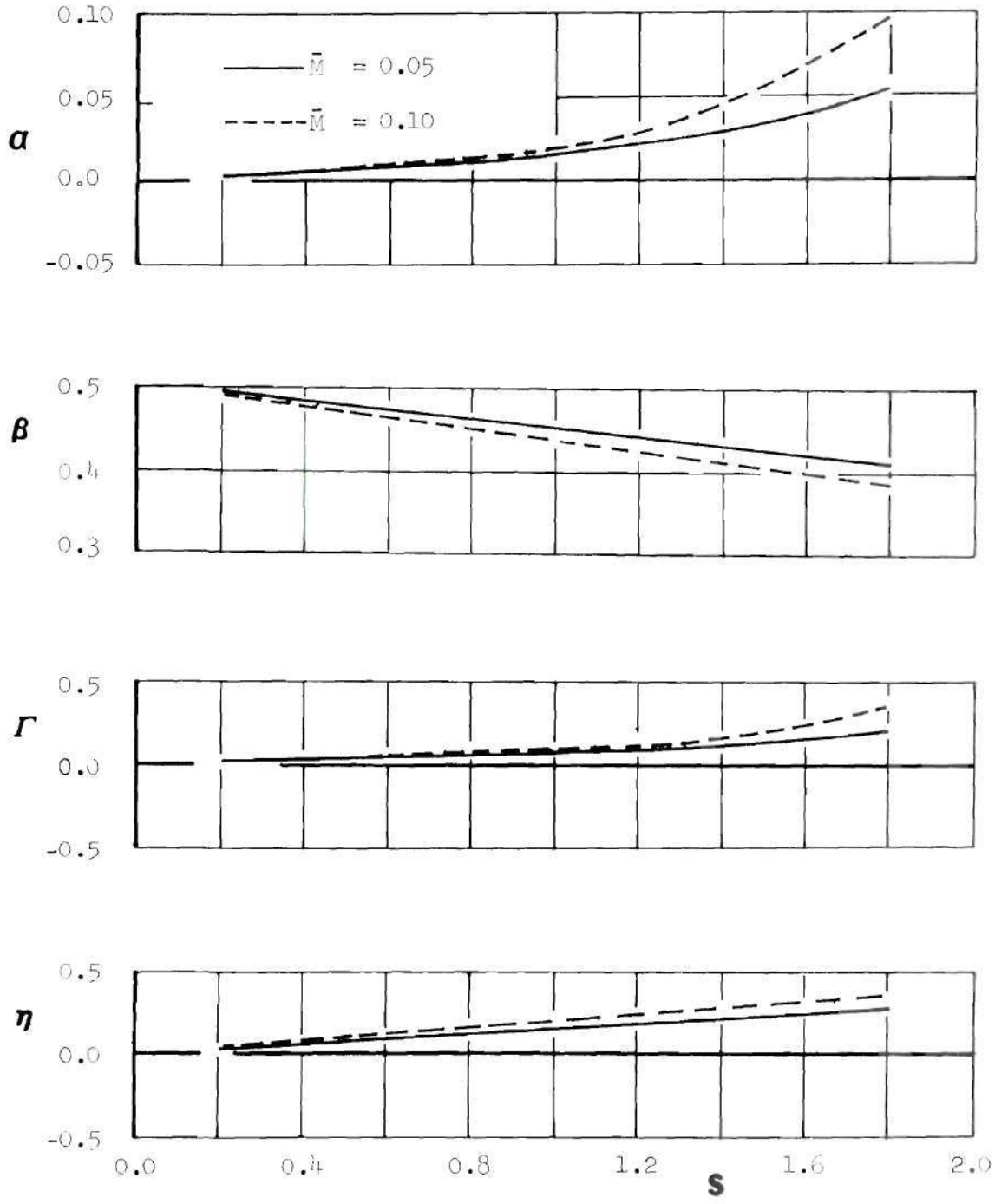

Figure 38. Effect of Mach Number on the Admittance Data of the Conical Nozzle.

Table 4. Study 4: Empirical Relations for Λ_N

Nozzle	Λ_N	
	$\bar{M} = 0.05$	$\bar{M} = 0.10$
Linear-Velocity-Profile	$-\frac{5.1}{100 - 38S}$	$-\frac{9.6 + 1.5S}{100 - 30S}$
Equal-Radii-of-Curvature	$-\frac{5.4 + 0.6S}{100 - 38S}$	$\frac{10 + 1.2S}{100 - 32S}$
Conical	$-\frac{5.8 + 0.58S}{100 - 37S}$	$-\frac{11 - S}{100 - 42S}$

experimental data measured in this investigation. The entrance diameters of the nozzles investigated in Reference 26 were equal to the combustor diameter and the lengths of their convergent sections were all equal to 7.5 inches. Using the scaling rules presented in Chapter II and considering the nozzles studied in the GEMSIP program as "reference" nozzles (for which z_{ref} = 7.5 inches), the theoretical admittances of the conical, equal-radii-of-curvature, and linear-velocity-profile nozzles (for which z_f = 3.57 inches) tested in Study 4 were obtained by considering them as "contracted" versions of the "reference" nozzles. The GEMSIP admittance data along with the admittance data for the "contracted" nozzles are presented in Figure 39. Though the lengths of the convergent sections of the "contracted" nozzles are now the same as those of the nozzles of Study 4, it should be borne in mind that the nozzles tested in Study 4 did not connect smoothly with the impedance tube; as shown in Figure 14 there was a step between the impedance tube and the nozzle entrance. The presence of such a step was not considered in the computations of Reference 26. An examination of the data presented in Figures 35, 36 and 39 indicates that the test frequency range of the Study 4 nozzles and the frequency range of interest in Reference 26 do not completely overlap each other. It can be observed that where these two frequency ranges overlap there is a qualitative agreement between the observed and predicted trends in the imaginary part of the nondimensional admittance η. However, no such agreement is indicated in the trends of the real part of the nondimensional admittance Γ. Unfortunately, due to the limited extent of frequency overlap, it is not possible at this time to generalize the above statement to the entire frequency range covered in Figure 39.

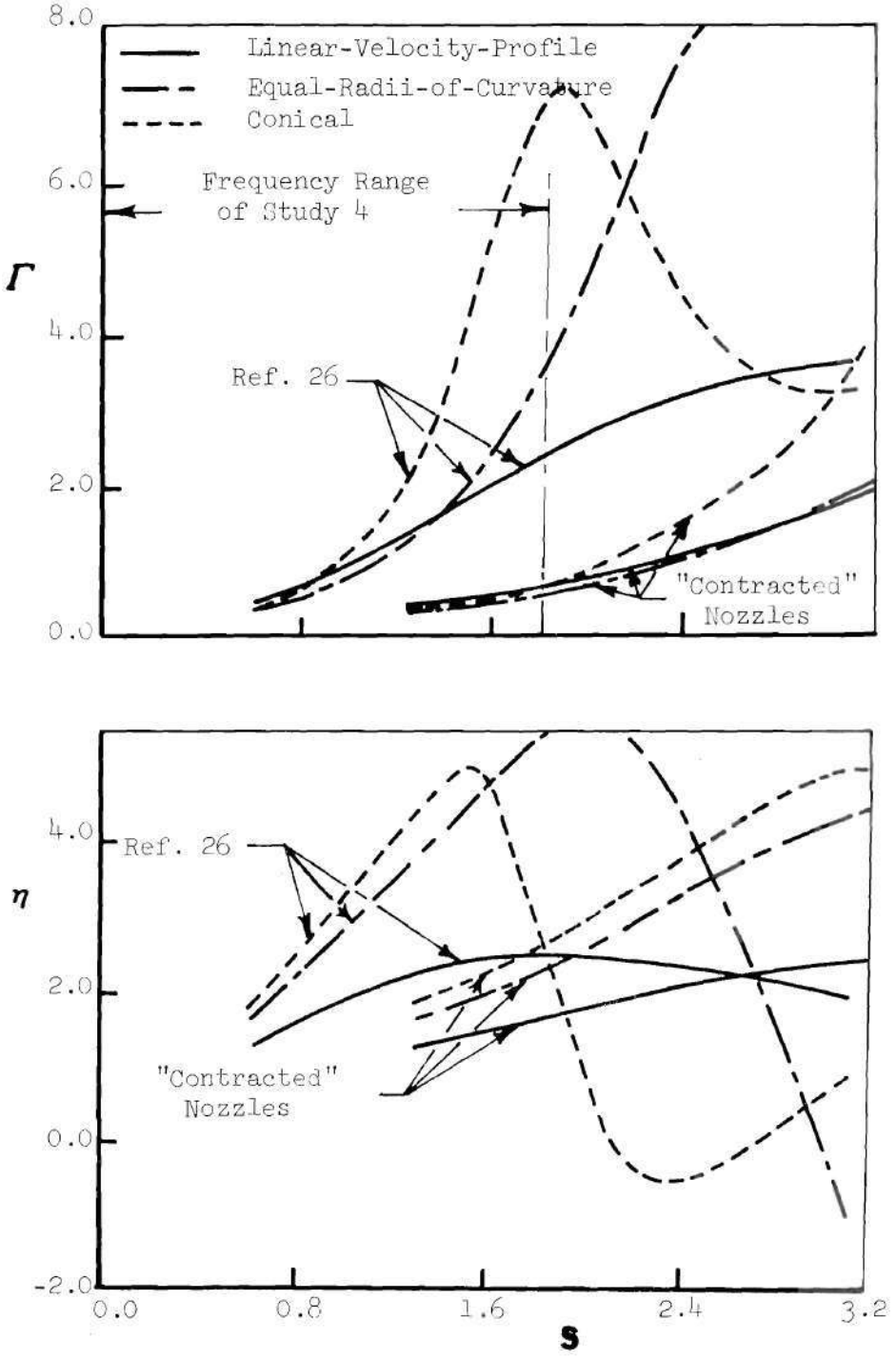

Figure 39. GEMSIP Admittance Data.

The main conclusion of this study is that the conical nozzle provides more damping than the equal-radii-of-curvature nozzle which in turn provides more damping than the linear-velocity-profile nozzle. Based on this conclusion it appears that for a given solid rocket nozzle with fixed values of entrance diameter, throat diameter and length of the convergent section the damping capability of the nozzle can be increased by suitably redesigning the geometry of its convergent section. Finally, it appears that the admittances of solid rocket nozzles are "weakly" dependent upon the frequency and chamber Mach number for values of $L_N/\lambda < 0.1$ and they both increase with frequency and Mach number for larger values of the above-mentioned ratio.

Study 5: Damping Capabilities of Multiple-Nozzle Clusters

This study was undertaken to investigate the dependence of damping provided by multiple-nozzle clusters upon the number of nozzles present in the nozzle cluster. For this purpose tests were conducted using single-, dual-, and quadruple-nozzle configurations. The nozzles tested in this study are described in Chapter III. All the tested nozzle configurations were designed to maintain equal cross-sectional area distributions which in turn ensure similar velocity distributions in their convergent sections. In addition, the convergent sections of all of the tested nozzle configurations are of equal length. These nozzles were tested with a chamber Mach number of 0.06.

The admittance data were obtained from pressure amplitude measurements and the data are presented in Figures 40 through 42. The data pertaining to each of the nozzles include the frequency dependence of the measured admittance parameters α and β as well as the values of the

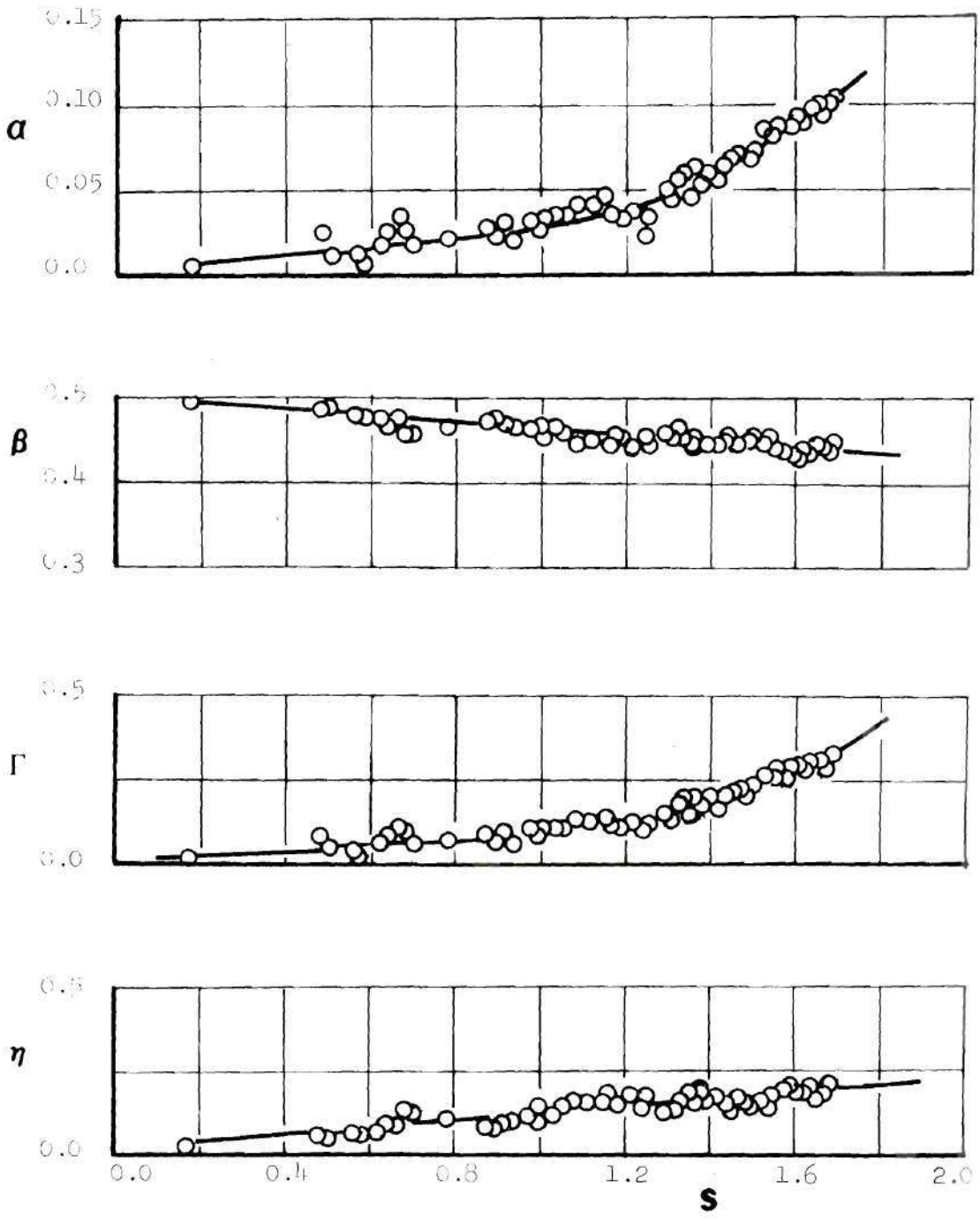

Figure 40. Frequency Dependence of the Admittance Data of the Single-Orifice Nozzle.

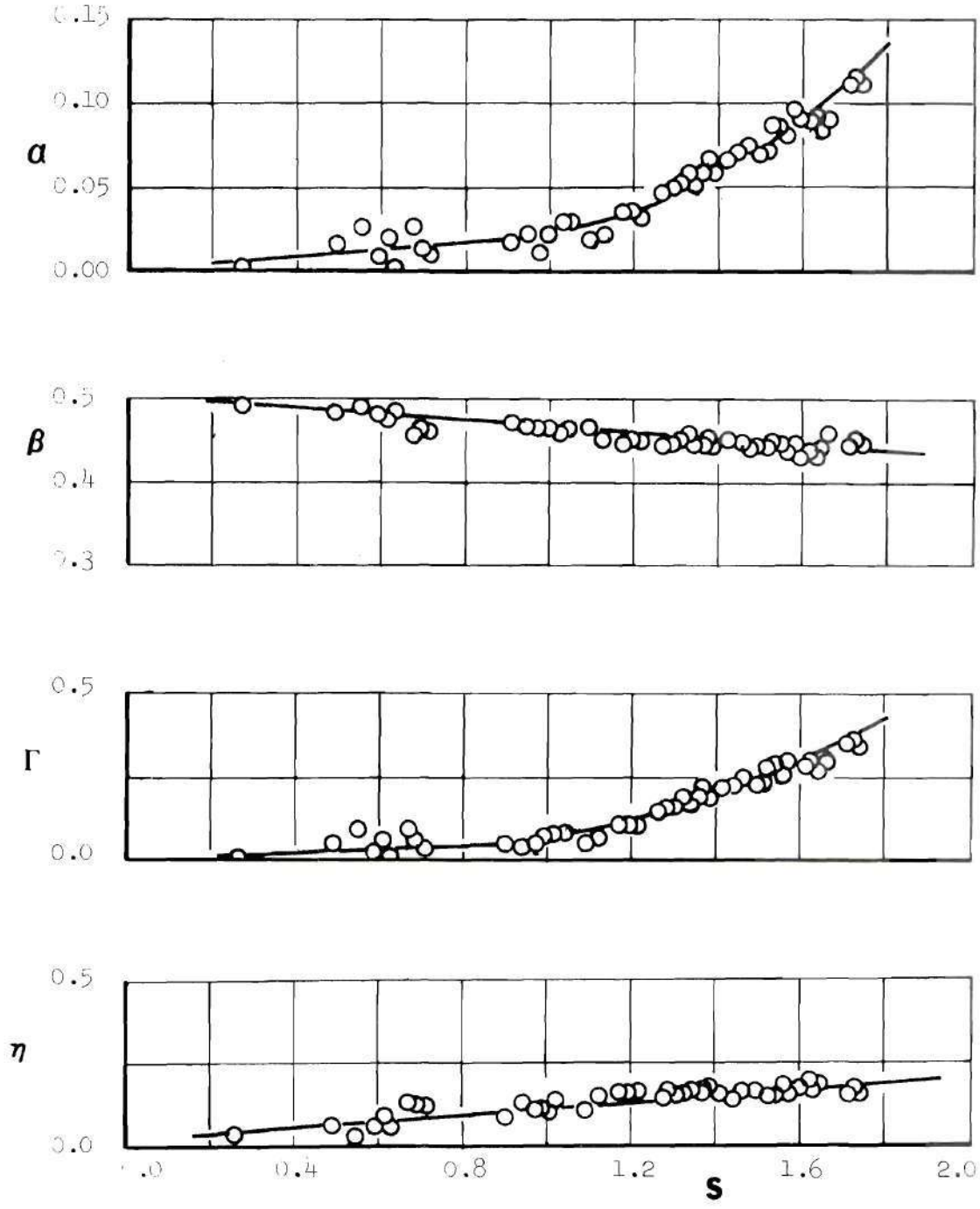

Figure 41. Frequency Dependence of the Admittance Data of the Dual-Orifice Nozzle.

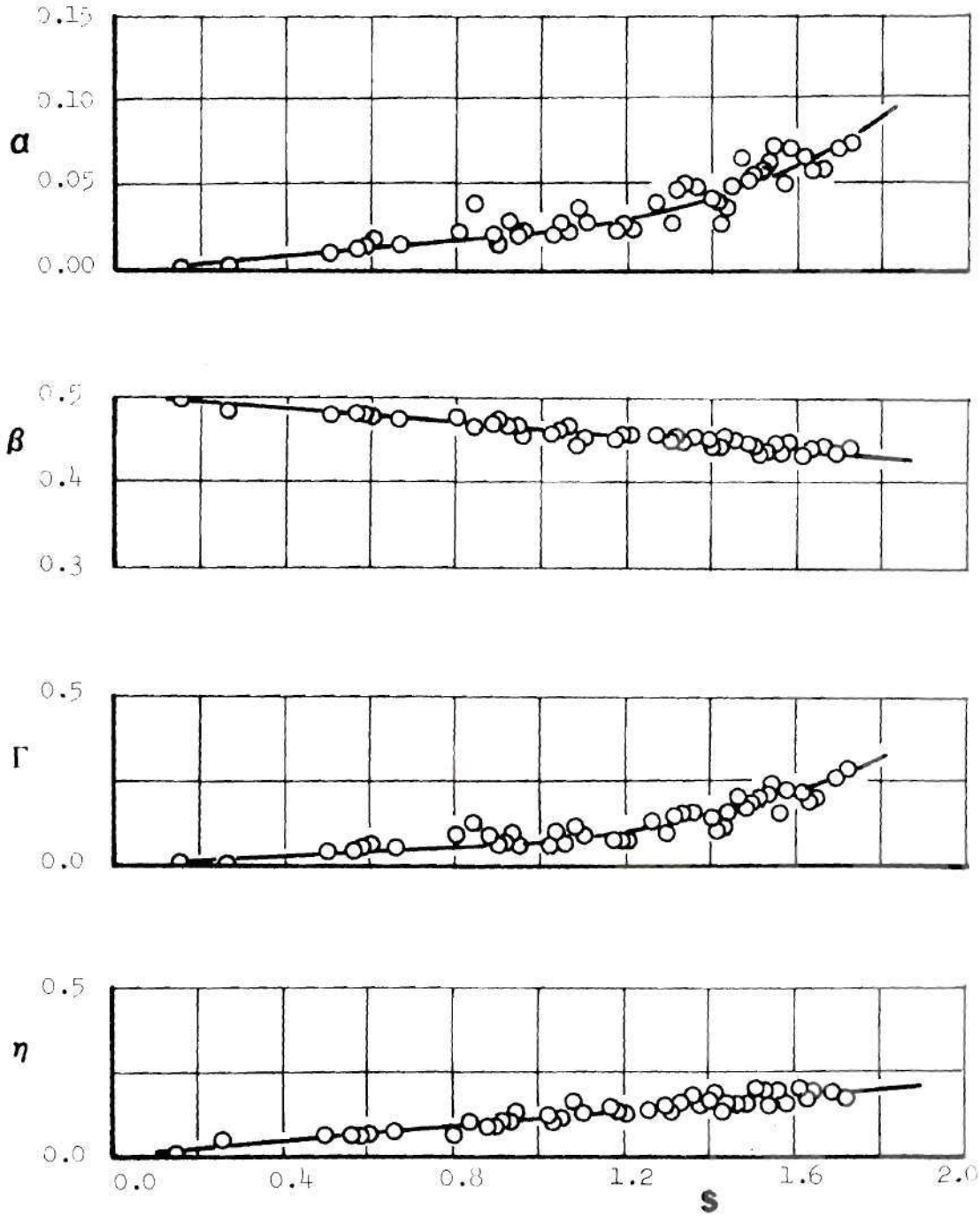

Figure 42. Frequency Dependence of the Admittance Data of the Quadruple-Orifice Nozzle.

real and imaginary parts of the nondimensional admittance y_N.

To evaluate the relative damping capabilities of these three nozzles, the data presented in Figures 40 through 42 is compared in Figure 43. Employing the measured values of the admittance parameter α and Figure 51 of the Appendix B the nondimensional decay coefficients of the Study 5 nozzles were also calculated and the results are presented in Figure 44. An examination of the measured values of α and Γ and the calculated values of Λ_N indicates that the quadruple-ported nozzle provides less damping for axial instabilities than the single- and dual-ported nozzles. The difference in the damping capabilities of these three nozzle configurations is particularly apparent at nondimensional frequencies, S, larger than 1.0. It is also noted from these figures that the single- and dual-ported nozzles provide approximately the same damping. Examination of the measured values of β and η indicates that all of the three nozzle configurations result in approximately the same phase shift, at the nozzle entrance, between the incident and reflected pressure waves.

It should also be pointed out that, similar to the observations of Study 4, the nozzle admittance data measured in this task are also frequency dependent. The lengths of the convergent sections of the nozzles tested in Study 5 are all the same and they equal 4.63 inches. Using this length, it can be shown that at high frequencies the basic assumption of the short nozzle theory (i.e., $L_N/\lambda << 1$) is no longer satisfied. Further examination of Figure 44 indicates that the nature of the frequency dependence of the admittance data of the Study 5 nozzles changes at a value of S between 0.9 and 1.2. This value of S corresponds

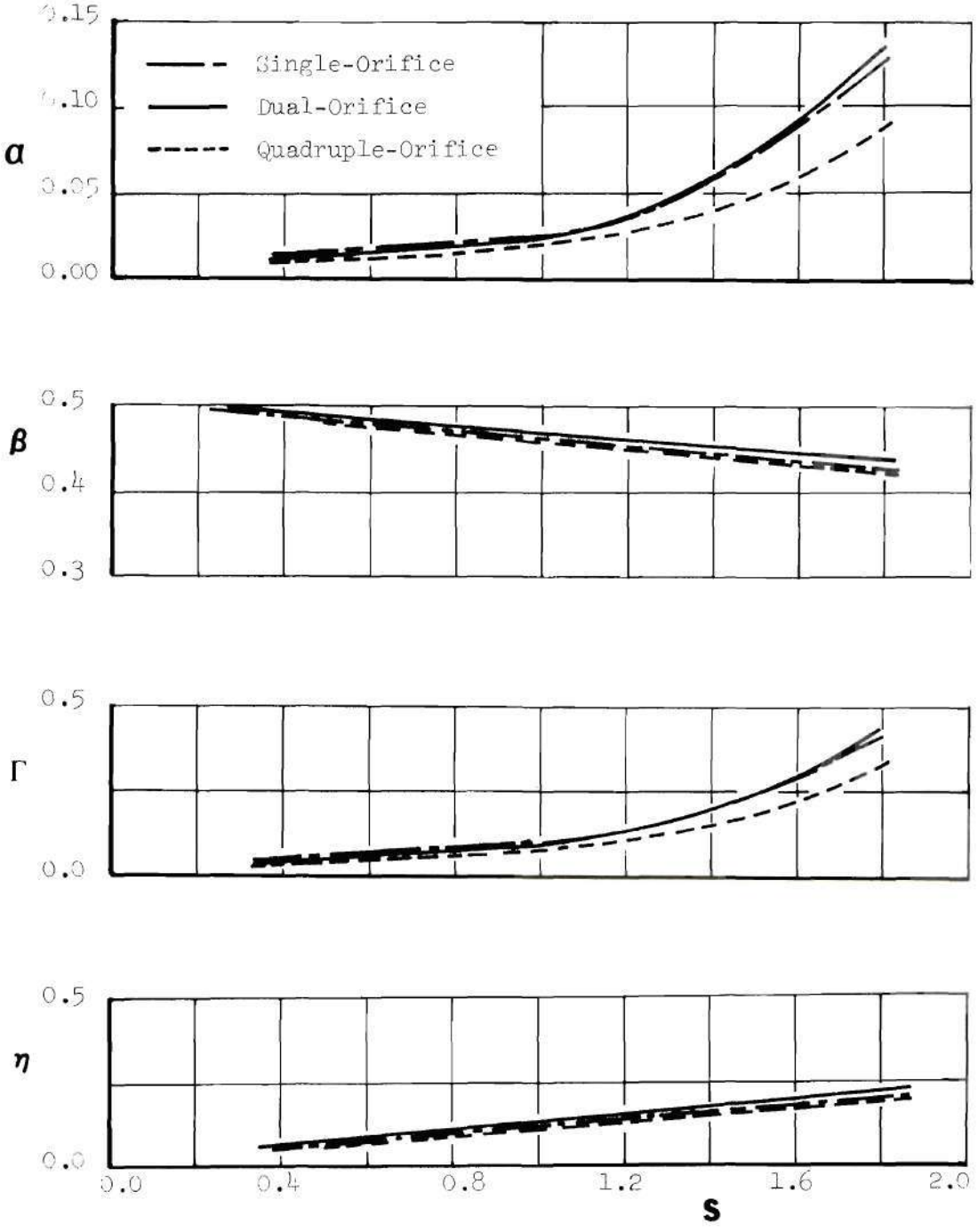

Figure 43. Comparison of the Admittance Data of Study 5 Nozzles.

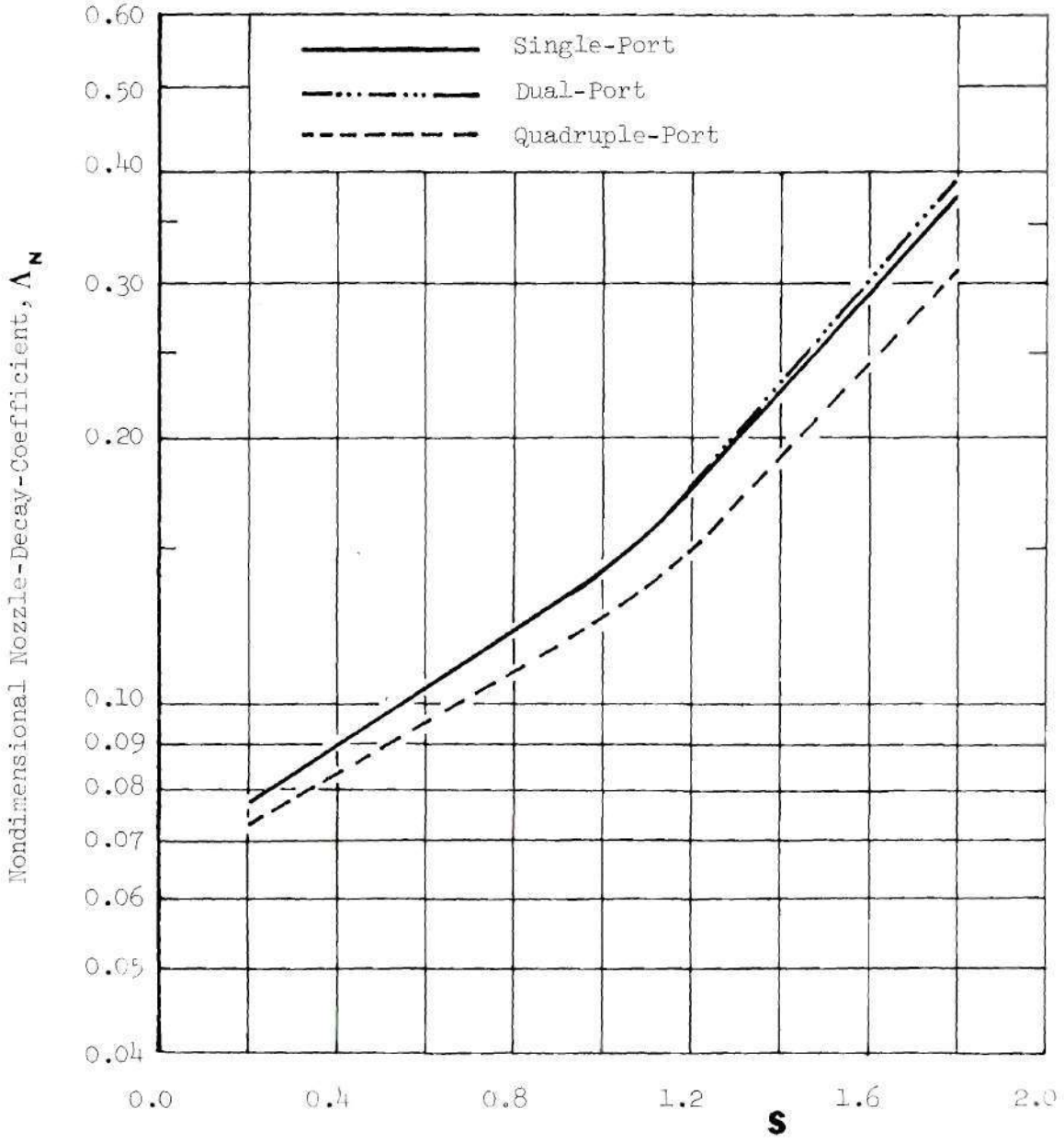

Figure 44. Frequency Dependence of Multiple-Nozzle Cluster Decay-Coefficients.

to a wavelength satisfying the condition $L_N/\lambda \approx 0.1$. As was found in the analysis of the Study 4 data, an analysis of the Study 5 admittance data indicates that the measured admittances are "weakly" dependent on the frequency for all values of $L_N/\lambda < 0.1$ and they become dependent for larger values of this ratio.

As was done in Study 4, rational functions were used to derive empirical relations that describe the frequency dependence of the non-dimensional decay coefficient Λ_N of the Study 5 nozzles. These empirical relations are presented in Table 5.

The main conclusion of this study is that the quadruple-ported nozzle provides less damping for axial instabilities than the single- and dual-ported nozzles whose damping capabilities are approximately the same.

Table 5. Study 5: Empirical Relations for Λ_N

$\overline{M} = 0.06$

Nozzle	Λ_N
Single-Port	$-\frac{6.5 + 2.6S}{100 - 39S}$
Dual-Port	$-\frac{6.55 + 2.65S}{100 - 39S}$
Quadruple-Port	$-\frac{6.3 + 1.5S}{100 - 39S}$

CHAPTER V

SUMMARY OF RESULTS AND CONCLUSIONS

Results and Conclusions

In summary, the following results and conclusions emerge from the studies conducted during this investigation.

(1) The values of the admittance parameter α, that is a measure of the attenuation provided by the test nozzles, are small and practically independent of the frequency for both the RN-I and RN-II nozzles. Hence both of these nozzles provide little damping for axial instabilities when used in actual rocket engines.

(2) The damping provided by short nozzles (including RN-I and RN-II, whose geometries satisfy the short nozzle criteria) is practically independent of the frequency and geometrical details of the nozzle contours. The measured admittance data indicate that when short nozzles are attached to cylindrical combustors, the resulting nondimensional Nozzle Decay Coefficients Λ_N approximately equal J, the ratio of the nozzle throat area to chamber cross sectional area; this approximate result is in agreement with the empirical conclusion of Buffum et al.[9,10] However, a comparison of the experimental short nozzle data with predictions based on the short nozzle theory indicates that the theory underestimates the damping capabilities of short nozzles.

(3) In general, for a given solid rocket nozzle with fixed values of entrance diameter, throat diameter and length of the convergent section, the nozzle damping can be increased by suitably redesigning the geometry

of its convergent section. Tests conducted with three different nozzle configurations showed that a conical nozzle provides more damping than an equal-radii-of-curvature nozzle which in turn provides more damping than a linear-velocity-profile nozzle.

(4) The real and imaginary parts of the nondimensional admittances of solid rocket nozzles are weakly dependent upon the frequency and chamber Mach number for all values of $L_N/\lambda < 0.1$ and they both increase with frequency and Mach number for larger values of the above-mentioned ratio.

(5) The damping provided by multiple-ported solid rocket nozzles depends upon the number of nozzles present in the nozzle cluster. Results obtained under this program showed that the quadruple-ported nozzle provides less damping for axial instabilities than the single- and dual-ported nozzles whose damping capabilities are approximately the same.

(6) During axial instabilities in a rocket engine with a submerged exhaust nozzle there is wave motion in both the combustor and the cavity surrounding the submerged nozzle. The depth of the cavity surrounding the submerged nozzle has a significant effect upon the measured admittance data. However, the cavity depth has negligible effect upon the computed value of the Nozzle Decay Coefficient. The secondary flow rates issuing from the nozzle cavity have practically no effect upon the nozzle admittance, but they do affect the nozzle decay coefficient.

(7) Careful judgment should be exercised when using the magnitude of the real part of the nozzle admittance to evaluate nozzle damping. The real part of the nozzle admittance becomes large whenever the nozzle entrance is located in the vicinity of a pressure node. The quantity

that should be used in the evaluation of nozzle damping is the product of the real part of the nozzle admittance and the square of the pressure amplitude at the nozzle entrance plane. One should also remember that both radiation and mean flow effects should be accounted for in the evaluation of nozzle damping.

(8) Relevant nozzle damping data for both "short" and "long" full-scale rocket nozzles can be determined experimentally by investigating the damping provided by geometrically-similar small-scale nozzles.

Recommendations for Future Work

Several recommendations can be made on the basis of the results of this investigation.

1. In order to assure that the nozzle admittance data measured under cold-flow conditions can be scaled to actual "hot" engine operating conditions, some of the tests conducted in this program should be repeated at elevated temperatures.

2. Nozzle damping is expected to depend upon both the geometry of the nozzle convergent section and the manner in which the nozzle attaches to the combustor. The effect of nozzle geometry has been investigated in this program while the effect of the manner in which the nozzle attaches to the combustor is yet to be investigated.

3. The nozzle admittance data measured in this program were obtained in driven impedance tube experiments where the amplitude of the chamber oscillations remained constant throughout a given test. These admittance data were then used to analytically determine the Nozzle Decay Coefficients. This procedure implicitly assumes that the nozzle admittance data measured under constant amplitude conditions are also

applicable to situations in which the amplitude of the oscillation decays with time. This assumption needs to be checked experimentally.

4. The nozzle employed in the submerged nozzle investigation of Study 3 is a short nozzle providing little damping for axial instabilities. In order to determine the dependence of the admittance of a submerged "long" solid rocket nozzle upon the depth of the cavity surrounding the nozzle and the secondary flow rate issuing from the cavity some of the tests conducted in Study 3 should be repeated with nozzles similar to those used in Study 4.

APPENDIX A

THE DEPENDENCE OF THE MODIFIED IMPEDANCE TUBE WAVE STRUCTURE UPON THE NOZZLE ADMITTANCE

This appendix will investigate the effect of the nozzle admittance parameters α and β upon the standing wave pattern inside the modified impedance tube. This study was motivated by the desire to optimize the accuracy of the admittance data obtained from either amplitude or phase measurements taken at discrete locations along the modified impedance tube. To obtain the desired information, the dependence of the amplitude and phase distributions, along the impedance tube, upon the nozzle admittance parameters α and β will be investigated analytically. This data will be then used to discuss the accuracy of the measurement technique used in this study.

For a one-dimensional oscillation in a simulated combustor, the behavior of the pressure wave is given by the following expression

$$p_1(z,t) = |P_1(z)| \; e^{i\{\delta(z) + \omega t\}} \qquad \text{(A-1)}$$

where the pressure amplitude $|P_1(z)|$ and phase $\delta(z)$ are given by Equations (2-13) and (2-14), respectively. An examination of Equations (2-13) and (2-14) indicates that for a given frequency, the pressure amplitude and phase are functions of the axial coordinate z, the steady state properties of the medium and the admittance parameters α and β which describe the boundary condition at the nozzle entrance plane. For

a given set of values of $\bar{M}$, λ, α and β the axial dependence of the pressure amplitude and phase were computed and typical results are plotted in Figures 45 through 48. These figures describe the dependence of the pressure wave structure in a driven impedance tube upon the mean flow Mach number $\bar{M}$, the nozzle admittance parameters α and β, and the wavelength λ.

As mentioned earlier in Chapter II, Equations (2-13) and (2-14) indicate that, in principle, the admittance parameters α and β can be obtained from either pressure amplitude or phase measurements taken at three different axial locations along the modified impedance tube. A careful examination of the figures presented in this appendix indicates, however, that measurements taken at three discrete axial locations may not always yield enough information about the axial dependence of the pressure amplitude and phase of the standing wave. This point may be better illustrated by considering an experiment in which the admittance of a solid wall termination (for which $\alpha = 0.0$ and $\beta = 0.5$) is to be determined. The theoretical pressure amplitude distribution for this case and two additional cases, for which $\beta = 0.5$ and α equals 0.1 and 0.2, are plotted in Figure 49a. Examination of this figure shows that all three amplitude distributions almost coalesce in the vicinity of amplitude maxima but they substantially differ from one another near pressure minima. Thus, if the values of α and β were to be determined by the use of three transducers that are located near amplitude maxima, then it is most likely that small experimental errors will produce serious errors in the measured values of α. It seems intuitively clear that to minimize the possibility of errors in the measurement of α, one would want the three transducers to

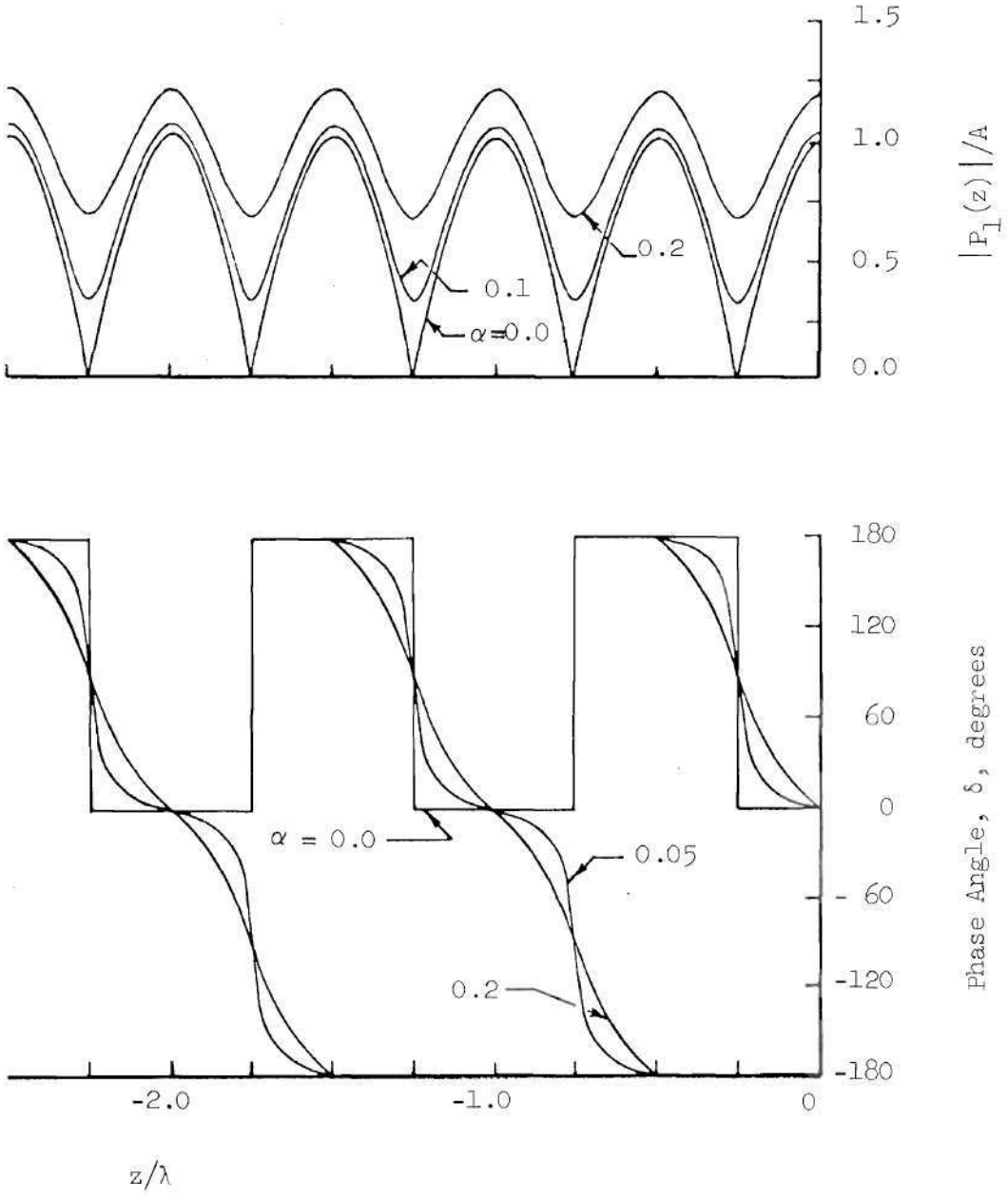

Figure 45. Standing Wave Pattern (with $\bar{M}$ = 0.0 and β = 0.5) in a Modified Impedance Tube.

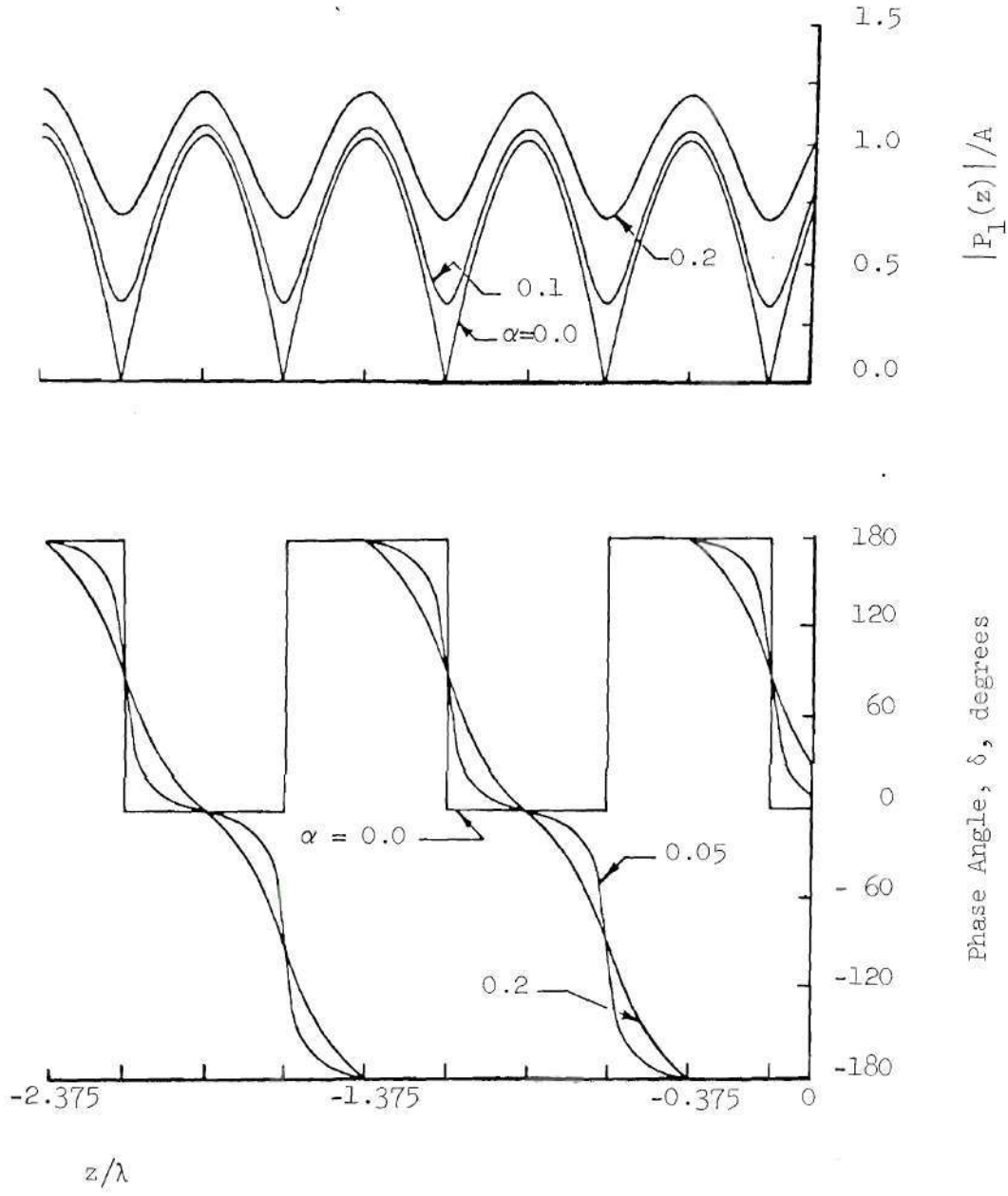

Figure 46. Standing Wave Pattern (with M = 0.0 and β = 0.25) in a Modified Impedance Tube.

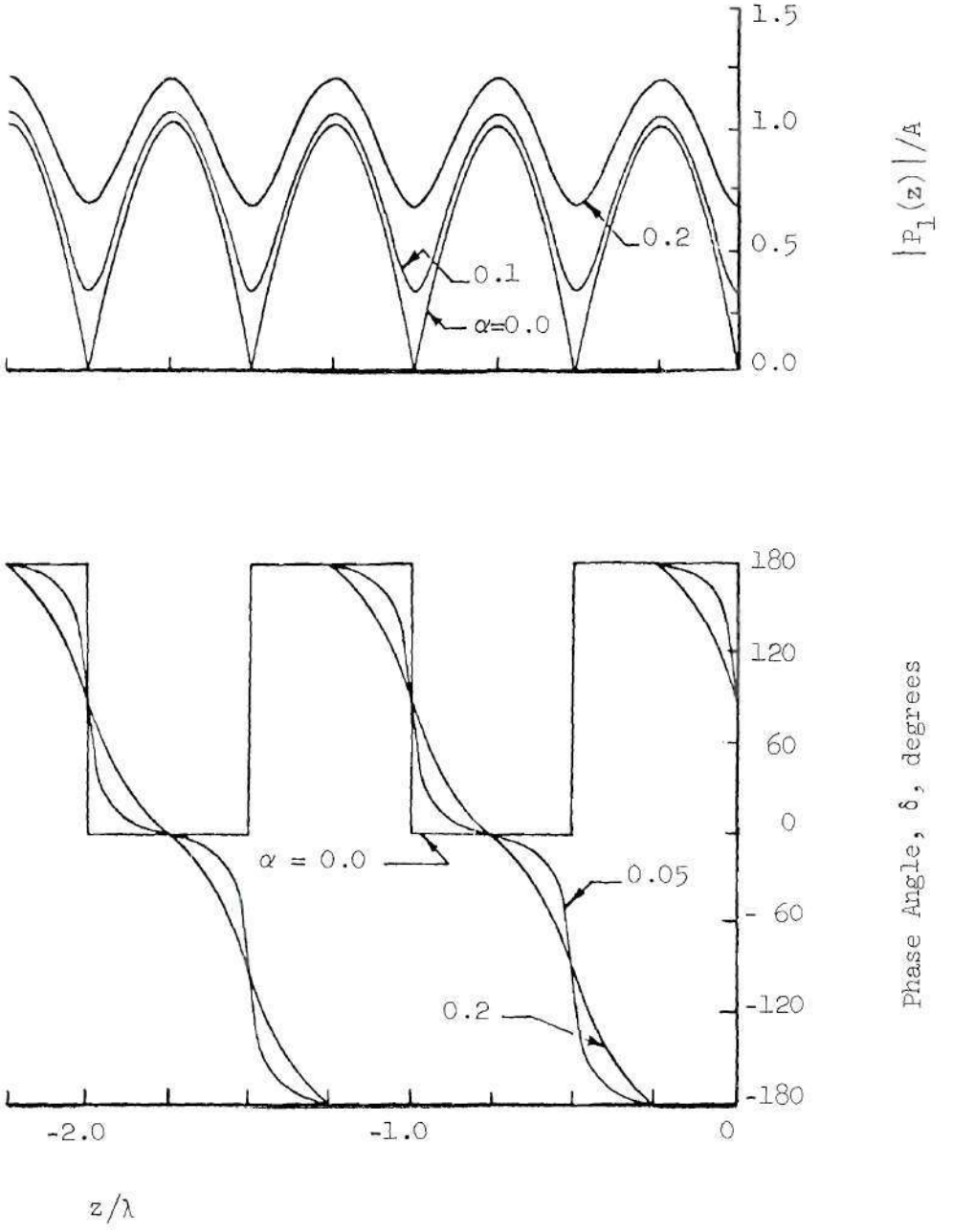

Figure 47. Standing Wave Pattern (with $\bar{M} = 0.0$ and $\beta = 0.0$) in a Modified Impedance Tube.

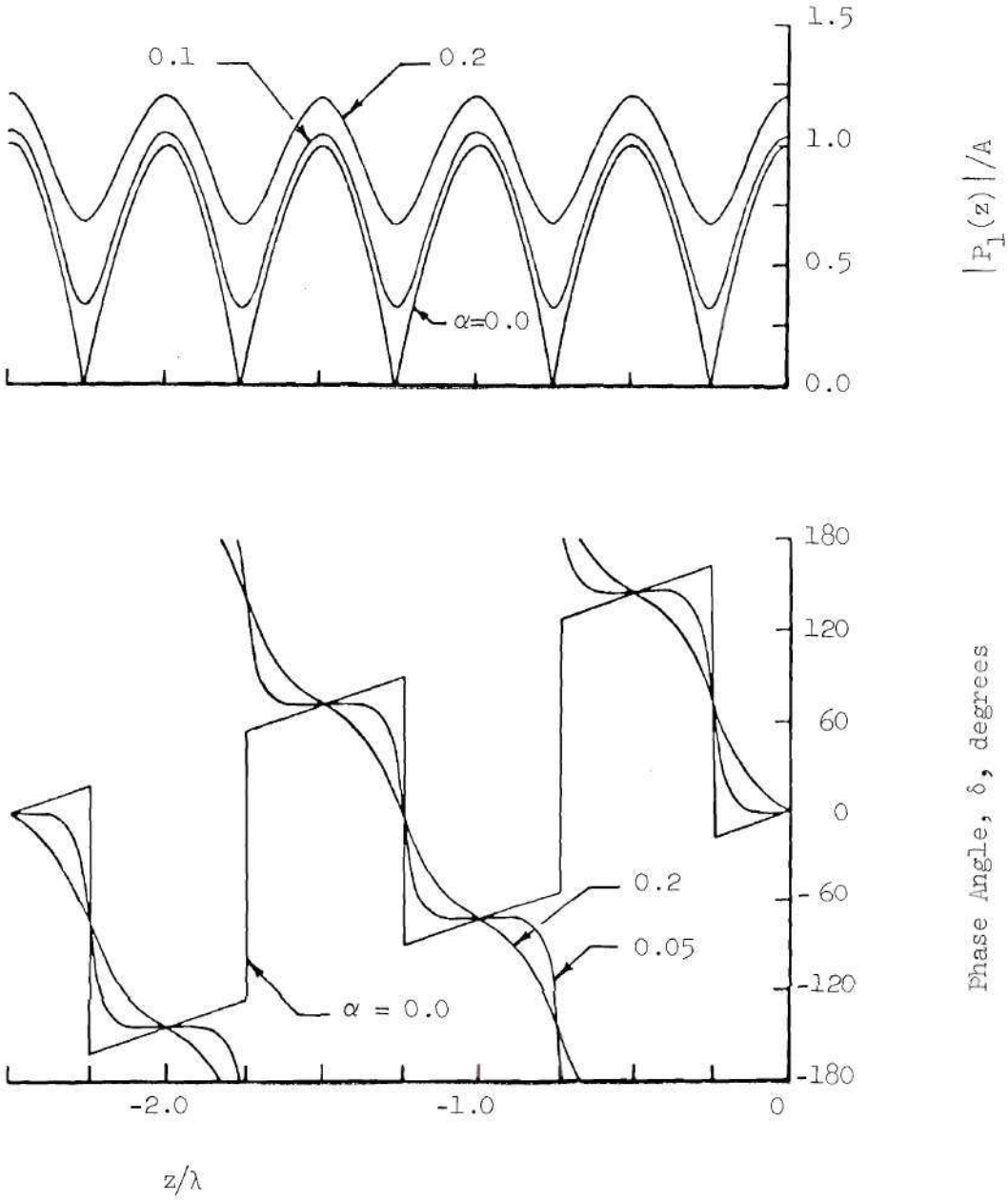

Figure 48. Standing Wave Pattern (with $\bar{M} = 0.2$ and $\beta = 0.5$) in a Modified Impedance Tube.

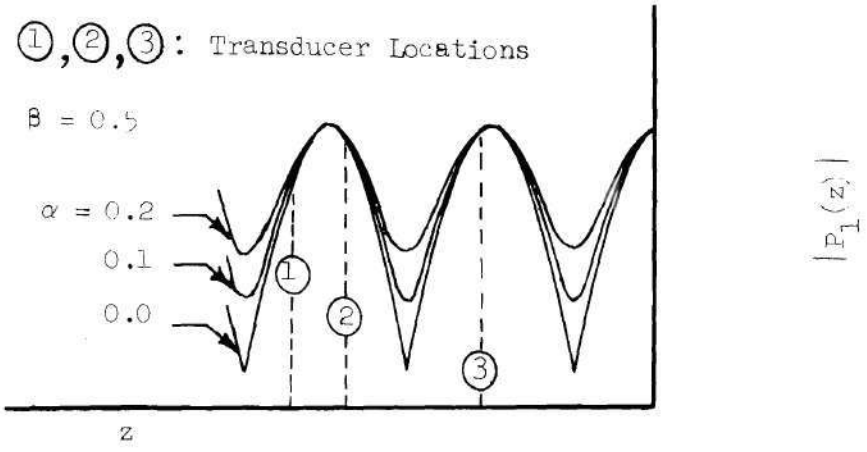

(a) Pressure Amplitude Measurement.

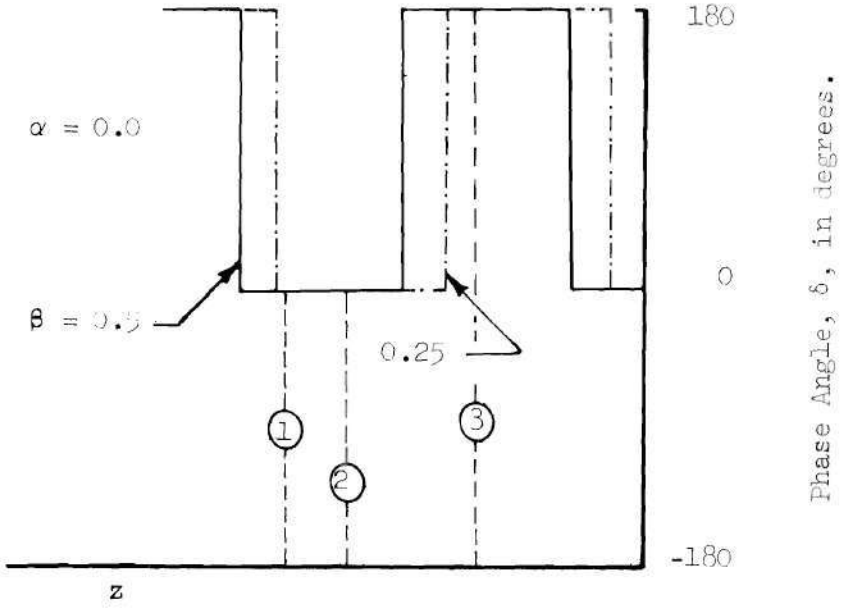

(b) Pressure Phase Measurement.

Figure 49. Standing Wave Measurement by Three Transducers.

be located near locations of both amplitude minimum and amplitude maximum. However, in a given experimental setup the structure of the pressure amplitude is not known and thus it is impossible to determine in advance the optimum locations for placing the transducers. To overcome this difficulty and to assure the quality of the measured data, more than three transducers need to be used.

The above discussion can be repeated for phase measurements. The only difference between the use of the phase and amplitude measurement techniques is that insufficient information about the phase distribution along the impedance tube would result in serious errors in the parameter β rather than the parameter α, as was the situation in the case of amplitude measurements. This point can be best illustrated by referring to Figure 49b where the phase distributions corresponding to two different values of β (i.e., $\beta = 0.5$ and $\beta = 0.25$) and the same value of α (i.e., $\alpha = 0.0$) are plotted. If the unknown admittances were to be determined by means of the three transducers shown in the figure, the correct value of β would most likely not be obtained. A further examination of the data presented in Figures 45 through 48 suggests that to minimize the possibility of errors in the measurement of α, phase measurements should be used. Also, the transducers must be located as close as possible to the amplitude nodal point. However, in an experimental setup the axial dependence of the pressure phase is not known in advance and these optimum locations depend upon the frequency of the oscillations. Hence, for the experimental arrangement used in this investigation, where the frequency of the driver output varied linearly between 40 to 600 Hertz, it was impossible to find optimum locations that will satisfy all the experimental conditions. As

was mentioned earlier, in the discussion of pressure amplitude measurements, this difficulty can be overcome by use of more than three transducers.

Finally, it should be pointed out that the expressions relating $|P_1(z)|$ and $\delta(z)$ to admittance parameters α and β are nonlinear and hence the use of pressure amplitude or pressure phase measurements taken at only three axial locations to determine α and β may not yield a unique solution. In view of the above discussion ten transducers placed at different locations along the modified impedance tube were used in this program to determine the behavior of the standing pressure wave pattern. Based on the experience gathered during this investigation, it is believed that the use of ten transducers is sufficient for the range of frequencies covered in this program.

APPENDIX B

NOZZLE DECAY COEFFICIENT FOR A CYLINDRICAL CHAMBER

This appendix will demonstrate how the measured small-scale nozzle admittances can be used to determine the decay (or growth) rate of a disturbance in the cold flow chamber. Since it will be assumed that the nozzle is only a means of adding or removing wave-energy into or out of the system, then the calculated decay (or growth) rate will be referred to as the Nozzle Decay Coefficient and it will be denoted by the symbol α_N.

The desired expression for α_N can be derived from the expressions derived in Reference 21 that use the mass, momentum and energy conservation laws to investigate the behavior of small-amplitude disturbances in cavities with mean flows. Specializing the expressions derived in Reference 21 to the system shown in Figure 50 leads to the derivation of Equations (2-20) through (2-23). For a one-dimensional oscillation, when the nozzle is the only means of wave energy transfer into or out of the combustor, Equation (2-20) reduces to the following form:

$$2\alpha_N \hat{V} = - < A_c \left\{ p_1 u_1 \left[1 + \left(\frac{\bar{u}}{\bar{c}} \right)^2 \right] + p_1^2 \left(\frac{\bar{u}}{\gamma \bar{p}} \right) + u_1^2 \left(\frac{\overline{\gamma p u}}{\bar{c}^2} \right) \right\} > \qquad \text{(B-1)}$$

All the quantities appearing in Equation (B-1) are evaluated at the nozzle entrance. The right hand side of Equation (B-1) contains four terms. The first term is a measure of the radiative wave energy loss due to the

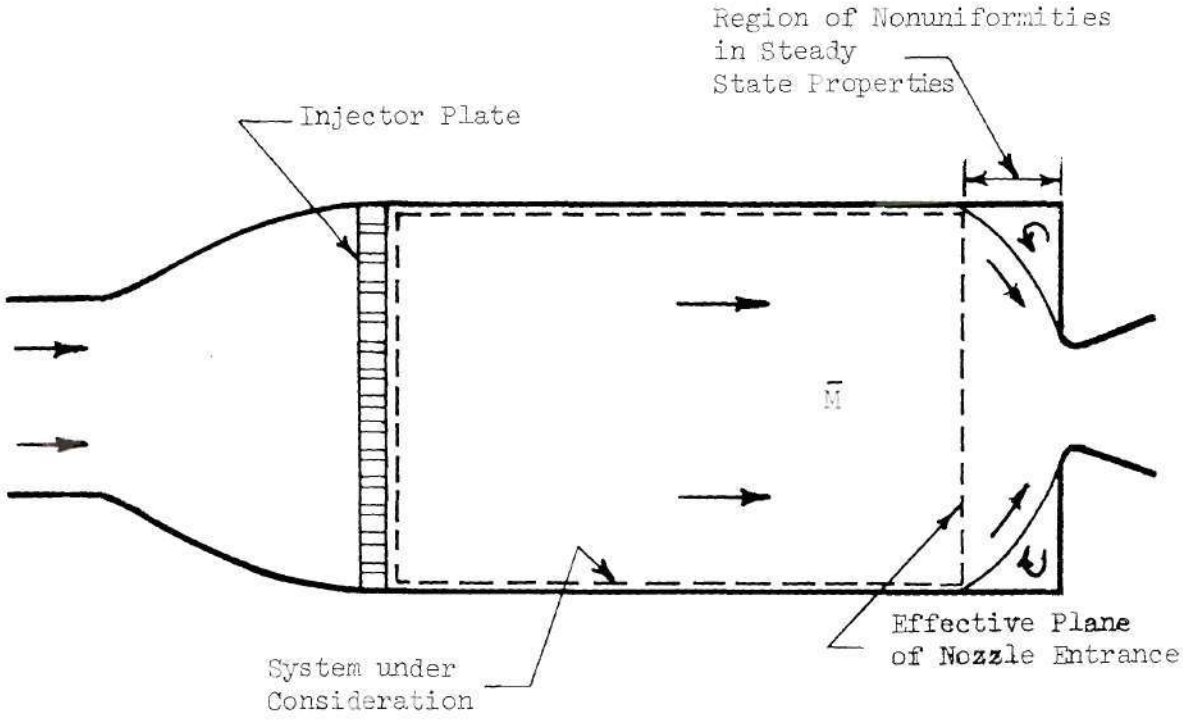

Figure 50. Schematic Diagram of a Combustor with a Short Nozzle.

wave propagation through the nozzle port. The remaining three terms are a measure of the wave energy losses due to the presence of a mean flow.

The space and time integrations, indicated in Equations (2-20) and (2-21), can be performed only if the mode structure and time dependence of the oscillations inside the combustor are known. The required expressions are obtained by solving the system of conservation equations that describe the behavior of a small amplitude disturbance superposed on a one-dimensional flow field inside the simulated rocket combustor. The resulting expressions (i.e., see Reference 15) describing the time and one-dimensional space dependence of the pressure and velocity perturbations inside the combustor are given by Equations (2-2) and (2-3). The real parts of the resulting complex expressions, which represent the physical oscillations in the chamber, are given by the following expressions:

$$\mathrm{Re}(p_1) = \gamma\bar{p}\hat{A}\Big[\sin(\omega t + az)\,\sinh(\pi\alpha)\cos(\pi\beta + \pi\,\frac{2d}{\lambda} + Rz) - \cos(\omega t + az)\cosh(\pi\alpha)\sin(\pi\beta + \pi\,\frac{2d}{\lambda} + Rz)\Big] \qquad \text{(B-2)}$$

$$\mathrm{Re}(u_1) = \bar{c}\hat{A}\Big[\sin(\omega t + az)\cosh(\pi\alpha)\cos(\pi\beta + \pi\,\frac{2d}{\lambda} + Rz) - \cos(\omega t + az)\sinh(\pi\alpha)\sin(\pi\beta + \pi\,\frac{2d}{\lambda} + Rz)\Big] \qquad \text{(B-3)}$$

Using Equations (B-2) and (B-3), letting $z = L_c$ and $d = 0$, and performing the time integrations indicated in Equation (B-1) give the following results:

$$< (p_1 u_1)_{z=L_c} > = \frac{1}{4}\,(\gamma\bar{p}\hat{A})(\bar{c}\hat{A})\sinh(2\pi\alpha) \qquad \text{(B-4)}$$

$$< (p_1^2)_{z=L_c} > = \frac{1}{2} (\gamma \bar{p} \hat{A})^2 \left[\cosh^2(\pi\alpha) \sin^2(\pi\beta + RL_c) + \sinh^2(\pi\alpha) \cos^2(\pi\beta + RL_c) \right] \quad \text{(B-5)}$$

$$< (u_1^2)_{z=L_c} > = \frac{1}{2} (\bar{c} \hat{A})^2 \left[\sinh^2(\pi\alpha) \sin^2(\pi\beta + RL_c) + \cosh^2(\pi\alpha) \cos^2(\pi\beta + RL_c) \right] \quad \text{(B-6)}$$

Substituting the expressions given in Equation (B-4) through (B-6) into Equation (B-1) yield the following result:

$$2\alpha_N \hat{V} = - \frac{1}{4} A_c (\gamma \bar{p} \bar{c}) \hat{A}^2 \left[2\bar{M} \cosh(2\pi\alpha) + (1 + \bar{M}^2) \sinh(2\pi\alpha) \right] \quad \text{(B-7)}$$

where for a one-dimensional oscillation Equation (2-21) gives

$$\hat{V} = A_c < \int_0^{L_c} \left\{ \frac{\bar{\rho}}{2} u_1^2 + \frac{1}{2\bar{\rho}\bar{c}^2} p_1^2 + \frac{\bar{u}}{\bar{c}^2} u_1 p_1 \right\} dz > \quad \text{(B-8)}$$

In writing Equation (B-8), it has been implicitly assumed here that the length of the region of non-uniformities is very small when compared to L_c. Substituting Equations (B-2) and (B-3) into Equation (B-8) and performing the indicated space and time integrations give

$$\hat{V} = \frac{1}{4} A_c \hat{A}^2 L_c \gamma \bar{p} \left[\cosh(2\pi\alpha) + \bar{M} \sinh(2\pi\alpha) \right] \quad \text{(B-9)}$$

Finally, substituting Equation (B-9) into Equation (B-7) and rearranging the terms result in the following expression for the decay or growth coefficient α_N:

$$\Lambda_N = \frac{\alpha_N L_c}{\bar{c}} = - \left[\frac{\bar{M} + \left\{ \frac{1 + \bar{M}^2}{2} \right\} \tanh(2\pi\alpha)}{1 + \bar{M} \tanh(2\pi\alpha)} \right] ; \sec^{-1} \quad \text{(B-10)}$$

Inspection of Equation (B-10) shows that the nozzle decay coefficient, in the case of a longitudinal oscillation, can be determined once $\bar{c}$, L_c, $\bar{M}$, and α are known. The quantities $\bar{c}$, L_c, and $\bar{M}$ are usually known a priori or they can be measured directly while the parameter α is measured as part of the determination of the nozzle admittance. With all of these parameters available, the nozzle decay coefficient may be determined from Equation (B-10). A plot, based on Equation (B-10), showing the dependence of the nondimensional nozzle decay coefficient Λ_N upon $\bar{M}$ and α is presented in Figure 51. This figure can be conveniently used to determine Λ_N once $\bar{M}$ and α are known from either experimental or theoretical data.

It is important to realize that the flow stream separates from the chamber walls, at some location upstream of the nozzle entrance, when the cross-sectional areas of the combustor and the nozzle entrance are not equal. When this occurs, the measured nozzle admittance provides information about the damping provided by both the nozzle and the non-uniform flow region just upstream of the nozzle entrance. Consequently, the calculated nozzle decay coefficient α_N accounts for both the damping provided by the nozzle and the non-uniform flow region located upstream of the nozzle entrance.

As was already pointed out during the discussion of the Study 3 admittance data, Equation (B-10) cannot be used directly to determine the nozzle decay coefficient of a submerged nozzle configuration. This is due to the fact that the gases leaving the nozzle cavity are flowing in a direction opposite to that of the primary chamber flow and the flow leaving the nozzle. The presence of a "reversed" cavity flow results in acoustic energy being "convected" from the cavity into the chamber. The

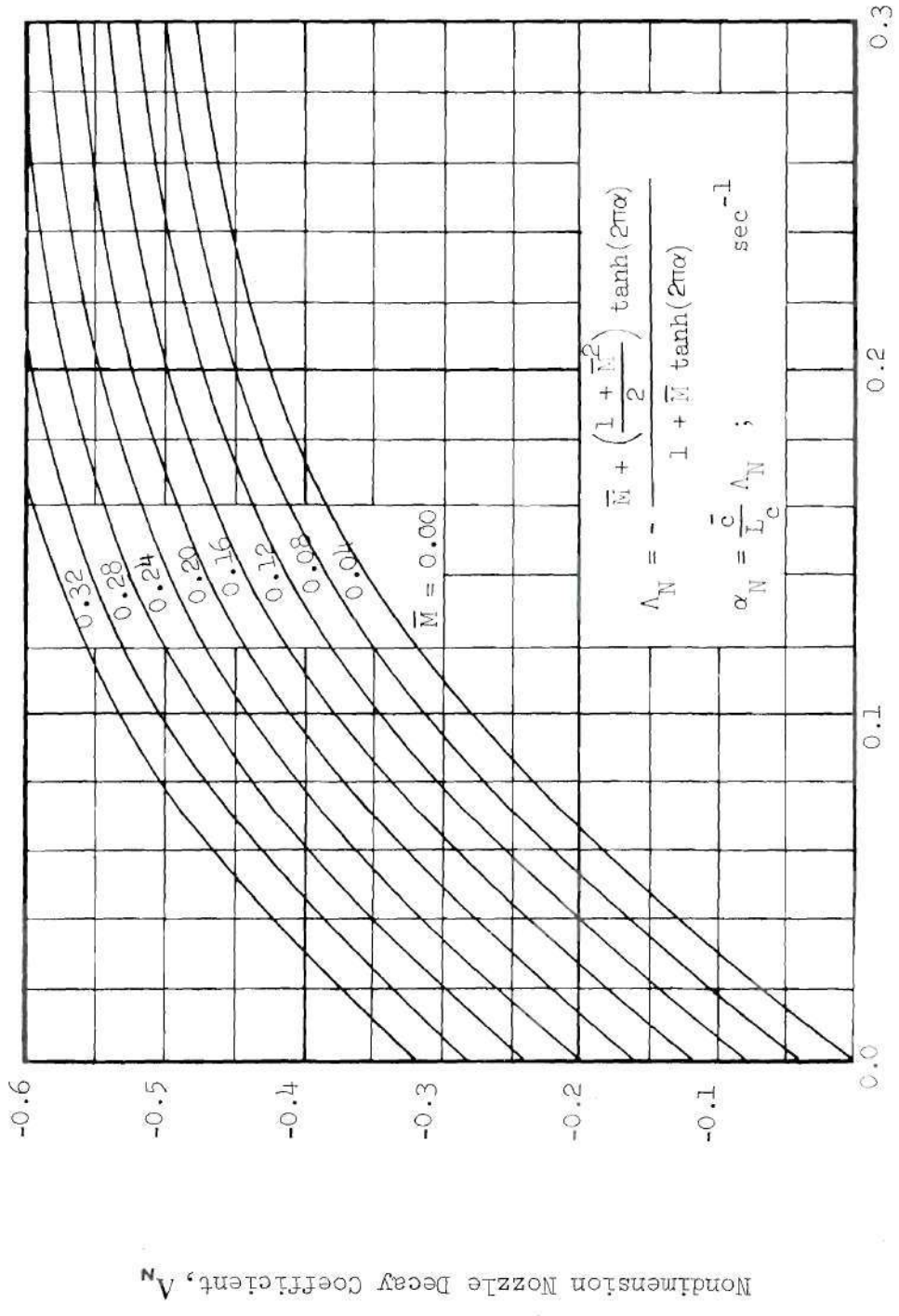

Figure 51. Dependence of Nozzle Decay Coefficient Λ_N upon α and $\bar{M}$.

Nozzle Admittance Parameter, α, Radians

presence of this secondary mean flow must be taken into consideration while performing the spatial integrations indicated in Equation (2-20). For computational purposes, the flow conditions in the combustor and the submerged nozzle entrance plane will be approximated by the velocity profiles shown in Figure 52. The nozzle effective mean flow Mach number, $\bar{M}_N$, accounts for both the primary combustor flow and the secondary cavity flow. Recognizing that the flow representation shown in Figure 52 is at best only approximate, and applying Equation (2-20) to the system shown in the figure results in the following expression:

$$2\alpha_N \hat{V} = -\Bigg\langle \Bigg[\int_{A_c} p_1 u_1 \, dS + \int_{A_c} p_1 u_1 \bar{M}_N^2 dS + \int_{A_s} p_1 u_1 \bar{M}_s^2 dS + \int_{A_c} \frac{\bar{M}_N}{\bar{\rho}\bar{c}} p_1^2 \, dS - \int_{A_s} \frac{\bar{M}_s}{\bar{\rho}\bar{c}} p_1^2 \, dS + \int_{A_c} \bar{\rho}\bar{c}\bar{M}_N u_1^2 dS - \int_{A_s} \bar{\rho}\bar{c} \bar{M}_s u_1^2 \, dS \Bigg] \Bigg\rangle \qquad \text{(B-11)}$$

where A_c is the chamber cross-sectional area and A_s is the cavity entrance area, both measured at the nozzle entrance plane. In deriving Equation (B-11) the relationships $\bar{\underrightarrow{M}}_N \cdot \underrightarrow{n} = \bar{M}_N$ where $\bar{M}_N$ is the effective nozzle entrance plane Mach number, $\bar{\underrightarrow{M}}_s \cdot \underrightarrow{n} = -\bar{M}_s$ where $\bar{M}_s$ is the Mach number of the secondary flow at the nozzle entrance plane, and $\underrightarrow{u}_1 \cdot \underrightarrow{n} = u_1$ have been used. Equation (B-11) can also be written as follows:

$$2\alpha_N \hat{V} = -\Bigg[(A_c + \bar{M}_N^2 A_c + \bar{M}_s^2 A_s) \langle p_1 u_1 \rangle + (\bar{M}_N A_c - \bar{M}_s A_s) \left\{ \frac{\langle p_1^2 \rangle}{\bar{\rho}\bar{c}} + \bar{\rho}\bar{c} \langle u_1^2 \rangle \right\} \Bigg] \qquad \text{(B-12)}$$

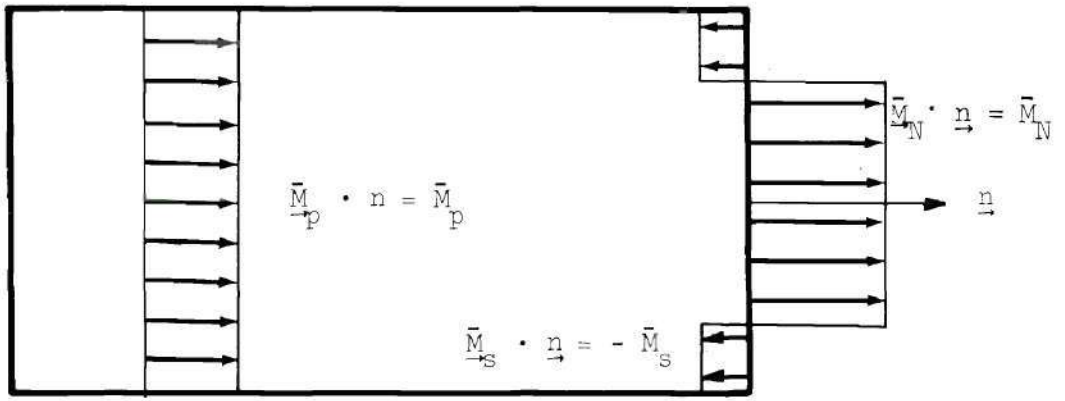

Figure 52. Schematic Diagram of a Combustor with a Submerged Nozzle.

To evaluate the volume integral $\hat{V}$, defined in Equation (2-21), the reverse flow in that part of the chamber near the cavity entrance is neglected and Equation (2-21) for a one dimensional oscillation reduces to the following form:

$$\hat{V} = A_c < \int_0^{L_c} \left(\frac{\bar{\rho}}{2} u_1^2 + \frac{1}{2\bar{\rho}\bar{c}^2} p_1^2 + \frac{\bar{M}_p}{\bar{c}} u_1 p_1 \right) dz > \qquad \text{(B-13)}$$

where $\bar{M}_p$ is the Mach number of the primary flow. Neglecting the wave motion in the cavity and using Equations (2-2) and (2-3) to describe the mode structure in the combustor, and using Equations (B-12) and (B-13) results in the derivation of the following expression for the nondimensional decay coefficient, Λ_N, for a combustor with a submerged nozzle:

$$\Lambda_N = - \frac{\left[\bar{M}_N - \bar{M}_s \frac{A_s}{A_c} \right] + \left[\frac{1 + \bar{M}_N^2 + \bar{M}_s^2 \frac{A_s}{A_c}}{2} \right] \tanh(2\pi\alpha)}{\left[1 + \bar{M}_p \tanh(2\pi\alpha) \right]} \qquad \text{(B-14)}$$

Examination of Equation (B-14) indicates that the presence of a secondary flow resulted in the addition of two more terms to Equation (B-10) for the nozzle decay coefficient Λ_N. The first of these terms $\bar{M}_s \frac{A_s}{A_c}$ results in a decrease in nozzle damping while the second term $-\frac{1}{2} \bar{M}_s^2 \left(\frac{A_s}{A_c} \right) \tanh(2\pi\alpha)$ results in an increase in nozzle damping. However, order of magnitude considerations indicate that the first term is larger than the second term and hence the presence of the "reversed" cavity flow is expected to reduce nozzle damping and thus decrease engine stability.

When $\bar{M}_p$, $\bar{M}_N$, $\bar{M}_s$, and α are all small quantities Equation (B-14) can be approximated by the following expression:

$$\Lambda_N = - \left[(\bar{M}_N + \pi\alpha) - \bar{M}_s \frac{A_s}{A_c} \right] \tag{B-15}$$

Comparing Equation (B-15) with the corresponding expression derived for the nonsubmerged nozzle (i.e., Equation (2-30)) also suggests that the submerged nozzle offers less damping due to the presence of a reversed secondary flow whose effect is represented by the term $\bar{M}_s A_s / A_c$.

REFERENCES

1. Price, E. W., "Experimental Solid Rocket Combustion Instability," Tenth Symposium (International) on Combustion, The Combustion Institute, 1965, pp. 1067-1082.

2. Bergman, G. H., and Jessen, E. C., "Evaluation of Conventional Rocket Motor Instabilities for Analysis of Oscillatory Combustion," AIAA/SAE 7th Propulsion Joint Specialist Conference, Salt Lake City, AIAA Paper 71-755, 1971.

3. Browning, S. C., Krashin, M., and Thacher, J. H., "Application of Combustion Instability Technology to Solid Propellant Rocket Motor," Journal of Spacecraft and Rockets, 16, 1972, p. 21.

4. Roberts, A. K., Brownlee, W. G., and Jackson, F., "Combustion Instability and the Design of Solid Propellant Rocket Motors," Canadian Aeronautics and Space Journal, 16, 1970, p. 21.

5. Crocco, L. and Sirignano, W. A., "Behavior of Supercritical Nozzles under Three-Dimensional Oscillatory Conditions," AGARDograph 117, Princeton University, Princeton, New Jersey, 1967.

6. Crocco, L. and Sirignano, W. A., "Effect of Transverse Velocity Components on the Nonlinear Behavior of Short Nozzles," AIAA Journal, 4, 1966, pp. 1428-30.

7. Zinn, B. T., "Longitudinal Mode Acoustic Losses in Short Nozzles," Journal of Sound and Vibration, 22, 1972, pp. 93-105.

8. Crocco, L., Monti, R., and Grey, J., "Verification of Nozzle Admittance Theory by Direct Measurement of the Admittance Parameter," ARS Journal, 31, 1961, pp. 771-775.

9. Buffum, R. G., Dehority, G. L., Slates, R., and Price, E. W., "Acoustic Attenuation Experiments on Subscale Cold Flow Rocket Motors," AIAA Journal, 5, 1967, pp. 272-280.

10. Slates, R. O., Buffum, F. G., and Dehority, G. L., "Acoustic Attenuation in Resonant Model-Rocket Motors," ICRPG/AIAA Second Solid Propulsion Conference, 1967, pp. 173-80.

11. Culick, F. E. C. and Dehority, G. L., "Analysis of Axial Acoustic Waves in a Cold Flow Rocket," Journal of Spacecraft and Rockets, 6, pp. 591-595.

12. Beranek, L. L., Acoustic Measurements, John Wiley and Sons, New York, 1949.

13. Lippert, W. K. R., "The Practical Representation of the Standing Waves in an Acoustic Impedance Tube," Acustica, 3, 1953, pp. 153-160.

14. Melling, T. H., "An Impedance Tube for Precision Measurement of Acoustic Impedance and Insertion Loss at High Sound Pressure Levels," Journal of Sound and Vibration, 28, 1973, pp. 23-54.

15. Bell, W. A., "Experimental Determination of Three-Dimensional Liquid Rocket Nozzle Admittances," Ph.D. Thesis, School of Aerospace Engineering, Georgia Institute of Technology, Atlanta, Georgia, 1972.

16. Zinn, B. T., Bell, W. A., Daniel, B. R., and Smith, A. J., "Experimental Determination of Three-Dimensional Liquid Rocket Nozzle Admittances," AIAA Journal, 11, 1973, pp. 267-272.

17. Morse, P. M. and Ingard, K. U., Theoretical Acoustics, McGraw Hill, New York, 1968.

18. Bell, W. A., Daniel, B. R., and Zinn, B. T., "Experimental and Theoretical Determination of the Admittances of a Family of Nozzles Subjected to Axial Instabilities," paper presented at 23rd International Astronautical Congress held in Vienna, Austria, 1972. (Also accepted for publication in Journal of Sound and Vibration.)

19. Coates, R. L. and Horton, M. D., "Design Considerations for Combustion Instability," Journal of Spacecrafts and Rockets, 6, 1969, pp. 296-302.

20. Hart, R. W., and McClure, F. T., "Theory of Acoustic Instability in Solid Propellant Rocket Combustions" Tenth Symposium (International) on Combustion, Combustion Institute, 1965, pp. 1047-1065.

21. Cantrell, R. H. and Hart, R. W., "Interaction Between Sound and Flow in Acoustic Cavities; Mass, Momentum and Energy Considerations," Journal of Acoustic Society of America, 36, 1964, pp. 697-706.

22. "Minuteman III Third Stage Pressure Oscillation Study," Aerojet Report 1387-01F, 1971.

23. Shapiro, A. H., The Dynamics and Thermodynamics of Compressible Fluid Flow, Ronald Press, New York, Vol. 1, 1953.

24. Smith, A. J., "Admittance Data Reduction Using A to D Converter; Users Manual," School of Aerospace Engineering, Georgia Institute of Technology, Atlanta, Georgia, 1973.

25. Marble, F. E., "Acoustic Disturbance from Gas Nonuniformities Convected Through a Nozzle," Paper presented at the Interagency Symposium on University Research in Transportation Noise, Stanford University, Vol. II, 1973, pp. 547-561.

26. "Gemini Stability Improvement Program," Aerojet Report GEMSIP FR-1, Vol. 3, 1965.

VITA

Bangalore Ananthamurthy Janardan was born in Bangalore, India on April 4, 1940. He graduated in 1958 with a Bachelor of Science degree from Mysore University. He had his technical education at Birla Institute of Technology, Ranchi and graduated in 1963 with a Bachelor of Science degree in Mechanical Engineering. He received in 1965 a Master of Engineering degree in Mechanical Engineering from the Indian Institute of Science, Bangalore. Since then he has been employed with the Propulsion Division of the National Aeronautical Laboratory, Bangalore. At present he is on leave of absence from the Laboratory and is attending the school of Aerospace Engineering of the Georgia Institute of Technology. He received the degree of Master of Science from Georgia Tech in 1972.